Theoretical study of thermoelectric properties in nanostructures

Brice Davier

NNT : 2018SACLS529

Thèse de doctorat

Theoretical study of thermoelectric properties in nanostructures

Thèse de doctorat de l'Université Paris-Saclay
préparée à Université Paris-Sud

Ecole doctorale n°575 Physique et ingénierie: électrons, photons, sciences du vivant (EOBE)
Spécialité de doctorat : Électronique et optoélectronique, nano- et microtechnologies

Thèse présentée et soutenue à Gif-sur-Yvette, le 29/11/2018, par

M. BRICE DAVIER

Composition du Jury :

M. David LACROIX Professeur, Université de Lorraine, CNRS, LEMTA	Président
M. Jérôme SAINT-MARTIN Maître de Conférence, Université Paris Sud (C2N)	Directeur de thèse
M. Sebastian VOLZ Directeur de Recherche, LIMMS/CNRS-IIS	Co-directeur de thèse
M. Samy MERABIA Chargé de Recherche, CNRS, ILM	Rapporteur
M. Mathieu LUISIER Associate Professor, ETH Zurich	Rapporteur
Mme Jelena SJAKSTE Chargé de Recherche, LSI, Palaiseau	Examinateur
M. Jay AMRIT Maître de Conférence, Paris Sud, Orsay - LIMSI-CNRS	Invité

Contents

List of Tables

List of Figures

Introduction

The thermoelectric conversion is a subject of active research. Its main applications are related to energy harvesting for autonomous power supply system as well as heat management in particular for CPU cooling. Yet, common thermoelectric systems unfortunately rely on rare and toxic compounds such as Bismuth Telluride, Lead Telluride, etc., . Their replacement by Silicon and Germanium which are more abundant and widely used by the microelectronic industry would be appealing. However, their intrinsic thermoelectric properties are poor especially close to room temperature.

In order to improve the thermoelectric conversion of devices based on Si and Ge, nanotechnologies provide new routes of optimization. Indeed, nanostructuring can be used to tune the intrinsic properties of nanostructures by several orders of magnitude.

In this framework, this PhD dissertation investigates the thermal properties of recently fabricated Si and Ge polytype nanowires. They are made of quasi-periodic sequences of cubic and hexagonal phases of Si or Ge. The presence of many polytype interfaces is expected to be beneficial to the thermoelectric properties. Since experimental characterizations of this nanowires are still very challenging, developing in parallel specific numerical tools is of high importance for developing this technology.

During this thesis, an original Monte Carlo simulator dedicated to phonon transport have been developed. It is a full-band and 3D simulator that is able to provide deep insights of thermal transport in complex nanodevices. As the required "semi-empirical" parameters are computed by using *ab initio* data, a large class of materials and phase can be modeled even the availability of experimental characterization. Besides, studies performed by using Molecular Dynamics are presented in order to parametrize semi-transparent interface modeling in the MC code.

In §1 the context of this thesis is presented. The theoretical models used through this work are presented in §2. The Monte Carlo and Molecular Dynamics simulations methods are detailed in §3. In §4, our methods are validated by studying the properties in bulk materials and thin films. §5 our implementation of rough boundaries in the Monte Carlo simulations is presented as well as the resulting simulations. Finally, in §6, the properties of interfaces between the different phases of Si and Ge are investigated.

1 Context

Currently, a significant part of the worldwide produced energy is rejected as wasted heat. In 2007, less than half of the produced energy was effectively consumed (cf. Smith, Belles, and Simon (2011)). There is thus a strong motivation to develop technologies that are able to harvest that large amount of lost energy.

Thermoelectricity deals with the coupling between the flux of electrical charges (current) and heat flux, enabling the direct conversion of thermal energy to electrical energy. The thermal energy can be transferred in solid-state systems by several mechanisms: lattice vibrations (related to pseudo particles called phonons), electrons (that is the electronic part of thermal conduction) and electromagnetic fields (i.e. by thermal radiation, cf. G. Chen (2005)). In this thesis, we focus on the thermal transport in semiconductors. Only the lattice vibrations are considered in this work, as other mechanisms (electronic conduction and radiation) are negligible in the studied systems. Besides, only the thermal part of the thermoelectric properties are studied.

At the macroscale, the thermal properties of materials can be well characterized by the thermal conductivity that is accurately modeled by using the Fourier's law (Fourier 1822). However, when the device size approaches the characteristic length scale of microscopic phenomena, the thermal properties are modified, and new theoretical models are required. Due to the high complexity of the nanoscale heat transport, numerical simulations have become very helpful in the study of nanomaterials and devices.

1.1 Thermoelectricity

The main application of thermoelectricity that we consider is the harvesting of thermal energy. While thermoelectric generators have a low efficiency with respect to other technologies (cf. Vining (2009)), they also have several advantages. Their mechanical simplicity makes them more reliable, and independent of gravity or atmospheric pressure. For instance, it makes them attractive to the spatial industry, and they have been used to power several probes and rovers. They also can be easily miniaturized and could be embedded in a wide range of products. By using such generators, temperature differences naturally present in the environment can be exploited to supply low power devices such as autonomous sensors.

Another application of thermoelectrics is the heat management. Current microprocessor technologies are limited by heat dissipation. Indeed, the increase of clock frequencies leads to an increase of the heat production in electrical devices and the limits of passive heat diffusion are reached. Thermoelectric devices could be integrated close to the sources of heat in order to extract it more efficiently (Pop 2010; Moore and Shi 2014).

The efficiency of a thermoelectric material is characterized by its thermoelectric figure of merit ZT, which is proportional to the Seebeck coeficient S, the electrical conductivity σ and inversely proportional to the thermal conductivity κ.

$$ZT = \frac{S^2 \sigma T}{\kappa} \tag{1}$$

In order to improve the conversion efficiency, ZT has to be increased. Consequently, κ should be reduced while S and σ should be increased. However, κ and σ are not independent parameters in common materials, and ZT optimization have remained very limited for decades (cf. Chen et al. (2003)).

Figure 1 (reproduced from Heremans et al. (2013)) shows the evolution of the figure of merit ZT of several materials between 1940 and 2010. Constant progress was made until 1970 when ZT of bulk materials reached a plateau. The ZT of Bismuth Telluride was then measured around 1. Unfortunately, the best thermoelectric materials happened to be rare and pollutant. This makes difficult their widespread use.

A thermoelectric device based on Si and Ge would be a better candidate, as they are abundant and compatible with the current fabrication technologies. However bulk Si and Ge ZT are too low to allow interesting thermoelectric applications.

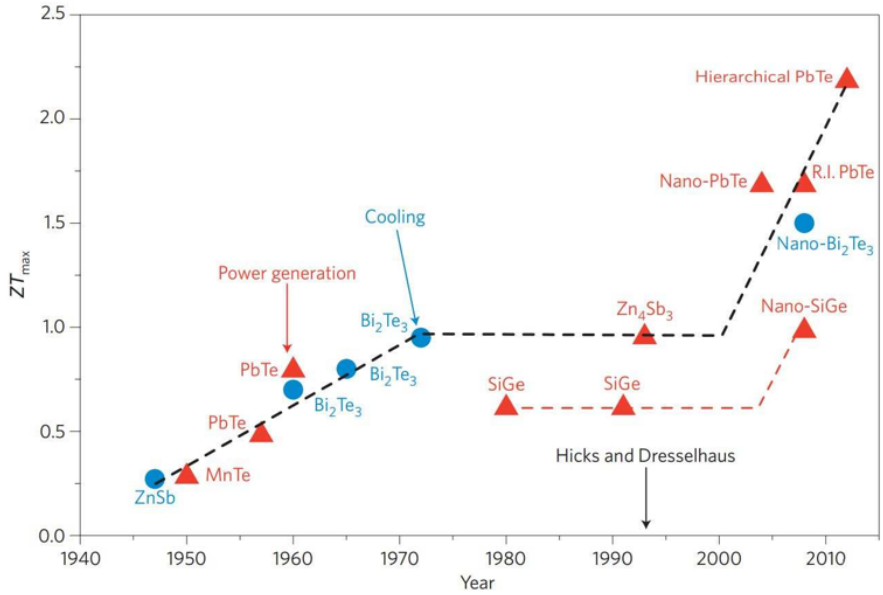

Figure 1: Evolution of the maximum ZT over time. Reproduced from (Heremans et al. 2013).

The pioneering work of Hicks and Dresselhaus (1993) opened new research directions by demonstrating that nanostructures could be used to significantly enhance the thermoelectric efficiency. Following this research trend, this work focuses on the reduction of the thermal conductivity, which is required for improving thermoelectric energy conversion (G. Chen 2005) by using nanostructuring.

Indeed, the characteristic length of electron transport, called the electron mean free path l^e_{mfp}, is usually much smaller than those involves in thermal transport

referred as $l^p_{mfp}h$. Moreover, boundary scattering mechanisms become significant in nanostructures (Ziman 2001; Peierls 1929) in which a reduction of the two previous characteristic lengths can be achieved. Thus, designing a nanostructure with an intermediate length L ($l^e_{mfp} < L < l^p_{mfp}h$)) would have a greater impact on the phonon transport than on the thermal one. Finally, ratios of $\frac{\sigma}{\kappa}$ and thus ZT higher than its bulk counterpart can be achieved. Experimental measurements in Silicon nanowires of appropriate diameters (Qiu et al. 2015) i.e. on the order of 100 nm, have already demonstrated a large reduction of the effective thermal conductivity (Li et al. 2003; Boukai et al. 2008; Hochbaum et al. 2008), down to 2 orders of magnitude lower than the bulk conductivity. As the related electrical conductivity reduction is weak, ZT values higher than 1 have been demonstrated (cf. Akiyama et al. (2017)).

Several other nanostructures have been investigated, e.g. nanofilms, superlattices (Hu and Poulikakos 2012; Mu et al. 2015), core-shell structures (Hu et al. 2011), phononic crystals (Yu et al. 2010), nanowire networks (Verdier, Lacroix, and Termentzidis 2018). The thermal conductivity can also be reduced by alloying (Garg et al. 2011) or partial amorphization (Donadio and Galli 2009) of materials.

Recently, Vincent et al. (2014) developed an original method for fabricating nanowires composed of a quasi-periodic stacking of cubic and hexagonal phases of Si or Ge. Images of a Ge polytype nanowire are shown in Figure 2 (reproduced from (Vincent et al. 2014)), showcasing the two phases and their interface. In addition to the ZT improvement due to the size effect (as in other nanowires), multiple polytype interfaces could affect strongly the thermal conductivity. Meanwhile, the electrical conductivity should be less impacted by the change of phase.

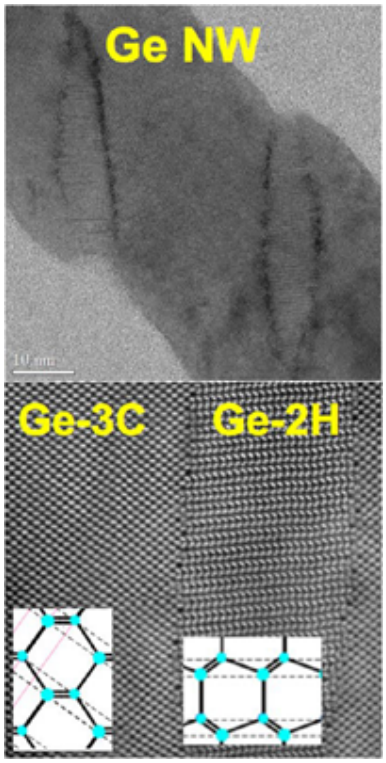

Figure 2: Germanium polytype nanowire (Vincent et al. 2014).

1.2 Nanoscale thermal transport

At low dimensions, the distribution of particles can strongly differ from the thermal equilibrium. The classical Fourier's law of conduction then becomes unable to describe the thermal transport, and nanoscale models are required. These models must include the material properties and the effects of nanostructures. They usually consider the heat either from the trajectories of individual atoms, or as collective excitations (i.e. phonons).

DFT (Density Functional Theory) simulations have been used to calculate the thermal properties of bulk materials (Seko et al. 2015) Or small nanostructures (Markussen, Jauho, and Brandbyge 2008; Li et al. 2012). This *ab initio* method can be used to study materials or structures that are not previously characterized. However, full quantum simulations such as DFT require a lot of computing resources, and are thus limited to very small systems in the order of hundreds of atoms.

The Atomistic Green's Function (AGF) method can solve the transmission function in a device, but it is generally limited to ballistic transport (N. Mingo and Yang 2003) but can be extended to include all relevant scattering mechanisms (Luisier and Klimeck 2009).

Among atomistic simulations, classical Molecular Dynamics (MD) simulation is a very common method to simulate the heat transfer. In this approach, the

trajectories of atoms are numerically solved and analyzed. The materials are described by using empirical inter-atomic potentials. This classical approach of transport is accurate only at high temperature, higher than the Debye's temperature, that is 640 K in Si (Madelung, Rössler, and Schulz 2002).

MD simulations have been widely applied for modeling nanowires made of different crystalline structures (Termentzidis et al. 2013) and of diameter up to 20 nm (Volz and Chen 1999; Donadio and Galli 2009). The effect of rough interfaces can be modeled directly in real space (Liu and Chen 2010; Qiu, Sun, and Ruan 2011) as well as the resulting reflections of mechanical waves. MD simulations can be performed at equilibrium (EMD) or non-equilibrium (NEMD) conditions. Previous authors have compared them in bulk Si (He et al. 2012; Sellan et al. 2010; Schelling, Phillpot, and Keblinski 2002) and Ge (He et al. 2012). The conductance of Si/Ge interfaces has also been investigated (Merabia and Termentzidis 2012) as well as the conductivity of Si/Ge superlattices (Termentzidis and Merabia 2012). Due their computational consumptions, MD studies are generally limited to devices that are made of ten thousands of atoms.

Methods based on the resolution of the Boltzmann Transport Equation (BTE) for phonons are relevant for larger system and can cover the full temperature range. The linearized BTE can be solved analytically when simple phonon dispersions and scattering terms are considered as done in pioneering works of Callaway (Callaway 1959) and Holland (Holland 1963). When considering simple geometries, it can be solved for instance by a direct approach (Nghiêm, Saint-Martin, and Dollfus 2016), a discrete ordinate method (Yang and Chen 2004) or a finite volume method (Narumanchi, Murthy, and Amon 2005).

But for 3D problems, a stochastic particle Monte Carlo method (Jacoboni and Lugli 2012) is much more numerically efficient and complex scattering terms can be implemented (Hamzeh and Aniel 2011). This versatile approach can solve accurately the BTE much beyond the linear approximation and in complex geometries. It has been used to study bulk materials (Mazumder and Majumdar 2001; Péraud and Hadjiconstantinou 2011; Klitsner et al. 1988; Peterson 1994), as well as nanocrystalline materials (Yang and Minnich 2017), porous nanofilms (Wolf, Neophytou, and Kosina 2014; Maire et al. 2017; Hao, Chen, and Jeng 2009) nanowires (Y. Chen et al. 2005; Lacroix, Joulain, and Lemonnier 2005), nanoribbons (Mei et al. 2014), etc. An important improvement of the MC simulations is the introduction of variance reduction methods in (Péraud and Hadjiconstantinou 2011).

In many MC approaches, simple isotropic phonon dispersions (Mazumder and Majumdar 2001; Lacroix, Joulain, and Lemonnier 2005) are assumed. Few works have used a full-band dispersion, i.e. have considered the phonon modes in the entire 3D Brillouin Zone (Kukita, Adisusilo, and Kamakura 2014; Aksamija and Knezevic 2010). However, significant deviations from isotropic calculations can be obtained (Kukita, Adisusilo, and Kamakura 2014). The accuracy of semi-empirical methods such as BTE or MD is directly related to the choice of their input parameters (inter-atomic potential, dispersion properties, phonon lifetimes, etc.). They are thus not convenient to study a new material for which such parameters are unknown. A methodology for solving the BTE in thin films without any adjustable parameter has been recently presented in (Chaput et al. 2018; Yang and Minnich 2017). In this simulation method, the BTE

parameters, i.e. full-band dispersion and full-band phonon-phonon scatterings rates, are preliminarily computed by using DFT calculation.

In MC simulation, the reflection at external rough boundaries is usually implemented by considering a specular reflection. Thus, external boundaries are designed in real space by using a realistic profile, e.g. using a saw-tooth shape (Moore et al. 2008) or a random surface (Ramayya et al. 2012). Other models consider a specific scattering term related to a diffusive reflection at the interface that randomizes the propagation direction of diffused phonons. Casimir has linked the thermal conductivity to the width of structures (Casimir 1938). More recently, a probability of specular reflection (Berman, Simon, and Ziman 1953; Ziman 2001) using a diffusive characteristic length for ultra-thin wires (Santamore and Cross 2001) have been defined. In Soffer's work (Soffer 1967), this probability depends on the incident wave vector of phonons plus two empirical parameters: the surface roughness standard deviation and its tangential correlation. This model provides results close to experimental measurements (Maurer et al. 2015). The interface transmission is described by two common models: the Acoustic Mismatch Model (AMM) and Diffusive Mismatch Model (DMM) (Little 1959). AMM considers perfect interfaces that conserve the wave coherence, while the DMM (Swartz and Pohl 1989) supposes that the interfaces are completely diffusive. More advanced methods based on MD (Merabia and Termentzidis 2012), AGF (Tian, Esfarjani, and Chen 2012) and *ab initio* lattice dynamics calculations (Alkurdi, Pailhès, and Merabia 2017) have also been used.

2 Theoretical models

In this chapter, we detail the theoretical basis of our studies. The concepts of thermal conductivity and interface thermal conductance are presented.

The two first sections of this chapter presents the studied devices and the different kinds of material modeling used in this work. The next sections focus on the heat transfer modeling and present relevant semi-analytical approaches. Numerical methods to solve the heat transfer are presented in details in the next chapter.

2.1 Simulated devices

In this thesis, different types of nanostructures, schematized in Figure 3, are investigated: nanofilms, nanowires and heterojunctions. In nanofilms, the external interfaces, separated by a finite distance, are called the top and bottom interfaces. In nanofilms both the in-plane and cross-plane configurations are considered, depending on whether the thermal flux is parallel or perpendicular to the interfaces, respectively.

As schematized in Figure 3, to implement numerically the devices, a cubic mesh is used. A material (of arbitrary crystal orientation) is assigned to each cell. All devices are in between a cold thermostat (blue plane) and a hot one (red plane). A face of a cell can be either transparent (when the adjacent cell is made of the same material), specular (no adjacent cell) or diffusive (green planes).

The reflected angle of a particle colliding with a specular face is equal to the incident one. This reflected angle is of course different when a diffusive face is involved and must be selected carefully, as explained later in this chapter. To mimic infinite dimensions, as needed for instance in cross-plane configuration for all directions except the transport one, specular reflections are implemented at opposite boundaries.

In this study, the heat transport is along the X-axis. The four devices shown in Figure 3 have different types of boundaries. They are:

(a) cross-plane nanofilm (CPNF), i.e. oriented along the cross-plane direction, with only specular boundaries;

(b) in-plane nanofilm (IPNF), i.e. oriented along the in-plane direction with a pair of specular (XZ planes) and diffusive (XY planes) boundaries (colored in green in Figure 3);

(c) rough nanowire (NW), with only diffusive boundaries.

(d) heterojunctions (HJ), with only specular boundaries, but composed of two materials separated in the center by an interface (colored in purple in Figure 3).

These devices are parametrized by their length L (distance between thermostats along X axis) and their width W (along the Z axis). In this study, only nanowires with a square cross section are considered (i.e. with the height along Y direction also equal to W).

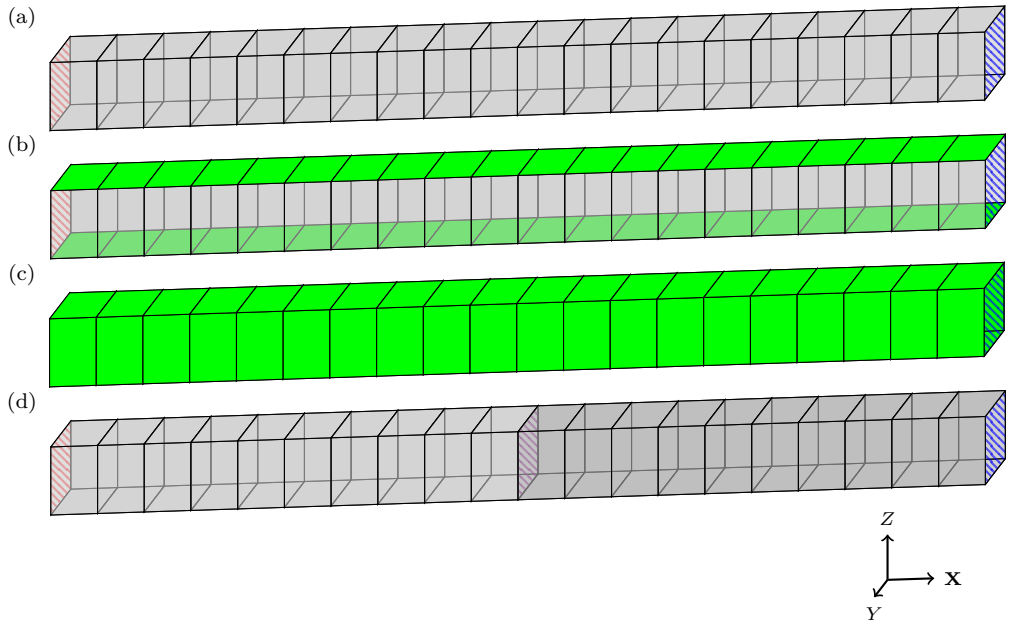

Figure 3: Schema of the simulated devices: (a) cross-plane nanofilm, (b) in-plane nanofilm, (c) nanowire and (d) heterojunction. Cold (hashed blue) and hot (hashed red) thermostats. Rough boundaries (green). Solid-solid interface (hashed purple).

2.2 Models of materials

To solve the heat transport equation in a solid-state system, the prior knowledge of both the dispersion relation and the scattering rates is required.

The dispersion relation is the relation between the phonon energy and wave vectors, defined in the entire reciprocal space. In a periodic lattice, the reciprocal space is periodic and the dispersion relation can be completely defined in a primitive cell centered on the origin called the Brillouin zone (BZ).

The movement of phonons in a material is perturbed by several scattering mechanisms, which can be characterized by their scattering rates. Usually, the main source of thermal resistance is due to the phonon-phonon scatterings.

It is possible to have an analytical representation of the dispersion relation and the scattering rates by using several approximations. In this thesis, a full band description of the BZ is mainly used, i.e. both the dispersion relations and scattering rates are numerically calculated for a large number of wave vectors in the whole BZ.

2.2.1 Full band models

In order to study the details of thermal transport more accurately than the previous works, all phonon modes are considered, and the anisotropic effects are

included in the present work. Thus the energy dispersion, the phonon velocity as well as the phonon scattering rates in all directions are considered.

Indeed, all phonon states belonging to the Brillouin Zone (BZ) are considered in our "full-band" description. To determine all these full-band material parameters, we use two different methods: the Adiabatic Bond Charge Model (ABCM) and the Density Functional Theory (DFT).

ABCM is a semi-empirical model derived from the Force Constant Model (FCM). In FCM, the force matrices are defined between every neighboring atoms in the primitive unit cell of the lattice, ignoring all other interactions. The energy can thus be calculated for any wave vector from the equation of motion of the phonons. The ABCM improves its accuracy by accounting for the delocalization of the electron cloud. The resulting negative charge called 'bond charge' accumulates at the center of the interatomic bond. Using the parameters of Weber (1977) for Si and Ge, the resulting ABCM dispersions fit experimental measurements with an error of only 2%. The dispersion relations are calculated in this work for both the cubic and hexagonal phases of Si and Ge, as detailed in (Larroque 2016).

DFT is an *ab initio* method which is relevant to investigate the phonon properties of a large range of materials. It is accurate and does not require any empirical parameter, but consumes heavy computing power. The dispersion relation and scattering rates for the cubic and hexagonal phases of Si (called Si3C and Si2H, respectively) that are used in this thesis have been computed by Chaput et al. (2018), as explained in Togo, Chaput, and Tanaka (2015).

Since the scattering rates cannot be calculated via the ABCM which considers by principle only the harmonic part of the potentials, the thermal conductivity can only be calculated by using DFT. However, the ABCM dispersion is sometimes used to calculate the interface thermal conductance since we do not have yet a complete set of DFT data for all Ge phases. For both methods, the first BZ is discretized in a set of N wave vectors, with $N = 31 \times 31 \times 31 = 29791$ and $N = 31 \times 31 \times 19 = 18259$ for cubic and hexagonal phases, respectively. Cubic and hexagonal phases have 6 and 12 phonon modes, respectively. The angular frequency, the group velocity and the phonon-phonon scattering rates are calculated for each discrete state characterized by a couple of a wave vector $\vec{q}$ and a mode m.

The only phonon scattering rates computed here by DFT are those related to the intrinsic phonon-phonon scattering mechanisms that are dominant in bulk materials. These phonon-phonon scattering rates λ are calculated via the finite displacement method detailed in supplementary materials of (Chaput et al. 2018; Togo, Chaput, and Tanaka 2015), for 101 temperatures ranging between 0 and 1000 K. In brief, DFT calculations have been performed by using the finite displacement method with PAW pseudopotentials, within the PBE approximation. This approach allows obtaining the forces on atoms, from which the harmonic and anharmonic force constants can be extracted. The phonon frequency and group velocity can then be computed from the dynamic matrix. During the simulation, the values corresponding to intermediate temperatures are interpolated by using a cubic spline method. We should note that Normal and Umklapp scattering mechanisms are not distinguished in our approach. Thus, our phonon-phonon scattering rates represent actually an average effect

due to a combination of the two kind of mechanisms.

Due to the discrete nature of our BZ description, the definition of the iso-energy states that are used for instance to select the final state after any scattering event leads to a fluctuation of energy inside the discrete states due to their finite size. Thus, the strict conservation of angular frequency (or energy) is modulo the frequency discretization step $\Delta\omega$. In our simulation $\Delta\omega$ is defined as $\Delta\omega = \omega_{max}/128$ where ω_{max} is the maximum phonon frequency in the material (this value of $\Delta\omega$ leads to negligible average energy loss as shown in §3.1.11).

The resulting iso-energy curves of the first phonon mode from DFT data are plotted in Figure 4. Parts (a) and (b) represent the BZ in face centered cubic and hexagonal lattices (for Si3C and Si2H, respectively) and their high symmetry points (from Setyawan and Curtarolo (2010)). Parts (c), (d), (e), and (f) are cartographies of the angular frequency in the main cutting planes of the BZ. In the cutting plane ΓXL of cubic silicon in (c), iso-energy curves are far from being circular (spherical in 3D) as in isotropic materials in the whole frequency range. In particular, the anisotropy between the L and U points is strong. In the hexagonal phase in (d), (e), and (f), an isotropic behavior is nearly achieved in all planes ($K\Gamma M$, $M\Gamma A$, and $K\Gamma A$, respectively) but only at low frequencies. In contrast, far from the G point the anisotropy becomes strong, in particular between the M and K points.

We can also see that the phonon group velocities, which are the derivatives of the angular frequency with respect to the wave vectors, will not be isotropic. Furthermore, in the optical modes, some regions of the BZ even show a group velocity with a direction opposite to the corresponding wave vectors.

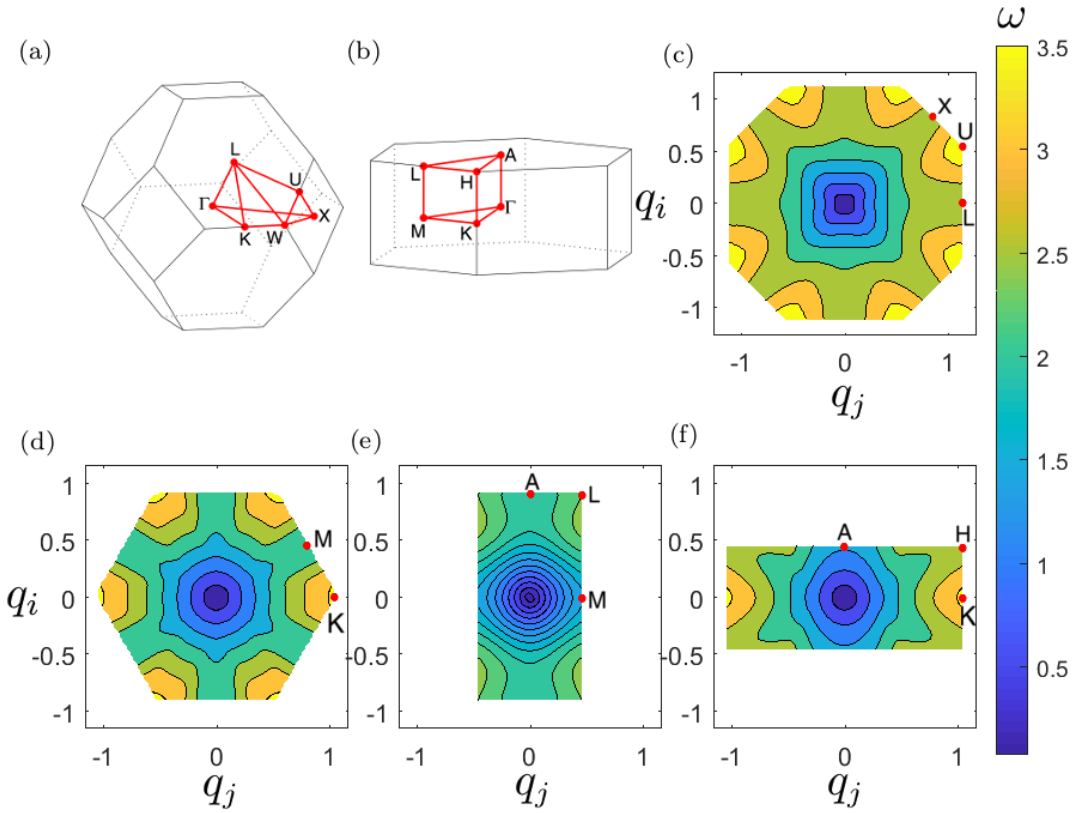

Figure 4: Cartography of the angular frequency ω in the BZ. Wave vectors $q_{i,j}$ are in $[10^{13}\ 2\pi/\mathrm{m}]$. Schema of the BZ in (a) Si3C, (b) Si2H. Iso-energies in (c) the (100) plane of Si3C, (d),(e),(f) in the (10-10), (11-20) and (0001) planes of Si2H, for the first phonon mode.

Similarly to the previous figure, the scattering rates in the main planes of Si3C and Si2H are represented in Figure 5. It shows an even stronger anisotropy in the dispersion relations. These figures illustrate the necessity of using a full-band representation of the BZ instead of a simple isotropic analytical formula.

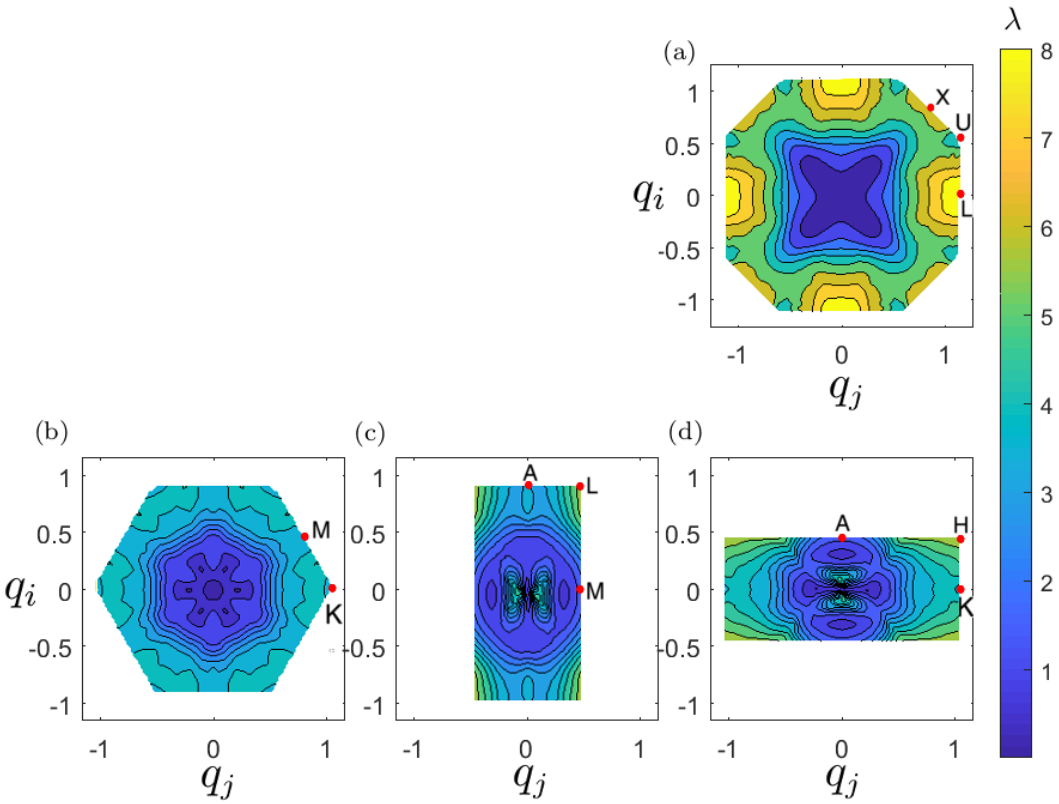

Figure 5: Cartography of phonon-phonon scattering rates λ in the BZ. Wave vectors $q_{i,j}$ are in [10^{10} Hz]. Iso-energies in (a) the (100) plane of Si3C, (b),(c),(d) in the (10-10), (11-20) and (0001) planes of Si2H, for the first phonon mode.

2.3 Models of rough boundaries

In nanostructures, the contribution of rough boundaries on the thermal resistance needs to be considered. Indeed, this contribution can become stronger than those of phonon-phonon scattering mechanisms.

A first model of the rough boundary contribution in thermal resistance was introduced by Casimir (1938). He considered all rough boundaries as black bodies at a constant temperature gradient. This means that all points in a structure emit as much energy as they absorb, i.e. they are perfectly diffusive boundaries. An average scattering rate within this model can be defined such as:

$$\lambda_{\text{boundary}} = \frac{v}{WF} \tag{2}$$

where F is a form factor related to the shape of the device independent from the device width W, and v is the phonon group velocity.

This model was improved by the work presented in (Berman, Simon, and Ziman

1953), by adding a probability p_{specular} to have a specular reflection at the rough boundary (thus $1-p_{\text{specular}}$ is the probability to have a diffusive reflection). This probability is constant and the rough boundary scattering rates have the form:

$$\lambda_{\text{boundary}} = \frac{v}{W}\frac{1+p_{\text{specular}}}{1-p_{\text{specular}}} \tag{3}$$

Soffer further improved the probability of specular reflection in (Soffer 1967), making it dependent on the incident angle of the phonon, the rms of the surface height deviation (called the surface roughness parameter Δ), and the spatial correlation of these deviations.

In the case where the spatial correlation of the surface roughness is negligible, the probability of specular reflection at a rough boundary becomes:

$$p_{\text{specular}} = e^{-(2cos(\theta)\Delta|\vec{q}|)^2} \tag{4}$$

where $\vec{q}$ is the incident wave-vector, θ its angle from the normal vector of the surface, and Δ is the surface roughness parameter.

Kazan et al. (2010) were able to fit experimental measurements of the thermal conductivity of nanowires from Hochbaum et al. (2008) with this model.

Since this model considered isotropic materials, we needed to adapt them to our full-band dispersion relation (see §2.2.1) in which the velocity and wave-vector of a given phonon state are not necessarily collinear. For a particle in a state j, the incident angle θ is changed to:

$$cos(\theta_j) = \frac{v_\perp}{|\vec{v}_j|} \tag{5}$$

where $v_{\perp,j}$ is the component perpendicular to the boundary interface of the velocity $\vec{v}_j$ of the incident phonon.

$q_\parallel$ being the component of the wave vector tangent to the surface, Chen et al. (2008) set p_{specular} to 1 when $Wq_\parallel > 1$ or to 0 otherwise. Also, Ramayya et al. (2012) models rough boundaries in real space using only specular reflections.

2.4 Heat transfer modeling and thermal conductivity

The thermal conductivity of a device is its main thermal property. In a nanostructure heated by two thermostats, it can be defined as:

$$\kappa = \frac{Q}{\Delta T}L \tag{6}$$

where Q is the net heat flux density (flux per unit of area) from the hot thermostat to the cold thermostat, ΔT is the temperature difference between the thermostats and L the distance between them.

2.4.1 Isotropic analytical models

In order to calculate bulk thermal conductivity, Callaway (1959) first used an isotopic and linear phonon dispersion relation, with only one artificial mode averaging all actual mode properties. The relaxation times were energy and temperature dependent, fitted from experimental measurements. This simple model managed to fit correctly the experimental thermal conductivities of Si and Ge at low temperatures.

Holland (1963) improved this model by separating the transverse and longitudinal acoustic modes. A frequency threshold was also used to better model the properties of higher energy phonons. The resulting bulk Si and Ge conductivities are relevant in the whole temperature range.

For phonon transport, many works assumed such simple dispersion relations (Mazumder and Majumdar 2001; Klitsner et al. 1988; Peterson 1994; Y. Chen et al. 2005; Lacroix et al. 2006). However, they require several parameters to fit on experimental measurements, and thus do not have predictive capabilities to investigate materials that have not been previously investigated experimentally. Besides, these approximations cannot reproduce accurately both the heat capacity and the heat conductivity (cf. the work of Larroque, Dollfus, and Saint-Martin (2017)) using a single normalization parameter in the whole temperature range.

2.4.2 Full-band semi-analytical models

Using the analytical dispersions relation and scattering rates mentionned in §2.2.1, the thermal conductivity can also be calculated with analytical formula. It is usually derived from the linearized BTE (see §3.1.1).

In this thesis, semi-analytical models (SA) as well as numerical approaches (MC and MD methods presented in the next chapter) are used to estimate the thermal conductivity. Previous full band models have been developed for instance by Mingo et al. (2003), and Aksamija and Knezevic (2010) demonstrated predictive calculations of the thermal conductivity with a full band dispersion relation. One originality of this work is to directly includes both dispersion relation and phonon-phonon scattering rates computed by using DFT calculations.

2.4.2.1 SA ballistic model

The ballistic SA model estimates the thermal conductivity in infinitely short cross-plane nanofilms (CPNF). The resulting thermal conductivity is linearly dependent on the distance L between thermostats. The heat flux densities involved are emitted from the hot $Q_{T_{\text{hot}}}$ and cold thermostats $Q_{T_{\text{cold}}}$ (at temperatures T_{hot} and T_{cold} respectively). The fluxes are estimated within a ballistic Landauer's formalism, without any diffusive mechanism leading to a heat transmission equal to 1.

The heat flux density injected by a thermostat at the temperature T, normal to

the vector $\vec{n}$ is then:

$$Q_T = V_s \sum_{\substack{\text{state } j \\ |\vec{v}_j \cdot \vec{n}|>0}} \hbar\omega_j |\vec{v}_j \cdot \vec{n}| f_{\text{BE}}(\omega_j, T) \tag{7}$$

where ω_j and $\vec{v}_j$ are the angular frequency and velocity of the phonons in the state j, V_s is the reciprocal volume of one state in the Brillouin zone, and f_{BE} is the equilibrium distribution.

The net heat flux density is:

$$Q^{\text{ballistic}} = Q_{T_{\text{hot}}} - Q_{T_{\text{cold}}} \tag{8}$$

The resulting thermal conductivity that it is L-dependent has the following form:

$$\kappa^{\text{ballistic}} = \frac{L\ V_s}{\Delta T} \left(\sum_{\substack{\text{state } j \\ \vec{v}_j \cdot \vec{n}>0}} \hbar\omega_j\ \vec{v}_j \cdot \vec{n}\ f_{\text{BE}}(\omega_j, T_{\text{hot}}) + \sum_{\substack{\text{state } j \\ \vec{v}_j \cdot \vec{n}<0}} \hbar\omega_j\ \vec{v}_j \cdot \vec{n}\ f_{\text{BE}}(\omega_j, T_{\text{cold}}) \right) \tag{9}$$

Usual approximations use the local temperature derivative of the phonon distribution instead of the temperature bias ΔT at the thermostats, leading to:

$$\kappa^{\text{ballistic}} = L\ V_s \sum_{\text{state } j} \hbar\omega_j |\vec{v}_j \cdot \vec{n}| \frac{\partial f_{\text{BE}}}{\partial T}(\omega_j, T_{eq}) \tag{10}$$

We found that these two approaches are not equivalent at low L. Similar expressions of the ballistic conductivity have been previously discussed for instance in Mingo et al. (2003) .

2.4.2.2 SA diffusive model

The SA diffusive model leads to a length-independent conductivity (as in an infinitely long CPNF) and should provide the bulk thermal conductivity. In this model, the conductivity is written as:

$$k^{\text{diffusive}} = V_s \sum_{\text{state}j} \hbar\omega_j |\vec{v}_j \cdot \vec{n}|^2 \frac{1}{\lambda_j} \frac{\partial f_{\text{BE}}}{\partial T}(\omega_j, T_{eq}) \tag{11}$$

where λ_j is the phonon-phonon scattering rate for state j.

The diffusive model is a solution of the linearized Boltzmann Transport equation (BTE). The steady-state BTE for each state j has the form:

$$\vec{v}_j \cdot \vec{\nabla} f_j = \left. \frac{\partial f_j}{\partial t} \right|_{\text{scatt}} \tag{12}$$

where f_j is the distribution of phonons in the state j.

The wave vector-dependent relaxation time approximation $1/\lambda_j$ is used to simplify the expression the phonon-phonon scattering rate, as follows:

$$\left.\frac{\partial f_j}{\partial t}\right|_{scatt} = -(f_j - f_{\mathrm{BE}}(\omega_j, T))\lambda_j(T) \tag{13}$$

By using this approximation, the system tends "naturally" to recover its equilibrium distribution.

We define f_j as the sum of the Bose-Einstein equilibrium distribution plus a small deviation δf_j.

$$f_j = f_{\mathrm{BE}}(\omega_j, T) + \delta f_j \tag{14}$$

The deviation from the equilibrium distribution is assumed to be much smaller than the equilibirum distrubtion **and** also independent from the temperature at the first order:

$$\delta f_j \ll f_{\mathrm{BE}}(\omega_j, T) \tag{15}$$

$$\frac{\partial(\delta f_j)}{\partial T} = 0 \tag{16}$$

Besides, as the spatial grandient can be expressed as follows:

$$\vec{\nabla} f_j = \frac{\partial f_j}{\partial T}\vec{\nabla} T \tag{17}$$

The left hand side of Eq. 12 can be written as:

$$\vec{v}_j \cdot \vec{\nabla} f_j = \vec{v}_j \cdot \vec{\nabla} T \frac{\partial f_j}{\partial T} = \vec{v}_j \cdot \vec{\nabla} T \frac{\partial f_{\mathrm{BE}}}{\partial T}(\omega_j, T) \tag{18}$$

Eq.12 becomes:

$$\delta f_j = \vec{v}_j \cdot \vec{\nabla} T \frac{\partial f_{\mathrm{BE}}}{\partial T}(\omega_j, T)\frac{1}{\lambda_j} \tag{19}$$

The heat flux density in the transport direction $\vec{n}$ (i.e. colinear with $\vec{\nabla} T$) is defined by:

$$Q = \sum_{\text{states } j} Q_j \tag{20}$$

$$Q_j = V_s \ \hbar\omega_j \ \vec{v}_j \cdot \vec{n} \ \delta f_j \tag{21}$$

We then introduce δf_j:

$$Q_j = V_s \ \hbar\omega_j \ \vec{v}_j \cdot \vec{n} \ \left(\vec{v}_j \cdot \vec{\nabla} T \frac{\partial f_{\mathrm{BE}}}{\partial T}(\omega_j, T)\frac{1}{\lambda_j}\right) \tag{22}$$

$$Q_j = \hbar\omega_j |\vec{v}_j \cdot \vec{n}|^2 \frac{1}{\lambda_j}\frac{\partial f_{\mathrm{BE}}}{\partial T}(\omega_j, T_{eq})\vec{\nabla} T \cdot \vec{n} \tag{23}$$

The conductivity of Eq. 11 is finally obtained from the definition of the thermal conductivity.

2.4.2.3 SA Matthiessen model

In order to model the thermal conductivities in devices with an intermediate length in which a heat transport regime between ballistic and diffuse limits occurs, we first mix the previous models by using a Matthiessen's rule. It means summing ballistic and diffusive conductivities (of Eq 11 and 9, respectively) as follows:

$$\frac{1}{\kappa_{\text{Matthiessen}}} = \frac{1}{\kappa_{\text{ballistic}}} + \frac{1}{\kappa_{\text{diffusive}}} \tag{24}$$

2.4.2.4 Spectral SA models: CPNF, IPNF and NW

More complex models based on a spectral decomposition of the thermal conductivities are usually more accurate. Thus, a specific model for each kind of studied nanostructures have been derived. Then, one model is dedicated to NanoFilms in Cross-Plane configuration (the CPNF model), another to NanoFilms in In-Plane configuration (IPNF) and the last one to nanowires (NW). In each case, the Soffer's model (see §2.3) is used to model the rough boundary scattering mechanism. In this approach, ballistic and phonon-phonon scattering rates are once again summed but their spectral dependences are considered. Indeed, the average distance over which a phonon moves along the transport direction $\vec{n}$ before colliding with a thermostat is:

$$\bar{L} = \frac{L}{2} \tag{25}$$

with L the distance between thermostats.

Similarly, in IPNF and NW models, the average distance over which a phonon moves in a transverse direction $\vec{n}_\perp$ before colliding with a rough boundary is

$$\bar{W} = W\left(\frac{1}{1-p_{\text{specular}}} - \frac{1}{2}\right) \tag{26}$$

with W the width of these devices, and by considering the probability of specular reflection p_{specular} from Eq. 4.

For these three models (NFCP, NFIP and NW), the total spectral scattering term for a state j is given by:

$$\lambda_{\text{CPNF},j} = \lambda_j + \frac{|\vec{v}_j \cdot \vec{n}|}{\bar{L}} \tag{27}$$

$$\lambda_{\text{IPNF},j} = \lambda_j + \frac{|\vec{v}_j \cdot \vec{n}|}{\bar{L}} + \frac{|\vec{v}_j \cdot \vec{n}_{\perp,1}|}{\bar{W}} \tag{28}$$

$$\lambda_{\text{NW},j} = \lambda_j + \frac{|\vec{v}_j \cdot \vec{n}|}{\bar{L}} + \frac{|\vec{v}_j \cdot \vec{n}_{\perp,1}|}{\bar{W}} + \frac{|\vec{v}_j \cdot \vec{n}_{\perp,2}|}{\bar{W}} \tag{29}$$

Finally, the associated thermal conductivities κ_{NFCP}, κ_{NFIP}, and κ_{NW} are calculated from Eq. 11 by replacing λ_j by their relevant scattering rates.

2.5 Interface thermal conductance modeling

The interface thermal conductance (ITC) is related to the temperature drop at an interface between two materials induced by a non-zero heat flux. Thus, the ITC is defined by:

$$G = \frac{Q_{\mathrm{inter}}}{\Delta T_{\mathrm{inter}}} \tag{30}$$

where Q_{inter} is the heat flux density flowing though the interface, and $\Delta T_{\mathrm{inter}}$ is the temperature drop at the interface.

It should be noted that the definition of $\Delta T_{\mathrm{inter}}$ is not trivial. The temperature at one side of the interface should be calculated (or measured) by considering only the incident phonons and not the total phonon distribution (cf. Swartz and Pohl (1989)). In the case of devices in (or close to) a diffusive phonon transport regime, these two different temperature definitions are equivalent, but they differ significantly in the case of a ballistic regime.

The two models mainly used for ITC investigation are the Diffusive Mismatch Model (DMM) and the Acoustic Mismatch Model (AMM). The full-band adaptations of AMM and DMM are detailed in (Larroque, Dollfus, and Saint-Martin 2018). In this thesis, we only investigate the DMM, which assumes a bad quality of the interface and leads to a diffusive process for every phonon crossing the interface. Then, each incident phonon can be either transmitted or reflected according to a transmission coefficient t, but in all cases it will undergo a diffusive scattering process inducing a memory loss of the incident phonon properties. Similarly to the SA ballistic model derivation for the thermal conductivity, the ITC can be theoretically estimated via a Landauer's approach. The net heat flux density at the interface between the materials A and B is determined by using a transmission coefficient $t_{A\to B}(\omega)$, which is considered to be only dependent on the angular frequency of the particles. The spectral impedance of a material A is defined for a range $\Delta\omega$ as:

$$I_A(\omega) = \frac{V_s}{\Delta\omega} \sum_{\substack{\text{states } j \\ \text{in material } A}} \hbar\omega_j^A \ \vec{v}_j^A \cdot \vec{n} \ \delta(|\omega - \omega_j^A| < \frac{\Delta\omega}{2}) \tag{31}$$

The transmission coefficient is then calculated by using the impedance of the two materials (A and B) involved in the interface:

$$t_{A\to B}(\omega) = \frac{I_B(\omega)}{I_A(\omega) + I_B(\omega)} \tag{32}$$

The final semi-analytical formula for the ITC can be written as follows:

$$G^{\mathrm{DMM}}(\omega, T) = \frac{\partial f_{\mathrm{BE}}}{\partial T}(\omega, T) I_A(\omega) t_{A \to B}(\omega) \tag{33}$$

where $G^{\mathrm{DMM}}(\omega, T)$ is the spectral decomposition of the ITC at temperature T, and f_{BE} is the equilibrium Bose-Einstein distribution.

3 Monte Carlo and Molecular Dynamics simulations

The main concepts related to the nanoheat transfer are reminded in the previous chapter. This chapter focuses on the numerical methods that have been used during this thesis to investigate the phonons in nanostructures with a particular interest for interfaces. First, an original Monte Carlo simulator partially developed during this thesis is presented, second the Molecular Dynamics simulation methods are reminded.

3.1 Monte Carlo method

The particle Monte Carlo method is a stochastic approach to solve the Boltzmann Transport Equation (BTE). In this thesis, we present a new simulator for MC phonon transport, which solves the BTE in 3D for both the real space and reciprocal space (full band approach). The required semi-empirical, i.e. the phonon dispersion and the phonon-phonon scattering rates, are parametrized in the entire 3D Brillouin zone by using *ab initio* DFT calculations (see §2.2.1).

After introducing the BTE, the model of the simulated particles is presented and the studied devices are described. Then, we detail our temperature definition and our complete algorithm. Our configuration method to adjust simulation parameters is explicated. Finally, we discuss our two phonon treatment of three phonon scattering processes, the assumption of the average elastic scatterings at rough boundaries.

3.1.1 Boltzmann Transport Equation

The Boltzmann Transport Equation (BTE) describes the time evolution of the phonon distribution function in phase space $f_j(\vec{r}, \vec{q}, t)$, where j is the phonon state, $\vec{r}$ the position in real space, $\vec{q}$ the wave-vector and t the time. Its time-dependent expression is given by:

$$\frac{\partial f_j}{\partial t} + \vec{v} \cdot \vec{\nabla} f = \left.\frac{\partial f}{\partial t}\right|_{\text{scatt}}, \tag{34}$$

where $\vec{v}_j$ is the phonon group velocity ($\vec{v}_j = \vec{\nabla}_{\vec{q}}\, \omega_j$, ω_j is the phonon angular frequency) and $\left.\frac{\partial f}{\partial t}\right|_{\text{scatt}}$ is the collision term.

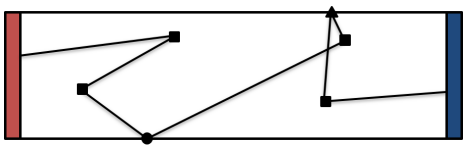

Figure 6: Schema of a possible phonon trajectory.

3.1.2 Principles of a particle Monte Carlo simulation

In order to solve the BTE, we use the particle Monte Carlo method for phonon transport (Péraud and Hadjiconstantinou 2011). In this stochastic approach, the trajectories of a large number of semi-classical particles are randomly selected. The trajectories for each particle are described as a conituous sequence of free flights (linear trajectories in real space without any change in the reciprocal space) and instantaneous scattering events (no change in real space but with a modification of the state in the reciprocal space). The scattering mechanism ending a free-flight can be either a phonon-phonon scattering or a collision with the device boundary. For each particle, the initial state, the duration of each free flight, the type and the effect of each scattering event are chosen randomly according to all relevant scattering rates. Figure 6 indicates a schematized particle trajectory in a device. The particle is first injected from a hot thermostat on the left contact. Then it undergoes several scattering processes in between its free flights. It finally exits through the cold thermostat on the right contact. At the end of a MC simulation, the phonon distribution is computed by summing over all the particles k belonging to the mode m at a given time:

$$f_m(\vec{r},\vec{q},t) = \sum_{\text{particles } k} \delta(\vec{q}-\vec{q}_k(t))\delta(\vec{r}-\vec{r}_k(t)) \tag{35}$$

It should be mentioned that only the trajectories during the steady state regime are considered here. However, the transient response could be also investigated by using our MC simulator.

3.1.3 Model of pseudo particles

To reduce the particle number and thus the computational resources, in our model each simulated particle represents a packet of N_ω phonons with a frequency ω. Considering phonon bundle with a constant number of phonons $N_\omega = N$ (and thus particles of different energies $E_p = N\hbar\omega$ according to ω) would make difficult the treatment of elastic scattering mechanisms (Klitsner et al. 1988). Thus, the number of phonons in a bundle N_ω at the frequency ω is tuned to keep constant the total energy $E_p(= N_\omega\hbar\omega)$ carried by each simulated pseudo particle (i.e. a phonon bundle). This input parameter E_p defines the energy resolution of the simulation.

3.1.4 Variance reduction and reference temperature

Only the deviation of phonon distributions from their equilibrium state are relevant to investigate heat transfer. We would like to simulate only the excess or lack of phonons with respect to their equilibrium distribution in order to limit strongly the number of studied phonons and thus the number of simulated particles. Hence, a reference temperature T^0 close to and usually below the actual temperature in the device is defined. Only the phonon bundles (the simulated particles) differing from the Bose-Enstein distribution at T^0 are simulated. Besides, each simulated particle gets a new parameter s equal to +1 (or -1)

to represent an excess (or a missing particle, respectively) with respect to the reference distribution at T^0.

For instance, the density of simulated particles in a state j in equilibrium at temperature T is:

$$n_j^{eq}(T) = \frac{\hbar\omega_j}{E_p}(f_{BE}(\omega_j, T) - f_{\mathrm{BE}}(\omega_j, T^0))\frac{V_s}{(2\pi)^3} \tag{36}$$

where f_{BE} is the Bose-Einstein distribution, and V_s the volume of a state in the reciprocal space.

This technique reduces both the simulation time and the numerical noise (see §3.1.12). All simulations presented in this work are based on this approach called "energy-based variance-reduced method" and have been developed by Péraud and co-workers (Péraud and Hadjiconstantinou 2011).

3.1.5 Effective temperature

The temperature in each device cell must be updated during the simulation, as the phonon-phonon scattering rates are temperature-dependent. The energy density-temperature relation $E_V(T)$ at equilibrium is computed by using this formula:

$$E_V(T) = \sum_{\text{state } j} \hbar\omega_j \left(f_{\mathrm{BE}}(\omega_j, T) - f_{\mathrm{BE}}(\omega_j, T^0)\right)\frac{V_s}{(2\pi)^3} \tag{37}$$

where V_s is the reciprocal volume of the state, and T^0 is the reference temperature. This function is plotted in Figure 7. A linear behavior is observed above 200K (this study is at 300K). The effective local temperature in a device cell is obtained by computing the phonon energy density. Since every pseudo particle (phonon bundle) has a constant energy, the local energy density in the device cell c is proportional to the particle density and it is given by:

$$E_{V,c} = \frac{E_p}{V_c}\sum_{\text{particles } k} s_k \tag{38}$$

Where V_c being the volume of the cell c, and s_k the sign of the particle k.

Then, the energy-temperature relationship of Eq. 37 is numerically inverted. Finally, the local temperature is $T_c = E_V^{-1}(E_{V,c})$.

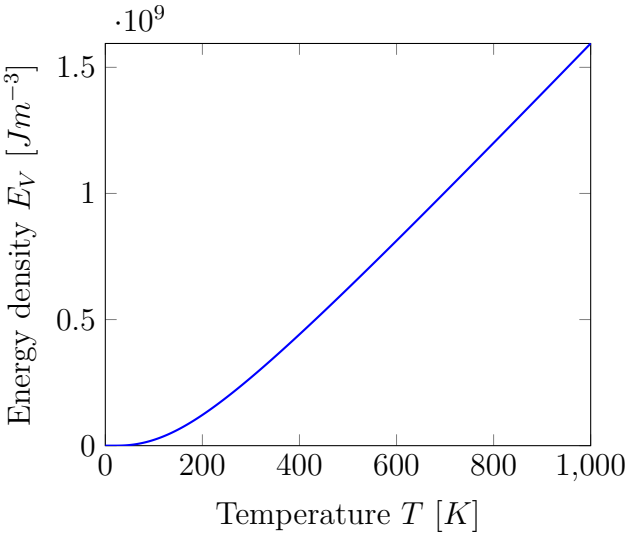

Figure 7: Phonon energy density-temperature relation in Si3C.

3.1.6 Monte Carlo Algorithm

The main Monte Carlo algorithm is presented in Figure 8. First, the initial phonon distributions of the particles are generated (§3.1.7). Two nested loops are then performed, one over time and the other one over particles. At every time step, the temperature is updated in each cell (§3.1.5), and particles are injected from the thermostats (§3.1.8.2). Then, the displacement of each particle is computed and their coordinates are updated (§3.1.6.1). During a time step, the events that can interrupt a free flight are either a collision with a cell boundary (§3.1.8.2) or a phonon-phonon scattering event (§3.1.8). At the end of the simulation, some post-processing calculations are performed to compute the final results (§3.1.8.3).

Figure 8: Main Monte Carlo algorithm.

3.1.6.1 Time of free flight and transport

The free flight corresponds to the movement of a particle between two scattering events. The scattering events can be separated in standard (bulk material) scattering mechanisms such as phonon-phonon scattering, and phonon-boundary scattering mechanisms.

Assuming Poissonian processes (cf. Jacoboni and Lugli (1989)), at the beginning of the free flight, the time before the next standard scattering event $t_{\text{scattering}}$ is randomly selected according to the following formula:

$$t_{\text{scattering}} = -\frac{\ln(n_{\text{random}})}{\lambda_j(T_c)} \tag{39}$$

where n_{random} is a uniform random number in]0;1] and $\lambda_j(T_c)$ is the total scattering rate from a phonon in a state j at a local temperature T_c. These scattering rates $\lambda_j(T_c)$ are assumed to be constant during a time step. In the general case, $\lambda_j(T_c)$ is the sum of the scattering rates corresponding to all relevant scattering mechanisms that are assumed to be independent. In this

work, only the phonon-phonon scattering rates contribute to $\lambda_j(T_c)$. They are calculated by using an *ab initio* approach as previously mentioned. This method was first developed for electron transport modeling (Jacoboni and Lugli 1989).

Besides, the time before the next boundary collision depends on the distance d between the particle and the boundaries along its transport direction. As the phonon velocity is constant during a free flight, we have

$$t_{\text{boundary}} = \min\left(\frac{d^x}{v_j^x}, \frac{d^y}{v_j^y}, \frac{d^z}{v_j^z}\right) \tag{40}$$

The actual free flight duration t_{ff} for the particle is thus limited by the first event that occurs, i.e.

$$t_{\text{ff}} = \min\left(t_{\text{remaining}}, t_{\text{boundary}}, t_{\text{scattering}}\right) \tag{41}$$

where $t_{\text{remaining}}$ is the remaining time before the end of the *i-th* time step δt for the particle. The interruption of a free flight by the end of a time step has no impact on the other scattering rates since they are Poissonian processes.

$$t_{\text{remaining}} = (t_i + \delta t) - t_{\text{current},k} \tag{42}$$

At the end of the free flight, the position in real space $\vec{r}_k$ of the particle k with a velocity $\vec{v}_j$ is updated according to:

$$\vec{r}_k(t_{\text{current},k} + t_{\text{ff}}) = \vec{r}_k(t_{\text{current},k}) + \vec{v}_j(t_{\text{current},k})t_{\text{ff}} \tag{43}$$

It should be mentioned that the wave vector is not modified during a free flight (only scattering mechanisms following the free flight have an impact on the wave vectors). Finally, the time counter of the particle is updated. New sequences of free flights and scattering events are selected until the end of the timestep.

$$t_{\text{current},k} = t_{\text{current},k} + t_{\text{ff}} \tag{44}$$

3.1.7 Initial conditions

In a cell of volume V_c, the initial number of particles N_{init,m,c} in a mode m is numerically calculated by using the equilibrium density $n^{\text{eq}}(\omega_j, T_c)$ defined in Eq. 36. Summing over all (m-mode) states, it yields:

$$N_{\text{init},m,c} = V_c \sum n_j^{eq}(\omega_j, T_c) \tag{45}$$

where E_p and T_c are the energy of a simulated particle and the local temperature, respectively.

For each initial particle, the angular frequency is selected according to a equilibrium distribution proportional to the volume of each iso-energy state. Then,

its wave-vector (reciprocal space) is randomly and uniformly selected among the iso-energy states. Using this method ensures that the repartition of energy between modes is as exact as possible. The position in the cell (real space) is also randomly selected according to a uniform distribution. Finally, the parameter s (sign) of the particle is positive if the local temperature T_c is higher than the reference temperature T_0, otherwise the parameter s is negative.

3.1.8 Scattering mechanisms

The two main phonon scattering mechanisms in Si and Ge are phonon-phonon scattering and impurity scattering. In this thesis, we ignore the impurity scatterings: the simulated materials are considered isotopically pure. However this mechanism could be easily included in our code by using for instance the relaxation time defined in (Holland 1963).

3.1.8.1 Phonon-phonon scattering mechanism

While the phonon-phonon scattering is a three-phonon process (higher orders being ignored), we approximate them as a two phonon process as proposed in the work of Lacroix, Joulain, and Lemonnier (2005). This greatly simplifies the algorithm, and since every particle has a fixed energy the conservation of energy is exact. This approximation can be considered as an average behavior of large number of phonons having a large number of collisions. A particle could undergo a phonon-phonon scattering event at the end of a free flight (i.e. $t_{\text{ff}} = t_{\text{scattering}}$). Then, the memory of the initial phonon state is lost (cf. Mazumder and Majumdar (2001)), the scattered pseudo particle (phonon bundle) is destroyed and the new one is randomly selected from an equilibrium distribution.

The probability of selecting a new state j is proportional to the equilibrium density of particles weighted by the interaction rate of that state (cf. Lacroix, Joulain, and Lemonnier (2005)):

$$p_j \propto \lambda_j(T_c) n_j^{eq}(T_c) \tag{46}$$

3.1.8.2 Boundary conditions

The faces of each cell in a device can be a thermostat, a specular boundary, a rough boundary, or a diffusive interface (ignoring the transparent interfaces between adjacent cells of the same material).

Thermostats

Thermostats inject a constant flux of particles that depends on their temperature. The number of particles injected during a time step δt through a surface is:

$$N_{\text{thermostat}}(T) = \sum_{\substack{\text{state } j \\ |\vec{v}_j \cdot \vec{n}_\perp| > 0}} \vec{v}_j \cdot \vec{n}_\perp \; A \; dt \; n_j^{eq}(T) \tag{47}$$

where $\vec{n}_\perp$ is the unit vector normal to the thermostated face and A is its area.

As each particle keeps track of its own simulated time, we initialize all of them at the beginning of the time step and make them behave as if they were injected continuously. In this calculation, it should be emphasized that the displacement of phonons during the (short) time step are assumed to be smaller than the mean free path of phonons, i.e. the transport of phonons in the thermostat is assumed to be ballistic.

Another possible method to simulate thermostats is to add a cell behind the thermostated face. Every face of that "black body" cell is specular, so that the phonon distribution inside the cell of the thermostat is constant and is equal to the equilibrium distribution at the thermostat temperature. In this "black body" cell, when a particle collides the thermostated face connected to the device, a standard specular phonon reflection occurs, and its phonon distribution remains unchanged. In parallel, a duplicated particle with the same properties as the incident phonon (position and wave vector) is created and injected (transmitted) inside the device as if the thermostated face were transparent. This last method is more accurate as it simulates completely the transport of phonons inside the thermostat but is more computationally consuming. We have implemented both methods. They all produce the same heat flux using our common simulation parameters. The direct injection at surfaces was chosen, as it is less computationally intensive.

Specular boundary

At smooth boundaries, the particle reflection is always specular, i.e. the wave-vector component normal to the surface boundary of the reflected particle ($q'_{\perp 0}$) is the reverse of the incident one ($q'_\perp = -q_\perp$).

As such specular reflections have no impact on the thermal flux parallel to the interface, they are used in our simulations to emulate semi-infinite boundaries. It should be mentioned that the implementation of specular reflection is obvious within a full-band description only if the orientation of the specular boundary corresponds to a high symmetry plane of the crystal.

Reflection at rough interface

In the case of a collision with a rough boundary, the particle has a given probability to undergo a diffusive reflection that randomizes the final wave vector instead of a specular reflection. In this work, we use the probability of specular reflections derived from the work of Soffer (1967). Its adaptation to our full-band model in detailed in §2.3

If a diffusive reflection occurs, the final state is selected among the states belonging to the same iso-energy states and with a relevant orientation of the final velocity in the case of a reflection (i.e. $\vec{v}_\perp \cdot \vec{v}'_\perp < 0$ where $\vec{v}$ and $\vec{v}'$ are the incident and reflected velocities).

Finally, the probability of each reflected iso-energy state is weighted by two factors: the complementary probability of a specular reflection for a reflected state j' with an angle $\theta_{j'}$ (from Soffer's model) and the related normal component of group velocity (as in the Lambert's law) as follows:

$$p_{\text{diffusive},j'} \propto (1 - p_{\text{specular},j'})|\vec{v}_{j'}|cos(\theta_{j'}) \tag{48}$$

This angular distribution of the final state allows the angular distribution conservation of the heat flux and leads to a net flux equal to zero at the steady state along the direction normal to the interfaces. This prevents an unphysical phonon accumulation near the rough boundary.

Transmission at semi-transparent interface

During a collision with a semi-transparent interface, the particle can be either reflected or transmitted. In our code, the phonon transmission probability $t_{A\to B}$ is implemented by using the DMM model (see §2.5) assuming fully diffusive interfaces. Thus reflected phonons as well as transmitted ones undergo an elastic diffusion (the memory of the incident phonon is lost). Our implementation of semi-transparent interface is very similar to those of rough boundaries: a new state is selected among the iso-energy states with a valid orientation of the velocity. In order to ensure self-consistency, the transmission probabilities are calculated for each direction ($A \to B$ and $B \to A$), with the same angular frequency step $\Delta\omega$ for the iso-energy states. The probability for selecting a state is weighted by the probability of the particle being reflected, and the component of its velocity normal to the interface.

$$p_{\text{DMM},j'} \propto (1 - t_{A\to B}(\omega_{j'}))\,|\vec{v}_{j'}|cos(\theta_{j'}) \tag{49}$$

3.1.8.3 Post-processings

During the simulation, at each time step and in each cell, the local temperature T_c is calculated as well as the local thermal heat flux density $\vec{J}_c$ $[Wm^{-2}]$ by summing over the contribution of all particles. The thermal conductivity of the simulated device is then calculated from the average heat flux density $\vec{J}_c$ along the transport direction $\vec{n}$, as defined in Eq. 6.

The confidence interval at 95% calculated for all simulations was found smaller than 1 $Wm^{-1}K^{-1}$ except in long devices ($L = 100$µm) for which the precision is reduced to achieve reasonable simulation times.

3.1.9 Criteria for simulation parameters

There are several simulation parameters that must be selected correctly to ensure convergence and accuracy of the simulation. An automatic process is used to define these parameters. First, we need to estimate the thermal relaxation time of the simulated device. The temperature in a cell approximately relaxes to its equilibrium value according to a negative exponential with a constant thermal relaxation time τ:

$$\Delta T_c(t) \propto \Delta T_c(0)exp(-\frac{t}{\tau}) \tag{50}$$

$$\Delta T_c(t) = T_c(t) - T_c(\infty) \tag{51}$$

Since there are two thermostats, the furthest cell is at $\frac{L}{2}$. This cell is related to the relaxation time of the device according to:

$$\tau = \frac{\partial E_V}{\partial T}(T)\frac{(\frac{L}{2})^2}{\kappa} \tag{52}$$

where E_V is the energy density, L is the length of the device and κ is an estimation of the thermal conductivity.

In Figure 9, the thermal relaxation time given by MC simulations of a CPNF is plotted as well as the results of equation 52 using the estimated thermal conductivities obtained via the ballistic, diffusive and CPNF SA formula (from §2.4).

In order to extract the relaxation time from simulation, an exponential fit is performed on the temperature of every cell as a function of time. These relaxation times are then extrapolated to the middle of the device, giving the results shown in the figure.

We thus confirm that the thermal relaxation time τ calculated from the SA CPNF thermal conductivity is a good approximation of the behavior of the MC simulations.

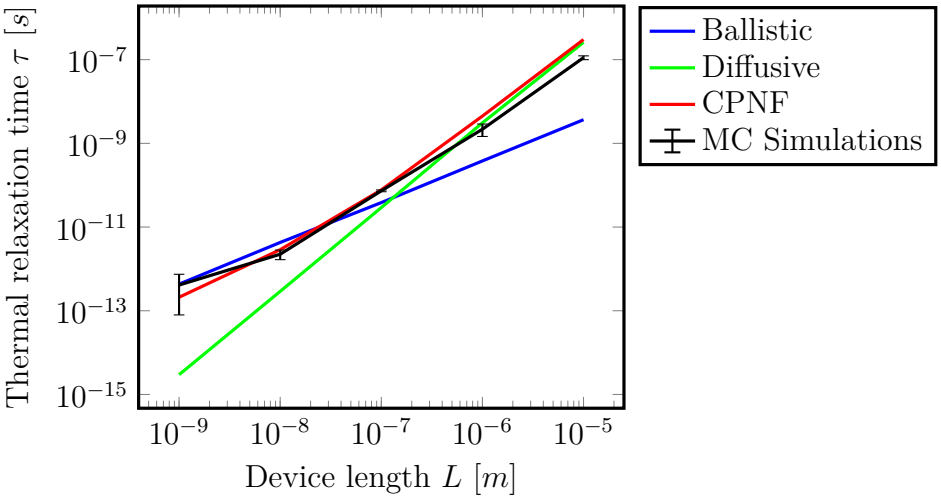

Figure 9: Estimation of thermal relaxation time τ from SA formula and MC simulations.

Using this approximation, the time step duration δT is set to $\frac{\tau}{20}$, and the temperature and heat flux are averaged every 5τ. This allows the temperature of the cells to relax progressively towards their steady-state values.

Finally, to choose a relevant particle energy E_p, the temperature fluctuation due to one particle displacement in a volume V_c is chosen to remain below δT (typically equal to 0.01K) leading to:

$$E_p = \delta T \ \frac{\partial E_V}{\partial T} \ V_c \tag{53}$$

This requirement on the precision of the temperature in each cell of the device results in an approximately constant number of simulated particles per cell, independent from their dimensions. As we modeled every device with 20 cells, all our simulations contained an average number of 20 000 coexisting particles.

For a typical device of size 1 µm × 100 nm × 100 nm in Si3C, with a 4 K-temperature difference between thermostats and a reference temperature $T^0 = 295$ K, our selected parameters were $E_p \approx 4\ 10^{-18}$ J and $\delta t \approx 1$ ns, and the simulation lasted 20 minutes on a single thread. Besides, for devices of length ranging between 1 nm and 10 µm, the timestep δt was tuned in the interval between about 0.1 ps and 100 ns.

3.1.10 Validation of two phonon approximation

During the MC simulation, the phonon-phonon scattering mechanism which is actually a three-phonon process is approximated by a two-phonon process. This approximation must conserve, at least on average, the frequency distribution of the phonon gas. By following the frequency change before and after each phonon-phonon scattering event for each simulated particle, we plot in Figure 10 the time evolution of these cumulated changes in a nanowire in the quasi-ballistic regime ($L = 1$µm, $W = 100$nm, $\Delta = 0.5$nm). The two phonon approximation appears to be consistent as the cumulated change fluctuates and remains negligible with respect to the total energy in the system ($2.6\ 10^{-18}$ J vs. $8.1\ 10^{-14}$ J, respectively).

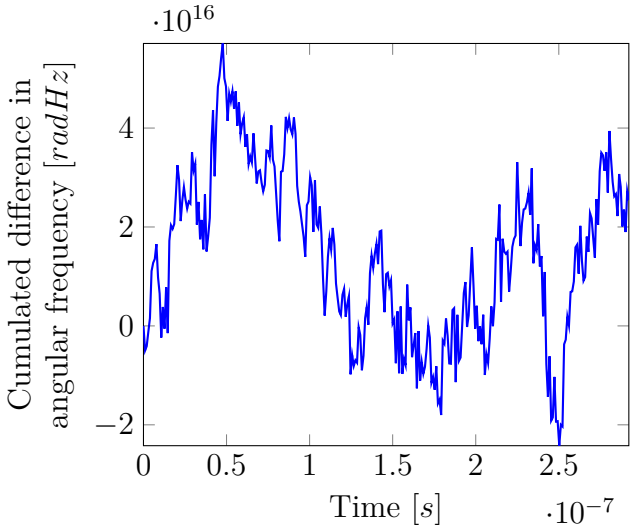

Figure 10: Time evolution of the cumulated phonon frequency change during phonon-phonon scattering events of all simulated particles in a nanowire. Parameters: $L = 1\mu m$, $W = 100nm$, $\Delta = 0.5nm$.

3.1.11 Validation of rough boundary scattering

Due to the discretization of the BZ, the elastic scattering due to rough boundaries cannot exactly conserve the angular frequency of simulated phonons. While the energy E_p of the simulated particles is exactly conserved in our algorithm, a frequency change equal to the frequency discretization step $\Delta\omega$ is possible at each scattering event. If it is not balanced, this change could impact the final frequency distribution of phonons.

To check this point, we summed these frequency changes caused by rough boundary scatterings over a complete simulation of a nanowire working in the quasi-ballistic regime (i.e. $L = 1\mu m$, $W = 100nm$, $\Delta = 0.5nm$). The time evolution of this cumulative change,plotted in Figure 11, shows a constant increasing trend. However, the total energy density corresponding to this drift during a 300 ns long simulation corresponds to an equivalent heat flux of approximately 666 Wm^{-2}, which is negligible as it is five orders of magnitude lower than the energy transfer carried by the actual heat flux of 200 MWm^{-2}.

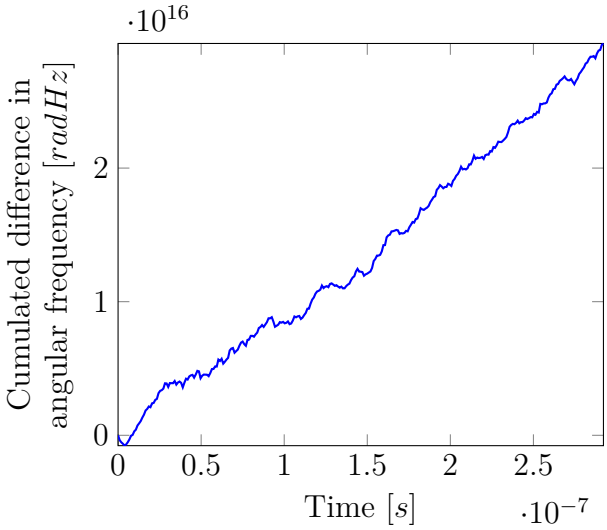

Figure 11: Time evolution of the cumulated phonon frequency change during rough boundary scattering events of all simulted particles in a nanowire. Parameters: $L = 1\mu m$, $W = 100nm$, $\Delta = 0.5nm$.

3.1.12 Validation of deviational formulation

For all MC simulations in this study, only phonons that are outside the distribution at a reference temperature T^0 are simulated in order to optimize simulation time and accuracy. In order to validate this method, we simulated a CPNF ($L = 1\mu m$, $W = 100nm$, $\Delta T = 4K$) with different T^0. The resulting temperature profiles are plotted in Figure 12. The temperature profile is less noisy when T^0 increases. Moreover, the simulation time typically decreases from 3 hours for $T^0 = 0K$ to 10 minutes for $T^0 = 300K$.

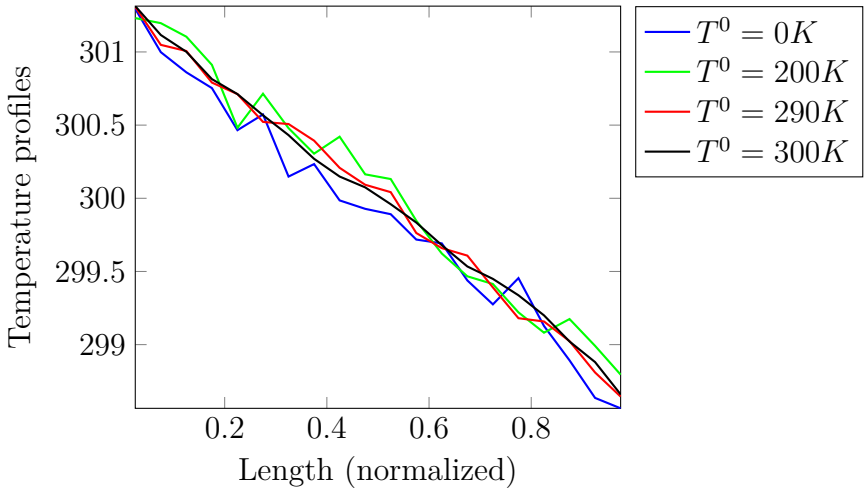

Figure 12: Temperature profiles in cross-plane nanofilms, simulated with varying reference temperature T^0, and other parameters equal.

3.2 Molecular Dynamics method

The Molecular Dynamics methods (MD) involve a classical simulation of atom trajectories. As each atomic position is given at the initialization, it is possible to model accurately the interfaces between materials by this technique.

In a MD simulation, each atom has a defined mass, position, and velocity. A time dependent Newton's second equation is numerically solved to get the atomic trajectories. The instantaneous forces of their interactions are calculated from semi-empirical potentials (depending on atomic positions). Finally, all relevant thermodynamic properties can be obtained from a statistical analysis of the system, e.g. the temperature is derived via:

$$\sum_{\text{atoms } i} \frac{1}{2} m_i |\vec{v}_i|^2 = \frac{3}{2} N k_B T \tag{54}$$

where m_i and $\vec{v}_i$ are the mass and velocitiy of the atom i, N is the number of atoms and k_B is the Boltzmann constant.

This technique is quite versatile but has some limitations. Firstly, these methods require a lot of computing power and then only small systems of thousands of atoms are manageable. In order to avoid diffusing phonons at the boundaries, periodic conditions are generally applied but the value of the phonon mean free path with respect of the size of the system or the unit cell has to be carefully considered. Secondly, the number of time steps, i.e. the actual simulation time, is commensurate and the time scale, or the frequency scale, is restricted by an empirical cut-off parameter. Finally, we should keep in mind that it is a classical simulation that cannot account for the energy quantization of phonons. MD simulations are thus limited to high temperature regimes above the Debye

temperature of the material that can be relatively high in the case of standard semiconductors.

In this thesis, the MD simulation software used was LAMMPS (Plimpton 1995). For interatomic potential for both Si and Ge, the Stillinger-Weber (Stillinger and Weber 1985) and Tersoff (Tersoff 1989) set of parameters, that includes phonon anharmonicity and 3-body interactions, have been used.

Several MD methods exist to study the thermal conductivity of materials. We detail both EMD and NEMD approaches and their advantages and drawbacks will be discussed in following chapters. The calculation of both the thermal conductivity of bulk materials, and the interface thermal conductance (ITC) is detailed.

In every method, periodic boundaries are applied to the system along all dimensions. For simulations with interfaces, this means that two interfaces are present in the system.

3.2.1 Structure and energy relaxation

At the beginning of the simulation, each atom is at its position of minimal potential energy and the distribution of their velocity is Gaussian. Therefore, before any calculation, the system must be relaxed to its equilibrium state.

For both EMD and NEMD, two steps are followed. A first run is performed in the isothermal-isobaric (NPT) ensemble at zero pressure to relax the structure of the system. Since the thermal conductivity is calculated in the micro-canonical (NVE) ensemble, a second run is then performed in this ensemble to ensure that the energy distribution is at its equilibrium.

The Si/Ge interfaces studied in §6 are perfect interfaces, and have a constant strain in each material. The lattice parameter in the direction parallel to the interface is the average of the bulk Si and Ge lattice constants. In the normal direction, the lattice parameter relaxes in both materials to maintain their density (Landry and McGaughey 2009). The polytype Ge interfaces are not strained, as there is no change of lattice parameter.

3.2.2 Bulk thermal conductivity with EMD

In EMD (Sellan et al. 2010; Schelling, Phillpot, and Keblinski 2002; Volz and Chen 2000), no external perturbations are applied during the simulation, and the thermal conductivity is calculated from a statistical study of atom properties with the Green-Kubo formula invoking the fluctuation-dissipation theorem.

During the simulation, the heat flux is calculated from the energy, stress, and velocity of each atom.

$$\vec{Q}(t) = \frac{1}{V}\left(\sum_i E_i \vec{v}_i - \sum \mathbf{S}_i \vec{v}_i\right) \tag{55}$$

where E_i is the potential and kinetic energy of atom i, $\vec{v}_i$ its velocity, $\mathbf{S}_i$ its stress tensor and V the volume of the system.

The method to obtain the stress tensor of each atom is detailed in (Thompson, Plimpton, and Mattson 2009).

The average of the autocorrelation of this heat flux is integrated according to the Green-Kubo formula (Volz and Chen 1999), giving a thermal conductivity expressed by:

$$\kappa(t_{\text{corr}}) = \frac{V}{k_B T^2} \int_0^{t_{\text{corr}}} \frac{\langle \vec{Q}(\tau) \cdot \vec{Q}(0) \rangle}{3} d\tau \tag{56}$$

where T is the equilibrium temperature.

To explore the whole phase space of the system, several independent simulations are performed (Chen, Zhang, and Li 2010). For each simulation, a black line in Figure 13 shows the evolution of the thermal conductivity as a function of the upper bound of the integral t_{corr}. Finally, an average (red line) is performed over all simulations. The error bars represent the confidence interval at 95%, calculated with:

$$\text{IC}_{95\%} = \left[\bar{x} - 2\frac{\sigma}{\sqrt{n}}; \bar{x} + 2\frac{\sigma}{\sqrt{n}} \right] \tag{57}$$

where $\bar{x}$ is average, σ the standard deviation and n the number of samples.

The value of the thermal conductivity is the average at $t_{\text{corr}} = t_{\text{cutoff}}$. At high correlation times, the integrals diverge due to the accumulation of numerical errors (as shown in Figure 13). t_{cutoff} is chosen after the first convergence (plateau of the red line) (Li, Porter, and Yip 1998) and before the increase of the standard deviation.

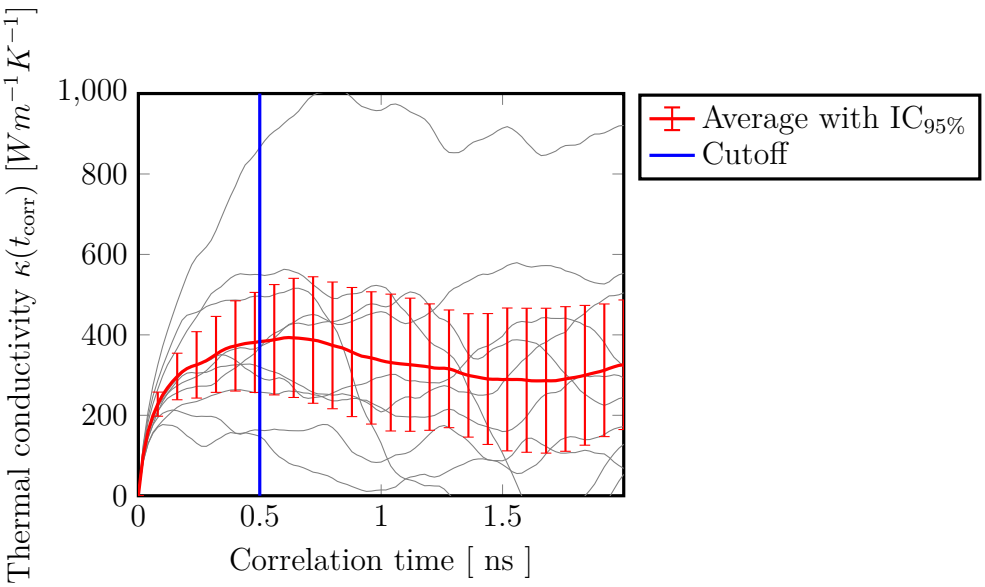

Figure 13: Evolution of the thermal conductivity as a function of the upper bound of the integral on correlation time t_{corr}. Each black line shows the result of an independent simulation. The red line shows the average, and the error bars are confidence interval at 95%.

3.2.3 Interface thermal conductance with EMD

The interface thermal conductance (ITC), instead of the previous bulk thermal conductivity, can be calculated with a similar method (Chalopin et al. 2012).

The heat flux across the interface between two volumes X and Y is:

$$Q_{\text{inter}}(t) = \frac{1}{2A}\left(\sum_{i\in X} \vec{v}_i \cdot \vec{F}_i^{Y} - \sum_{j\in Y} \vec{v}_j \cdot \vec{F}_j^{X}\right) \tag{58}$$

where $\vec{v}_i$ is the velocity of atom i velocity, $\vec{F}_i^{X}$ the interaction force on atom i from atoms in area X, and A the cross-section area of the interface.

This formula requires that the interaction potential can be calculated separately for each atom pair, and summed accordingly in order to obtain the $\vec{F}_i^{X}$. While this is trivial with the Stillinger-Weber potential which is defined by a two-body and a three-body components, this is not the case for the Tersoff potential.

As explained in §3.2.1, due to the periodic boundaries of the system, there are two interfaces. The area A used for the normalization must account for them.

The thermal conductance is then calculated from the Green-Kubo formula, with a normalization slightly different from Eq. 56:

$$G(t_{\text{corr}}) = \frac{A}{k_B T^2} \int_0^{t_{\text{corr}}} \langle Q_{\text{inter}}(\tau) \cdot Q_{\text{inter}}(0) \rangle d\tau \tag{59}$$

The results are then processed in the same way as the bulk method: the result is the average of several simulations, and the error is estimated from the confidence interval at 95%.

3.2.4 Bulk thermal conductivity with NEMD

The second kind of method that we study is NEMD. In opposition to EMD methods, their procedures are similar to experimental measurements. Perturbations are applied to the system, in our case the temperature in some regions of the system is controlled by rescaling the kinetic energy of atoms.

These two "external" thermostats induce a temperature gradient in the system and an internal thermal flux that can be calculated. The thermal conductivity is then directly obtained from its definition in Eq. 6.

Since the size of the system is small compared to the mean free path of phonons, the transport is partially ballistic between the thermostats. This means that there is a direct dependence between the calculated conductivity κ and the distance between thermostats L. In Figure 14, the relation between their inverses $\frac{1}{\kappa} = f(\frac{1}{L})$ is shown in blue. The error bars are the confidence intervals at 95%. A linear extrapolation (red line) at $\frac{1}{L} = 0$ gives the result for bulk conductivity (Schelling, Phillpot, and Keblinski 2002). The green lines are linear extrapolations of the maximum and minimum errors.

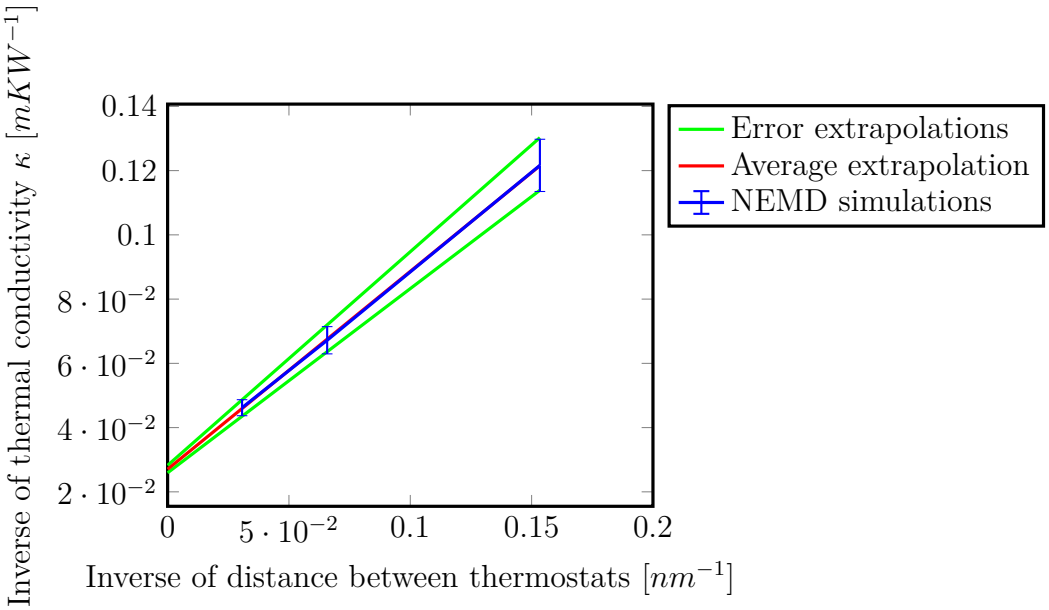

Figure 14: Inverse of thermal conductivity as a function of the inverse of the distance between thermostats, for Si at 1000K. Results from NEMD simulations (blue line). The red and green lines are the extrapolations at $\frac{1}{L} = 0$, for the average and the maximum and minimum errors, respectively.

3.2.5 Interface thermal conductance with NEMD

To calculate the ITC, each thermostat is placed in a different material as represented in Figure 15. White and grey volumes describe two different materials, for instance Silicon and Germanium. The red and blue hashed volume are respectively the hot and cold thermostats.

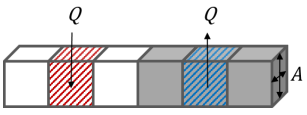

Figure 15: Diagram of the simulation box for simulating an interface in NEMD.

In addition to the thermal gradient inside the materials, there is a temperature drop ΔT at the interfaces due to the Kapitza resistance. In order to estimate it, we calculate the average temperature in slices of the simulation box, along the transport direction. The resulting temperature profile is shown in Figure 16 where the white and grey backgrounds represent the different materials, and the red and blue hashed areas represent the hot and cold thermostats. A linear interpolation of the temperatures far from the interfaces and thermostat is used to extrapolate the temperature at both sides of the interface, giving a precise estimation of ΔT.

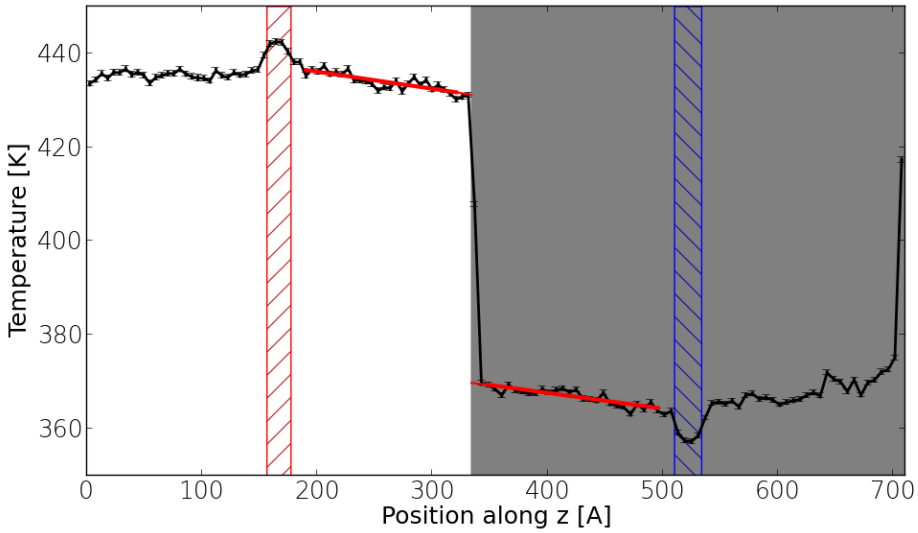

Figure 16: Temperature profile of the simulation box along the transport direction of a Si/Ge interface with NEMD.

The ITC is then calculated from its definition in Eq. 30.

Only the property of the interface is taken into account by this temperature drop ΔT_{inter}. In contrast to the bulk conductivity calculations in §3.2.4, the ballistic transport between the thermostats and the interface is not related to length dependence of the ITC. Thus, the calculated value does not need to be extrapolated from several sizes of simulation boxes.

An issue with the NEMD methods is that the rescaling of atom kinetic energy by the thermostats induces an out of equilibrium phonon distribution in the thermostats. Since at our simulation scales the transport is partly ballistic, the equilibrium distribution is never recovered between the thermostats, or at the sides of the interfaces. The definition of temperature is then unclear.

4 Bulk materials and thin films

This chapter focusses on the thermal properties in both bulk materials and thin films. Molecular Dynamics (MD) simulations have been performed in order to test the different methods and benchmark them against previous results. Meanwhile, our Full Band Monte Carlo (MC) simulator based on *ab initio* parameters were used to study the anisotropy of Si and Ge in several crystalline phases. By using these advanced numerical simulations, several semi-analytical (SA) models of the thermal conductivity in a quasi-ballistic regime are discussed.

4.1 Bulk thermal conductivities by using MD

This section is dedicated to MD simulations, and bulk thermal conductivities of Si and Ge are calculated. For Silicon both the cubic and the hexagonal phases are investigated.

The thermal conductivities are calculated by using both Equilibrium and Non Equilibrium (EMD and NEMD) methods. Stillinger-Weber (SW) and Tersoff (Ter) potentials are used and their related results are discussed. The time step is 1 fs. For each simulation, two preliminary relaxation steps (see §3.2.1) during 40 ps (in simulation time) are performed. The heat flux is calculated by averaging over the next simulated 120 ps. The final thermal conductivity is an average over 20 independent runs. For EMD, we found that a simulation of 8-unit cells along each dimension is the minimum size to compute size independent conductivities.

The results from Si and Ge at $T = 1000$K are presented in Table 1 and Table 2. As $T = 1000$K is higher than the Debye temperatures of these materials, that are equal to 640K and 374K, respectively, a MD approach is relevant. Besides, in this temperature regime the phonon mean free path is lower than the system length and the computed thermal conductances are size independent.

For the sake of comparison, previous MD results extracted from (Sellan et al. 2010) and (Schelling, Phillpot, and Keblinski 2002) are also shown. Besides, experimental values from (Capinski et al. 1997) and (Ruf et al. 2000) for isotopically pure Si (as considered in our simulations) as well as (Ozhogin et al. 1996) for pure Ge are indicated. These values given at 1000K are derived from an extrapolation from measurements at lower temperatures.

	$\kappa\ Wm^{-1}K^{-1}$
Exp. Capinski	44
Exp. Ruf	45.8
NEMD Ter.	49.7 ± 1.2
NEMD SW	52.7 ± 1.7
NEMD SW Sellan	40 ± 8
NEMD SW Schelling	65 ± 16
EMD Ter.	77.2 ± 21.3
EMD SW	60 ± 17
EMD SW Sellan	60 ± 12
EMD SW Schelling	62 ± 16

Table 1: Si bulk thermal conductivity at 1000K from EMD and NEMD.

	$\kappa\ Wm^{-1}K^{-1}$
Exp. Oz	15
NEMD Ter.	19.7 ± 0.5
NEMD SW	28.5 ± 0.4
EMD Ter.	32.9 ± 8.0
EMD SW	82.8 ± 27.4

Table 2: Ge bulk thermal conductivity at 1000K from EMD and NEMD.

Our MD results are consistent with previous MD simulations. According to our error estimations, they overestimate the experimental values. Besides, Ge results within the EMD method using Stillinger Weber potential appear disappointing and only the Tersoff potential will be used in the following for Ge study.

In Table 3, the thermal conductivity at $T = 1000$K of cubic and hexagonal phases of Si and Ge are compared by using the EMD method with Tersoff potential.

	Si	Ge
Cubic	77.2 ± 21.3	32.4 ± 7.2
Hexagonal	72.0 ± 16.8	31.6 ± 11.2

Table 3: EMD bulk conductivity at 1000K in cubic and hexagonal phases of Si and Ge, with Tersoff potential.

Both the hexagonal phases of Si and Ge show a slight reduction in thermal conductivity with respect to their cubic counterpart. Although the hexagonal phases are anisotropic (as we will see later), it should be noted that in EMD, a pseudo isotropic thermal conductivity is calculated because the method averages the contribution of all directions.

The thermal conductivities are calculated in both cubic and hexagonal Si (resp. named Si3C and Si2H) with the SA diffusive formula (see Eq. 11), at $T = 1000$K like in MD and $T = 300$K, in Table 4. The hexagonal phase is studied in two lattice orientations: [10-10] (Si2Hx) and [0001] (Si2Hz).

Materials	κ at $T = 300$K	κ at $T = 1000$K
Si3C	138.5	36.9
Si2Hx	100.3	27.2
Si2Hz	74.1	20.6

Table 4: SA bulk conductivities at 1000K and 300K in cubic and hexagonal Si.

At 1000K, we find that the Si3C results with SA underestimate both the experimental thermal conductivities and the MD ones. We confirm that the hexagonal phases have a reduced conductivity, even more than in MD. A strong anisotropy between Si2Hx and Si2Hz is also observed. One should keep in mind that these values are derived without considering any phonon-impurity scattering mechanism (with just phonon-phonon scattering) and thus this value underestimates the experimental measurements of isotopically pure Silicon (Ruf et al. 2000). However, it is a good estimation of the thermal conductivity of natural Silicon at ambient temperature. Hence, no other scattering mechanism is taken into account in our study of bulk Si.

4.2 Ballistic to diffusive transition in thin films

By using Monte Carlo simulations, this section studies the transition of thermal properties between bulk material in which the thermal transport is diffusive and cross-plane nanofilms (CPNF) in which the thermal transport is quasi-ballistic. Several semi-analytical (SA) models are compared to Monte Carlo (MC) simulations. Both the cubic and hexagonal phases of Si are investigated. The angular frequency distribution of both the energy and heat flux are carefully studied. Finally, in order to explore the anisotropy of thermal transport, the angular distribution of the heat flux is checked.

All the following calculations are performed at an average temperature of $T = 300$K, with a temperature difference between the thermostats of $\Delta T = 4$K, and a reference temperature of $T^0 = 295$K for the MC algorithm (see §3.1.4).

4.2.1 Comparison between models in cubic Si

In this section and the following, we investigate the influence of the length L on the thermal conductivities κ of CPNF calculated with several methods:

- MC simulations,
- SA ballistic model (cf. Eq. 9). It is linearly dependent on L and corresponds to the short film asymptotic behavior,
- SA diffusive model (cf. Eq. 11). It is this independent of L and corresponds to the long film asymptotic behavior,
- SA Matthiessen model (cf. Eq. 24). It is a kind of average between the 2 previous models that is widely used to investigate CPNF,
- SA CPNF model (cf. Eq. 27). This model is a frequency dependent evolution of the previous model.

Figure 17 shows for cubic Silicon (Si3C) at 300K the thermal conductivities along the [100] lattice orientation. At long L, all the models (but the ballistic one) converge to the diffusive value of thermal conductivity: $\kappa_{\text{diffusive}} = 138$ $Wm^{-1}K^{-1}$, which corresponds to the bulk conductivity. Likewise, except the diffusive model, they asymptotically converge at short L to the conductance of the ballistic model. This confirms that the models are equivalent at these limits.

We should note that for device length L shorter than 10nm, i.e. at the atomic scale, the considered phonon dispersion relation is not relevant and the indicated MC results are just a guide for the eyes illustrating the asymptotical behavior.

There is a gradual transition between the two asymptotic behaviors. This transition is often modeled in the literature by using the Matthiessen model. However, we find that this modeling exhibits a strong discrepancy with MC results at intermediate length. For instance, at $L = 200$nm, the SA model overestimates the conductivity by 60%. Meanwhile, the SA CPNF model is much more accurate leading to an error lower than 4% for all film lengths. Thus, the SA CPNF requiring much less computational resources than the complex MC simulations reproduces the MC results with a very good accuracy. This shows that a spectral treatment of the heat flux is necessary to correctly model the transition between ballistic and diffusive regimes.

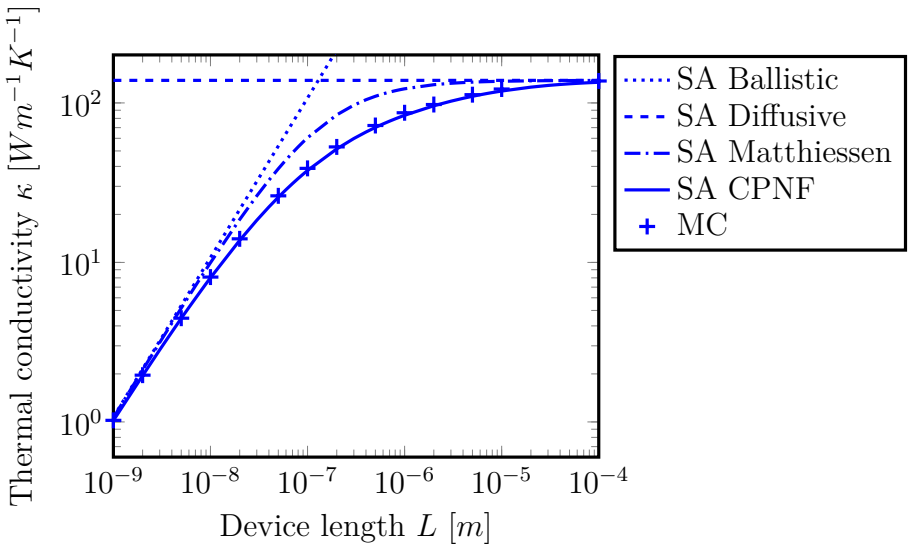

Figure 17: Thermal conductivities in CPNF as function of film length, in Si3C.

4.2.2 Comparison between cubic and hexagonal phases of Si

The evolution of the Si thermal conductivity κ in the cubic phase (Si3C, in blue) is plotted in Figure 18 similarly as in the previous section and this evolution is compared to those in the hexagonal phase. Two lattice orientations of the hexagonal phase are considered: [10-10] (Si2Hx, in green) and [0001] (Si2Hz, in red). While all the curves have the same behaviors, Si2Hx and Si2Hz always

exhibit lower κ than cubic Si. For instance, at the diffusive limit, i.e. in long films, $\kappa_{\text{diffusive}} = 138$, 100 and $74 W m^{-1} K^{-1}$ for Si3C, Si2Hx and Si2Hz respectively. Besides, these results show an anisotropy between the two hexagonal phase orientations. The anisotropy leads to a $\kappa_{\text{diffusive}}$ 26% higher in the Si2Hx.

We also confirm that the SA CPNF provides impressively accurate results for all these materials.

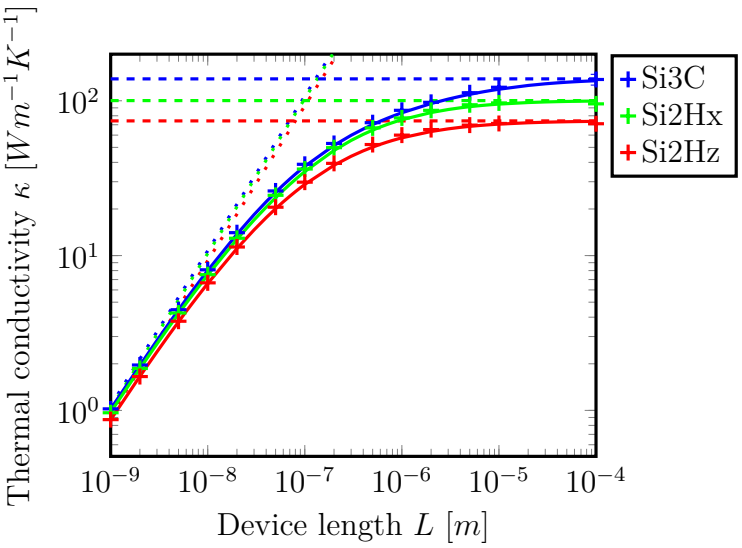

Figure 18: Thermal conductivity in CPNF as function of device length L, in Si3C (blue), Si2Hx (green) and Si2Hz (red).

4.2.3 Spectral distributions of energy and heat flux

The previous sections show that the SA CPNF model provides good estimates of the thermal conductivity due to its accurate spectral distribution of the thermal conductivity and thus of the heat flux. In order to study the spectral thermal properties, the average spectral energy and heat flux in a MC simulation are investigated in this section.

In a MC simulation at the steady state, the spectral energy density $E_{\text{MC}}(\omega)$ of phonons in the nanofilm is computed. In a device cell (i.e. between $\vec{r}$ and $\vec{r}+\vec{dr}$), the time spent by each particle in all energy states (i.e. between each ω and $\omega + \delta\omega$) are summed. This average occupation distribution of each state $f_{\text{MC},j}$ gives the average spectral energy density $E_{\text{MC}}(\omega)$ as:

$$E_{\text{MC}}(\omega) = \frac{E_p}{V_c} \sum_{\text{states } j} f_{\text{MC},j} \delta \left(|\omega - \omega_j| < \frac{\Delta\omega}{2} \right) \tag{60}$$

where V_c is the volume of the considered device cell.

At equilibrium, the theoretical spectral energy density $E_{\text{th}}(\omega)$ is given by the Bose-Einstein distribution. We should note that the distribution at the reference temperature $T^0 = 295\text{K}$ is removed as in the MC simulations. It yields:

$$E_{\text{th}}(\omega) = \frac{V_s}{(2\pi)^3} \sum_{\text{states } j} \hbar\omega_j \left(f_{\text{BE}}(\omega_j, T) - f_{\text{BE}}(\omega_j, T^0) \right) \delta \left(|\omega - \omega_j| < \frac{\Delta\omega}{2} \right) \tag{61}$$

where V_s is the reciprocal volume of a state in the BZ.

Similarly, the spectral heat flux density is calculated by summing for each state the product of their occupation and their related velocity in the transport direction $\vec{n}$.

$$Q_{\text{MC}}(\omega) = \frac{E_p}{V_c} \sum_{\text{states } j} f_{\text{MC},j} \ \vec{v}_j \cdot \vec{n} \ \delta \left(|\omega - \omega_j| < \frac{\Delta\omega}{2} \right) \tag{62}$$

For the sake of comparisons, in the SA CPNF model, the spectral heat flux density is given by:

$$Q_{\text{CPNF}}(\omega) = \frac{\Delta T}{L} \frac{V_s}{(2\pi)^3} \sum_{\text{states } j} \hbar\omega_j (\vec{v}_j \cdot \vec{n})^2 \frac{1}{\lambda_{\text{CPNF},j}} \frac{\partial f_{BE}}{\partial T}(\omega_j, T) \delta \left(|\omega - \omega_j| < \frac{\Delta\omega}{2} \right) \tag{63}$$

We show in Figure 19 the angular frequency distribution of the phonon energy in CPNFs with an intermediate length (at $L = 1\mu\text{m}$) in Si3C and Si2H. The spectral energy is shown separately for each phonon mode. Crosses represent the MC values and lines are for the theoretical values from the SA CPNF model. We can see that there is no discrepancy between Si2Hx and Si2Hz spectra as the energy is not dependent on the lattice orientation.

We observe that the MC and theoretical approaches give the same result in terms of energy. This means that the particles in the MC simulation are not strongly out of equilibrium, as it is expected for these simulation parameters (length and temperature bias).

In Figure 20, the integral of the angular frequency distribution of the heat flux is plotted for 1 µm long CPNFs made of Si3C, Si2Hx and Si2Hz. The contributions of each mode are indicated with different colors. The integral of the distribution is used here instead of the spectral distribution of the heat flux as it is less noisy and also indicates directly the total contribution of each mode (at the highest frequency).

The evolutions of all spectral distributions are similar to the SA CPNF model, especially in the case of Si3C. However, the total contributions of each mode differ. Moreover, for some modes at high angular frequency (i.e. in the optical modes), a negative contribution to heat flux can be observed in MC results that are not present in the SA model. For instance, in the case of Si2Hz, the 6th mode has a clear negative contribution. We explain this phenomenon by the

fact that the diffusive approximation used in SA CNPF model only account for positive velocities, as only their absolute values are used. These 'negative' velocities are particularly present in optical modes at higher angular frequencies and corresponds to the observed negative contributions. Thus, total heat fluxes computed by the SA model are higher than these computed by using MC. This is consistent with the lower SA thermal conductivities previously discussed.

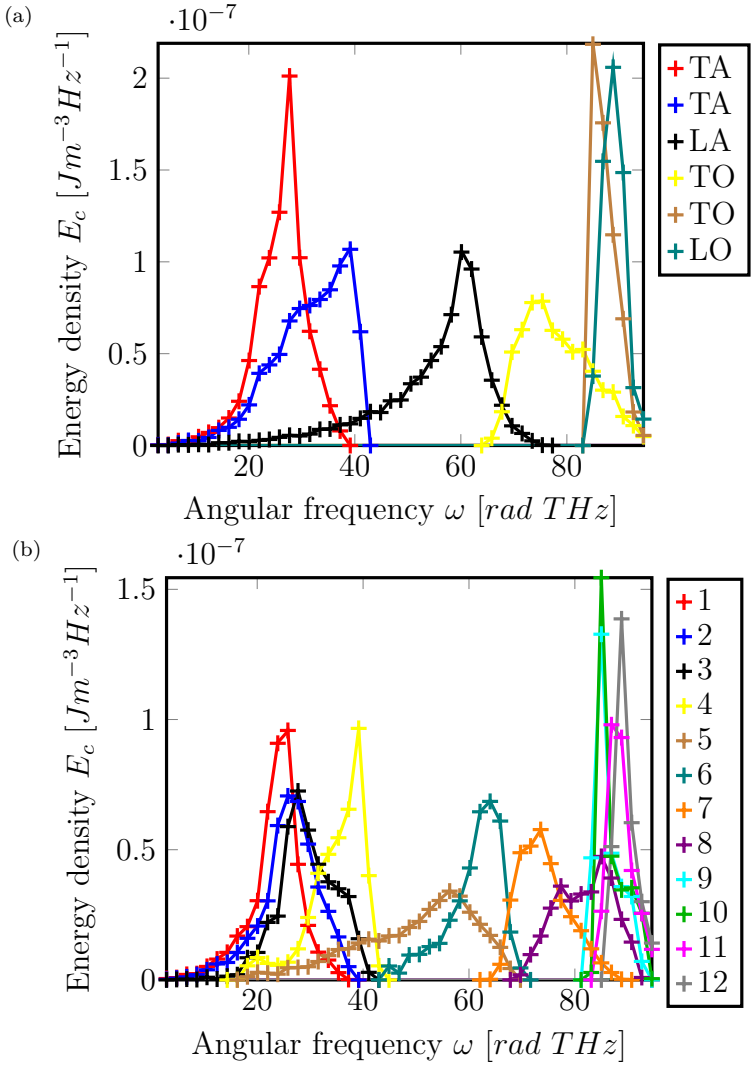

Figure 19: Spectral distribution of the phonon energy for each mode in a 1µm long CPNF. (a) Si3C (b) Si2H. Crosses for MC. Lines for SA CPNF.

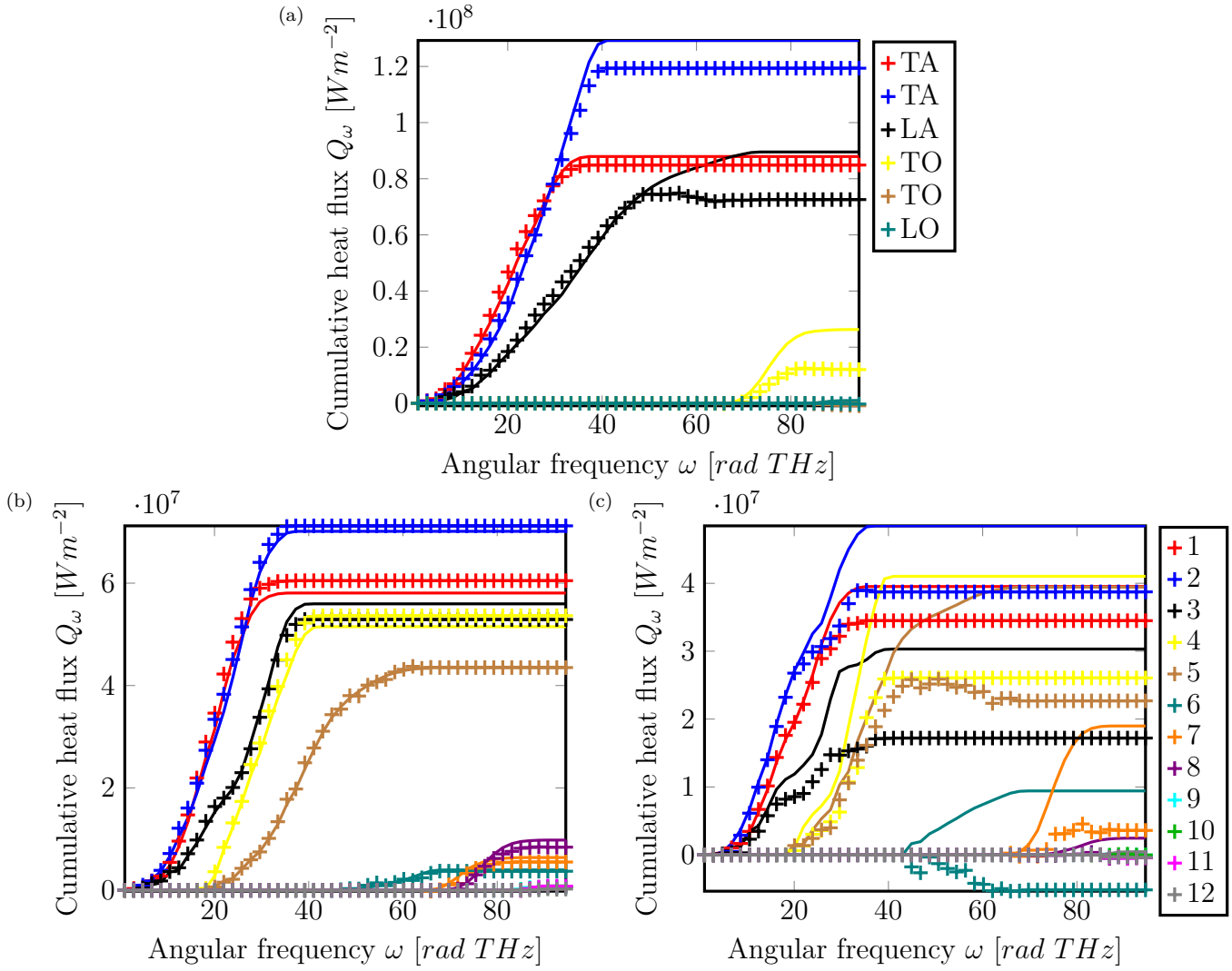

Figure 20: Cumulative spectral distribution of the heat flux in a 1µm long CPNF. (a) Si3C, (b) Si2Hx and (c) Si2Hz. Crosses for MC simulations, continuous lines for SA CPNF model.

The total contributions of each mode to the heat flux are also indicated in Table 5, (a) for Si3C, (b) for Si2Hx and (c) for Si2Hz. The modes are numbered by ascending energy values. As expected, the heat flux is mainly carried by acoustic modes: 96% for Si3C, 61.1% for Si2Hx (with 33.4% in 4th to 6th modes), 66.4% for Si2Hz (with 32.0% in 4th to 6th modes). In Si3C, the 5th and 6th (TO) modes have a negative net contribution. However, the absolute value of the contribution is in the order of magnitude of the margin error of the MC simulation. In Si2H, modes higher than the 8th mode carry a negligible amount of heat.

(a)

Mode	Heat flux contribution
1 (TA)	29.5%
2 (TA)	41.5%
3 (LA)	25.2%
4 (TO)	4.2%
5 (TO)	−0.3%
6 (LO)	−0.1%

(b)

Mode	Heat flux contribution
1	20.0%
2	23.6%
3	17.5%
4	17.8%
5	14.4%
6	1.2%
7	1.8%
8	2.8%
9	0.22%
10	0.22%
11	0.27%
12	0.08%

(c)

Mode	Heat flux contribution
1	25.3%
2	28.4%
3	12.6%
4	19.1%
5	16.6%
6	−3.8%
7	2.6%
8	−0.32%
9	−0.02%
10	−0.01%
11	−0.33%
12	−0.28%

Table 5: Heat flux contribution per mode in 1µm long CPNF, (a) in Si3C, (b) Si2Hx, and (c) in Si2Hz.

4.2.4 Angular distribution of heat flux

Our full band description of the phonon dispersion in each material allows to account for the anisotropy of the thermal conductivity. In order to estimate it, the angular distribution of the heat flux is plotted in Figure 22.

In Figure 22 (a), (c), and (d), we represented the 'angular density of state' (aDOS) of Si3C, Si2Hx and Si2Hz, respectively. In our convention, the heat transport direction in a CPNF is always set towards the positive X axis. It is important to note that this angular analysis is performed in real space (not in the wave vector space). We consider a unit sphere, and discretize it along its spherical coordinates, i.e. the polar and azymuthal angles θ and ϕ. The definition of these angles is reminded in Figure 21. For each solid angle (real space direction), we sum the contribution of all the discrete states in the BZ (reciprocal space) of the material that have this phonon velocity orientation i.e. toward that solid angle, around the corresponding θ and ϕ.

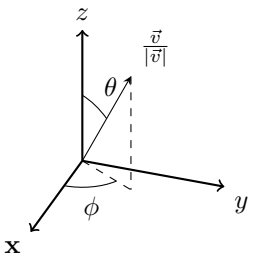

Figure 21: Spherical coordinates, showing the polar angle θ and the azymuthal angle ϕ.

To summarize, the aDOS is simply the number of states (per unit volume) in each solid angle, normalized by their area $S_{\Delta\theta,\Delta\phi}$.

$$\text{aDOS}(\theta,\phi) = \frac{V_s}{(2\pi)^3 \; S_{\Delta\theta,\Delta\phi}} \sum_{\text{states } j} \delta\left(|\theta-\theta_j| < \frac{\Delta\theta}{2}\right) \; \delta\left(|\phi-\phi_j| < \frac{\Delta\phi}{2}\right) \tag{64}$$

We observe a high aDOS in the main lattice directions of each phase:

- for Si3C, <110> are the highest, followed by <100> and <111>.
- for Si2H, <10-10> and <0001> have high aDOS, followed by <21-30>.

The aDOS in the hexagonal phase is higher along its main orientations than in its cubic counterpart as there are only 14 main directions in Si2H (6 <10-10>, 6 <21-30> and 2 <0001> directions) lower than the 22 main directions in Si3C (6 <100>, 8 <110> and 8 <111> directions).

In Figure 22 (b), (d), and (f), the angular distribution of the heat flux density is shown in Si3C, Si2Hx and Si2Hz, respectively. The average occupation of states during MC simulations $f_{\text{MC},s}$ is used to calculate the heat flux. Differently from the process presented for the aDOS, to compute the angular heat flux, the (negative or positive) contribution of the state will depend on the sign of the X component of its velocity.

$$Q_{\text{MC}}(\theta,\phi) = \frac{E_p}{V_s \; S_{\Delta\theta} \; \Delta\phi} \sum_{\text{states } j} f_{\text{MC},j} \; \vec{v}_j \cdot \vec{n} \; \delta\left(|\theta-\theta_j| < \frac{\Delta\theta}{2}\right) \; \delta\left(|\phi-\phi_j| < \frac{\Delta\phi}{2}\right) \tag{65}$$

The figures showing the angular heat fluxes are relatively noisy especially along the directions in which the aDOS is low, as only few MC particles are present. In the three cases, as expected, the main contribution is oriented directly towards the transport direction ($\theta = 0$ and $\phi = 0$). However, in Si3C, the heat flux along the <111> directions is higher than along the <110> directions even though their aDOS is lower. Similarly, in Si2Hx, the <21-30> directions contribute more than the <10-10> ones.

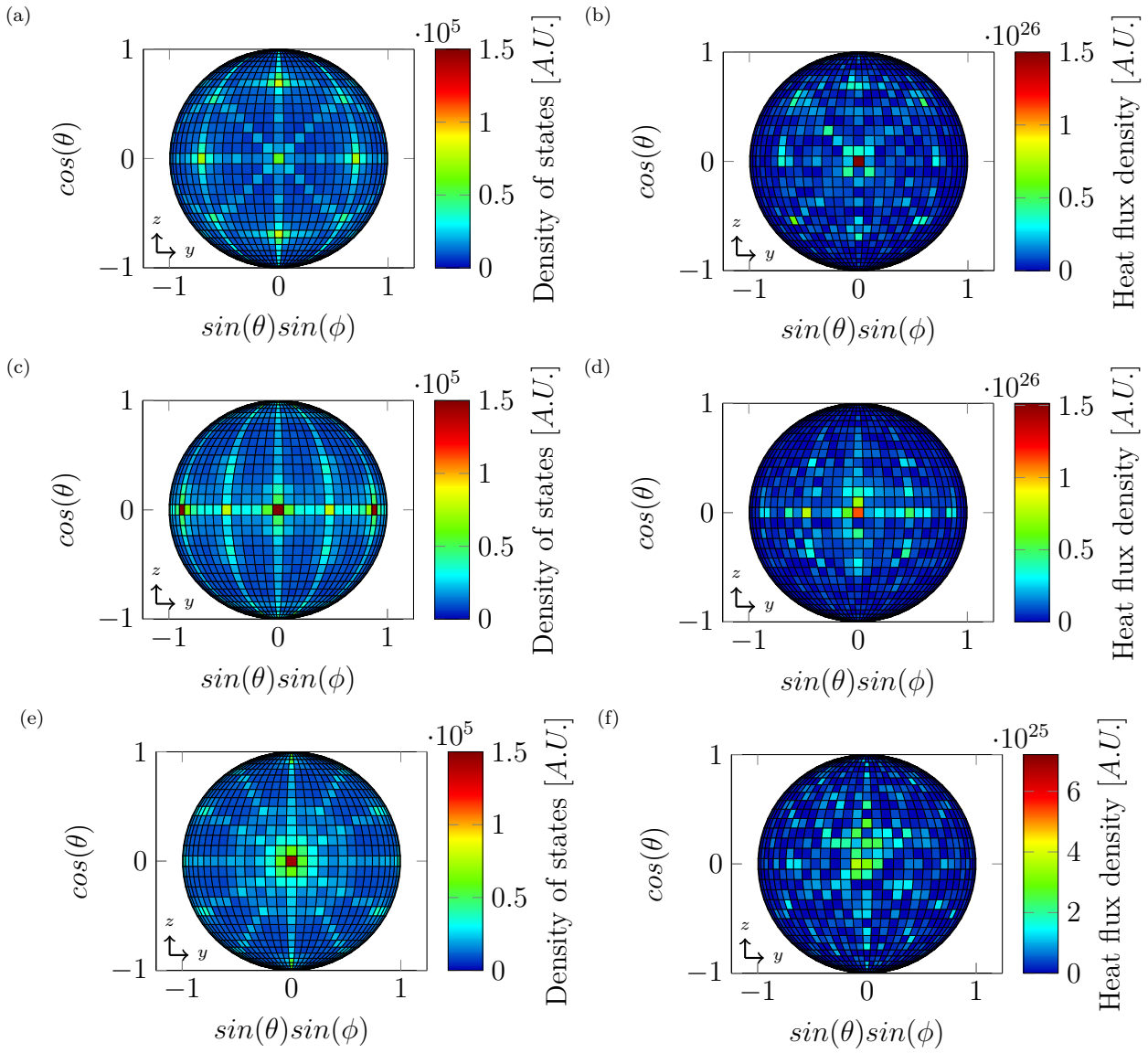

Figure 22: Angular density of state and angular heat flux in Si3C, Si2Hx and Si2Hz, in a 1µm long CPNF. (a), (c), and (e) are the aDOS, (b), (d), and (f) are the angular heat fluxes, in Si3C, Si2Hx and Si2Hz, respectively

Figure 22 clearly shows the spherical distribution of the heat flux in 2D. In Figure 23 the angular heat flux dependence over the polar and azymuthal angles θ and ϕ are plotted independently (i.e. an integration is performed over the other angle). Parts (a), (b), and (c) correspond to Si3C, Si2Hx, and Si2Hz, respectively.

In an isotropic system, the angular distribution of the flux is expected to be a smooth cosine function (as in the Lambert's distribution). But in both cubic and hexagonal phases, the angular distributions exhibit peaks revealing that the

heat flux is mostly transported along specific orientations. Each peak and their related orientations are labeled in the figures.

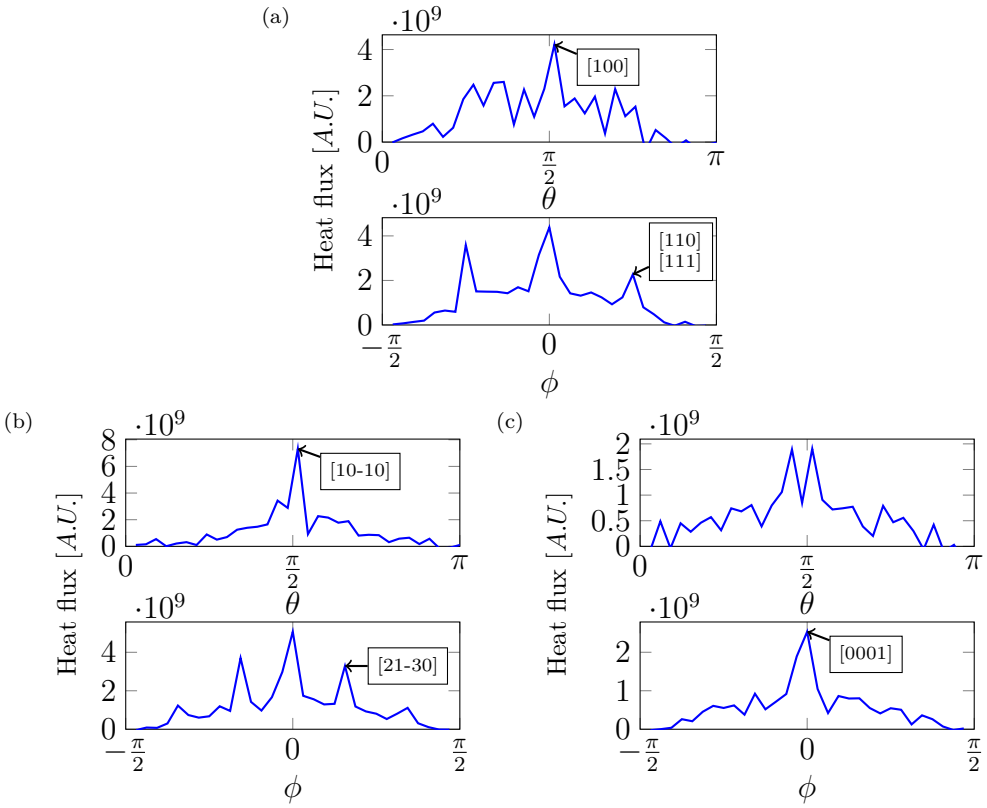

Figure 23: Angular heat flux as function of the polar θ and azymuthal angles ϕ in Si3C, Si2Hx, and Si2Hz.

4.2.5 Angular distribution of heat flux in an isotropic material

In our full band model, state discretization in the reciprocal space that is not very fine ($N = 31 \times 31 \times 31$ for Si3C), in particular near the Γ point. In order to check the impact of our mesh on the computed angular heat flux, we have created an artificial isotropic material having the same dispersion along all directions. For this material, the angular frequencies for the wave vectors in the main direction [100] of Si3C is used as a reference for all the 6 modes. Then for each state in the BZ, its angular frequency is computed according to its distance from the Γ point (i.e. the norm of their wave vector). The norm of the velocities is calculated similarly and the direction of the velocity is parallel to the wave vector. Likewise, the isotropic phonon-phonon scattering rates are interpolated along the [100] direction.

The angular DOS and the angular distribution of heat flux computed in a 1µm long CPNF in this isotropic material is shown in Figure 24. The aDOS in Figure 24 (a) has a slight bias in the main direction [100] and in the planes

between them, but it is clearly negligible compared to the features visible in the aDOS in previous materials in Figure 22 (a), (c) and (e). In Figure 24 (b), the angular heat flux is very diffuse in the whole hemisphere.

We thus confirm that our discretization of the BZ is sufficient to capture the anistropy of the heat transport in the studied materials.

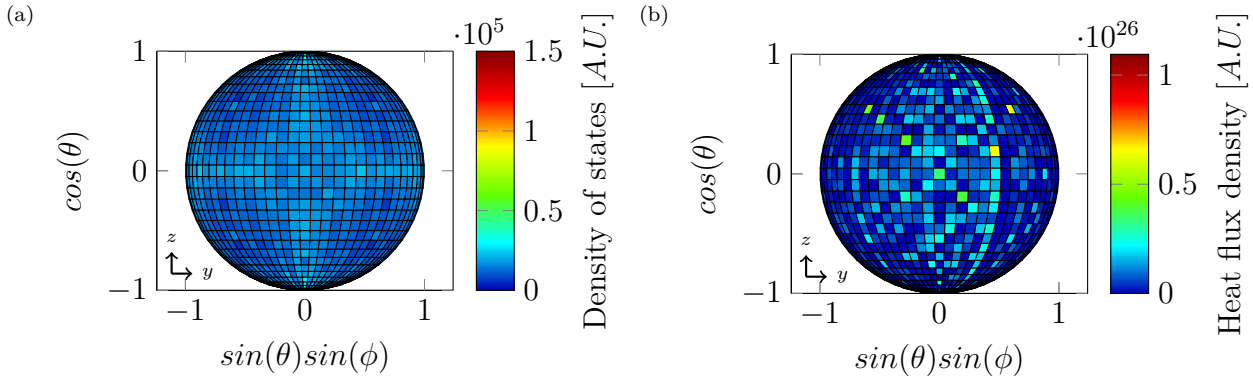

Figure 24: (a) Angular density of state and (b) angular heat flux in an artificial isotropic material, in a 1µm long CPNF.

5 Rough nanostructures

While the previous chapter details the thermal properties of thin films in the cross-plane configuration, here we consider thin films in the in-plane configuration (IPNF) with 2 rough interfaces and nanowires (NW) with 4 rough interfaces (the surrounding external boundaries), as defined in §2.1. In this chapter, we study the effect of rough boundaries in nanostructures by using our MC method including the phonon-rough interface scattering mechanism (cf. §3.1.8.2). As done in §4 for CPNFs, the evolutions of thermal conductivity, and the spectral and angular distributions of the heat flux are studied. The accuracy of the SA model to model rough IPNFs and NWs is discussed. By using a fully diffusive model for rough boundaries in the MC code, the thermal transport along several lattice orientations is investigated and compared with experimental measurements.

5.1 Effect of rough boundaries in IPNFs and NWs

5.1.1 Device geometry

In IPNFs and NWs, the device geometry is mainly characterized by 2 parameters:

- their length L, or distance between thermostats along the X axis,
- their width W, or distance between the rough boundaries (cf. Figure 3).

This section shows the dependence of the thermal conductivity on these parameters.

In Figure 25, the evolution of the thermal conductivity κ with the device length L is shown for IPNFs and NWs of width $W = 100$nm and roughness parameter $\Delta = 0.5$nm. For the sake of clarity, it should be mentioned that the figure is a semilog plot that differs from log-log axes used for similar figures presented in the previous chapter. For $L = 100$µm, κ that is equal to 138 in CPNFs is reduced down to 87 and 69 $Wm^{-1}K^{-1}$ in IPNFs and NWs respectively. As expected, the degradation of the thermal conductivity is directly related to the number of rough boundaries in long devices in which the heat transport is diffusive. However, in ultra-short devices in which the heat transport is ballistic, the thermal conductivity evolutions are the same whatever the number of rough interfaces (2 in INPF and 4 in NW). More interestingly for devices having rough boundaries, the semi-analytical models (SA), indicated in solid lines, do not fit MC results for IPNFs and NWs as well as in the case of CPNFs. For $L = 10$µm, the CPNF, IPNF and NW SA results are 2%, 5% and 12% lower than the corresponding MC result, respectively. And for $L = 1$µm, the CPNF, IPNF and NW SA results are 3%, 8% and 14% lower than the corresponding MC result, respectively.

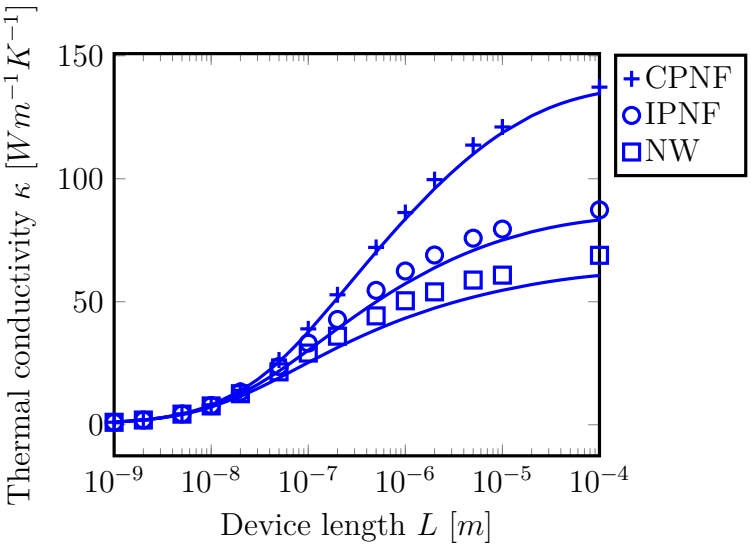

Figure 25: Thermal conductivity as function of device length in Si3C for CPNF +, IPNF ○ and NW □.

For the same 3 different devices with a length $L = 1\mu m$ and $\Delta = 0.5nm$, Figure 26 shows the evolution of κ as a function of the device width W. As all devices have a length of $L = 1\mu m$, an intermediate heat transport regime occurs mixing ballistic and diffusive transports. For $W = 1nm$, κ is 16 and 6 $Wm^{-1}K^{-1}$ for IPNF and NW, resp. The increase of κ with the increase of W in IPNF and NW exhibit a similar behavior. For intermediate width of $1\mu m$, κ reaches 95% and 90% of the CPNF conductivity in IPNF and NW, resp. For devices wider than $1\mu m$ in which $W > L$, the impact of rough boundaries is weak, and the cross-plane conductivity is recovered with a difference lower than 5%. For thinner devices i.e. for W in the range of 10 nm to 200 nm, the width of the device impacts on the thermal conductance by a factor of about 30 $Wm^{-1}K^{-1}$ per decade (in W) for both IPNFs and NWs.

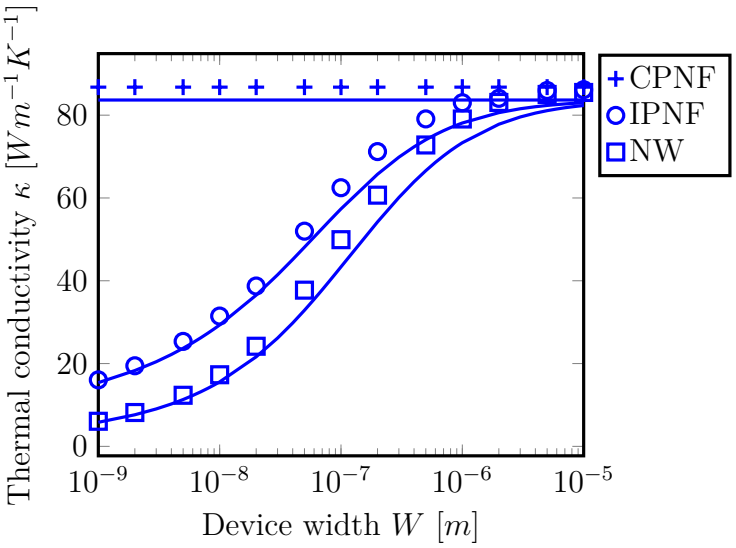

Figure 26: Thermal conductivity as function of device width in Si3C for CPNF +, IPNF ○ and NW □.

5.1.2 Effect of the surface roughness parameter

Figure 27 shows the evolution of κ as a function of the surface roughness empirical parameter Δ for a device of length $L = 1\mu m$ and width $W = 100nm$. Two plateaus can be observed. For ultra-small values of Δ lower than 0.1 nm, the diffusive reflections are negligible and then the cross-plane thermal conductivity using specular interface reflections for phonons is recovered. For a value of Δ higher than 1 nm, the conductivities of NWs and IPNFs reach their minimum. This minimum is related to a fully diffusive regime in which all phonon reflections at the external boundaries are diffusive (with a randomized reflected angle). It should be noticed that the overall trends of these Monte Carlo results are reproduced by the relevant SA models. Nevertheless, these SA models systematically underestimate the MC results.

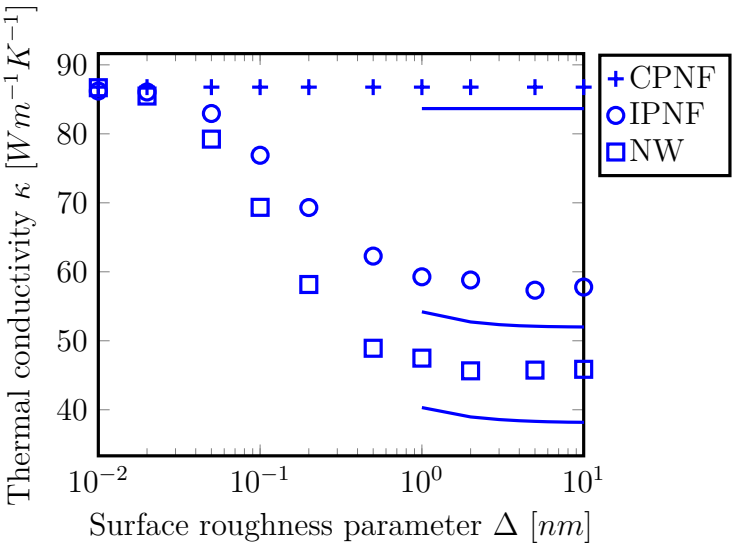

Figure 27: Thermal conductivity as function of the surface roughness parameter in Si3C for CPNF +, IPNF ○ and NW □.

5.1.3 Impact on the spectral and angular distributions of the heat flux

We have performed the same analyses as in §4.2.3 on NWs. The spectral distribution of the thermal energy in a NW follows the equilibrium distribution as shown in Figure 19 for CPNFs.

Figure 28 compares the spectral heat flux in NW and CPNF in Si3C devices with $L = 1\mu m$, $W = 100nm$ and $\Delta = 0.5nm$. The contribution of each mode is plotted with a specific color, solid lines show the results in CPNF while dashed lines stand for NW. We observe a strong reduction of the heat carried via the acoustic modes of the NW with respect to the case of CPNF in accordance with the reduction of the thermal conductance. However, the heat contribution of phonons belonging to the TO mode is higher in NW than in CPNF even if the absolute value remains weak.

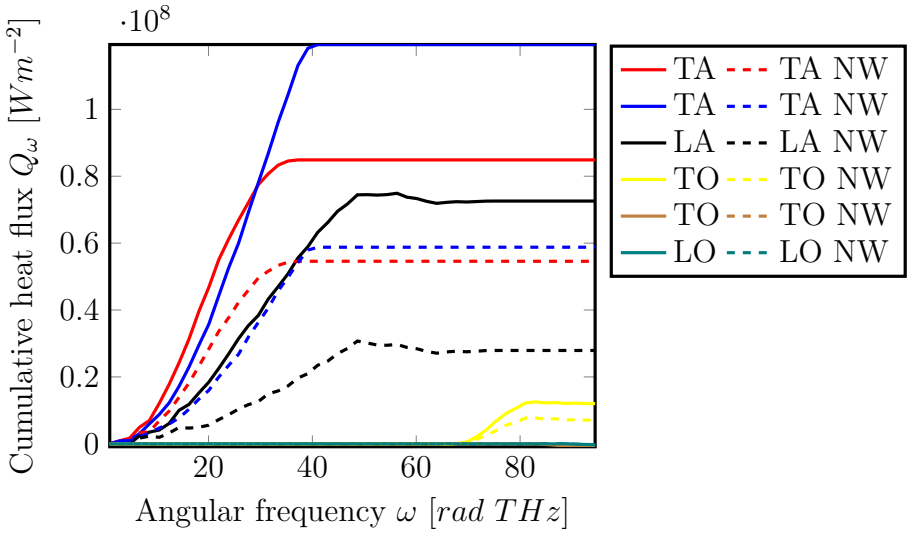

Figure 28: Cumulative spectral distributions of the heat flux in a 1µm long CPNF and NW for each phonon mode.

With respect to the CPNF distribution shown in Table 5 (only differing by the rough boundaries), we observe a heat flux reduction of 49%, 39% and 36% in NW made of Si3C, Si2Hx and Si2Hz, respectively. Indeed, we can explain this difference, as the heat flux in CPNF of Si2H is anisotropic and more intense towards the transport X direction. Besides, the contribution of each mode to the heat flux is indicated in Table 6 (a), (b) and (c) for nanowires made of Si3C, Si2Hx and Si2Hz, respectively. The heat flux reduction ratio is not similar for each phonon mode and depends on the material. In Si3C, the most reduced contribution is related to that of the 2nd and 3rd mode and in Si2Hx the contribution of the 1st, 2nd and 4th ones.

(a)

Mode	Heat flux contribution
1 (TA)	37.0%
2 (TA)	39.9%
3 (LA)	18.9%
4 (TO)	4.8%
5 (TO)	−0.4%
6 (LO)	−0.2%

(b)

Mode	Heat flux contribution
1	18.4%
2	20.7%
3	20.0%
4	15.7%
5	14.5%
6	1.9%
7	2.7%
8	4.6%
9	0.32%
10	0.48%
11	0.40%
12	0.18%

(c)

Mode	Heat flux contribution
1	23.5%
2	24.3%
3	14.3%
4	26.9%
5	17.6%
6	−7.8%
7	3.8%
8	−1.2%
9	0.01%
10	−0.09%
11	−0.53%
12	−0.68%

Table 6: Heat flux contribution per phonon mode in NW with $L = 1$µm and $W = 100$nm, (a) in Si3C, (b) Si2Hx, and (c) in Si2Hz.

The angular distribution of heat flux is plotted in Figure 29 for a CPNF and a NW made of Si2H oriented along the [100] direction with a length $L = 1$µm and width $W = 100$nm. The lateral peaks of the heat flux correspond to directions having an high angular density of states in bulk materials. These states remain important in CPNFs and contribute significantly to the heat flux. However, their impact is strongly reduced in the case of rough NWs where the flux is much more focused along the transport direction [10-10] which is also a main direction of the material.

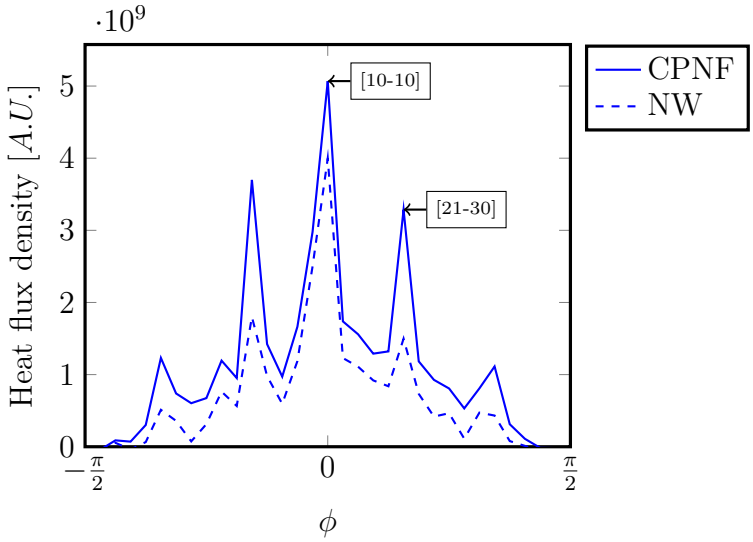

Figure 29: Heat flux angular distribution in Si2Hx NW vs. CPNF, $L = 1\mu m$ and $W = 100nm$.

5.2 Fully diffusive rough boundaries

Previously in this chapter (cf. Figure 27), we have seen that if the phonon boundary scattering mechanism (Soffer's model) is used with a roughness parameter Δ higher than 1 nm, a plateau of the thermal conductivity is reached. This limit is called the fully diffusive limit of the phonon boundary scattering, i.e. for this high value of Δ almost all reflections at the interface are diffusive, i.e. all the reflected angles of reflected phonon are randomized.

In order to mimic such very rough external boundaries, a model called "fully diffusive" (FD) has been implemented. Thus, the FD model is equivalent to the previously used Soffer's model but with a zero probability of having a specular reflection (p_{specular}). To benchmark Soffer's model with $\Delta = 0.5nm$ model and the FD one, the two resulting conductivities in Si3C nanowires are plotted in Figure 30 as a function of the length L (for $W = 100nm$). A significant discrepancy between the two models can be observed only for L higher than 500 nm. This indicates that in the FD, phonons have an average mean free path around 500nm. The FD model is thus relevant in short NWs.

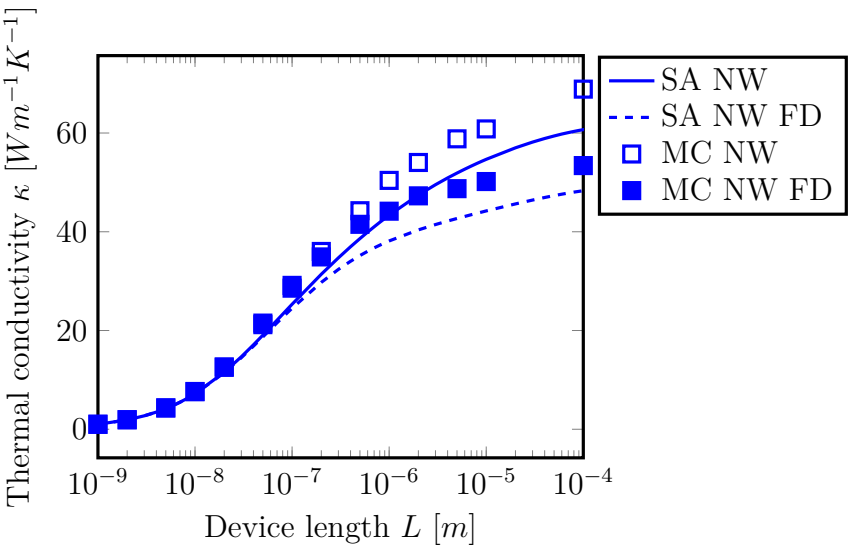

Figure 30: Thermal conductivity as function of device length in Si3C for NW □ and NW FD ■.

5.3 Rough boundaries and crystalline orientations

Our full-band approach for phonon dispersion allows a priori the study of arbitrary crystalline orientations. Nevertheless, only one crystalline orientation has been investigated for Si3C (and two for Si2H) in the previous sections.

Indeed, our implementation of a specular reflection (although it is the standard one) requires the existence of a final state having a wave vector with a negative perpendicular component with respect of the wave vector of the incident phonon ($q_{\perp 0} = -q'_{\perp 0}$). This condition is always fulfilled only if the orientation of the specular boundary is oriented along a high symmetry plane of the crystal.

This limitation is not present in the fully diffusive (FD) model since the final state is randomly chosen among all the available final iso-energy states. We are thus able to study the thermal conductivities of Si3C nanowires for several other crystal orientations. In Figure 31, the thermal conductivity as a function of device length is plotted for [100], [110] and [111] lattice orientations by using the FD model. While the conductivities are similar in all directions for devices smaller than a few µm, at higher lengths different values are achieved, revealing some anisotropy in the heat transport. The diffusive limits along the [111] and [110] directions are 6% and 15% lower than the limit for the [100] direction, respectively.

Once again, the semi-analytical models appear quantitatively disappointing in long devices when the fully diffusive approximation is used, nevertheless they are able to capture the qualitatively the trends of the orientation effects.

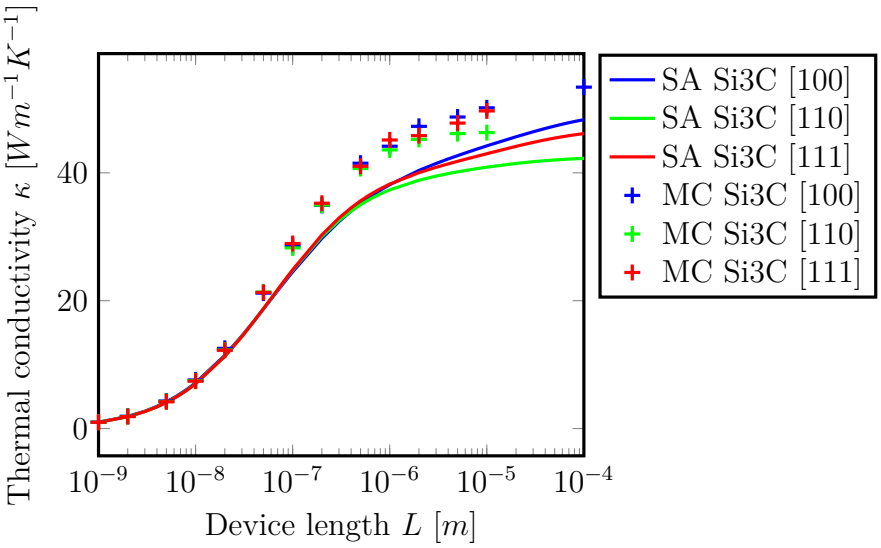

Figure 31: Thermal conductivity κ as function of device length L in Si3C for NW FD in [100], [110] and [111] lattice orientations.

5.4 Comparison with experimental mesurements

Several experimental measurements of thermal conductivity in IPNFs and NWs have been reported in the literature. In this section, we compare works from Ju (Ju and Goodson 1999), Liu (Liu and Asheghi 2006), Li (Li et al. 2003) and Hochbaum (Hochbaum et al. 2008) with results from our Monte Carlo simulations.

In Figure 32 (a) and (b), we compare the calculated and measured conductivities in Si3C IPNF and NW, respectively. In all these experiments, the device length L is about 1 µm. In the case of IPNF, the simulated thermal conductivities fit the experimental data of Liu and Asheghi (2006) and slightly underestimate the conductivity from Ju and Goodson (1999). For nanowires, our results are close to Li et al. (2003) ones and the thermal conductivity relationship with the width are relatively well reproduced, except for the shortest width $W = 22$nm. Hochbaum's results (Hochbaum et al. 2008) show a conductivity that is an order of magnitude lower. They explain this difference by the strong roughness on the NW boundaries due to the fabrication method. However, even our fully diffusive model fails to reproduce these results.

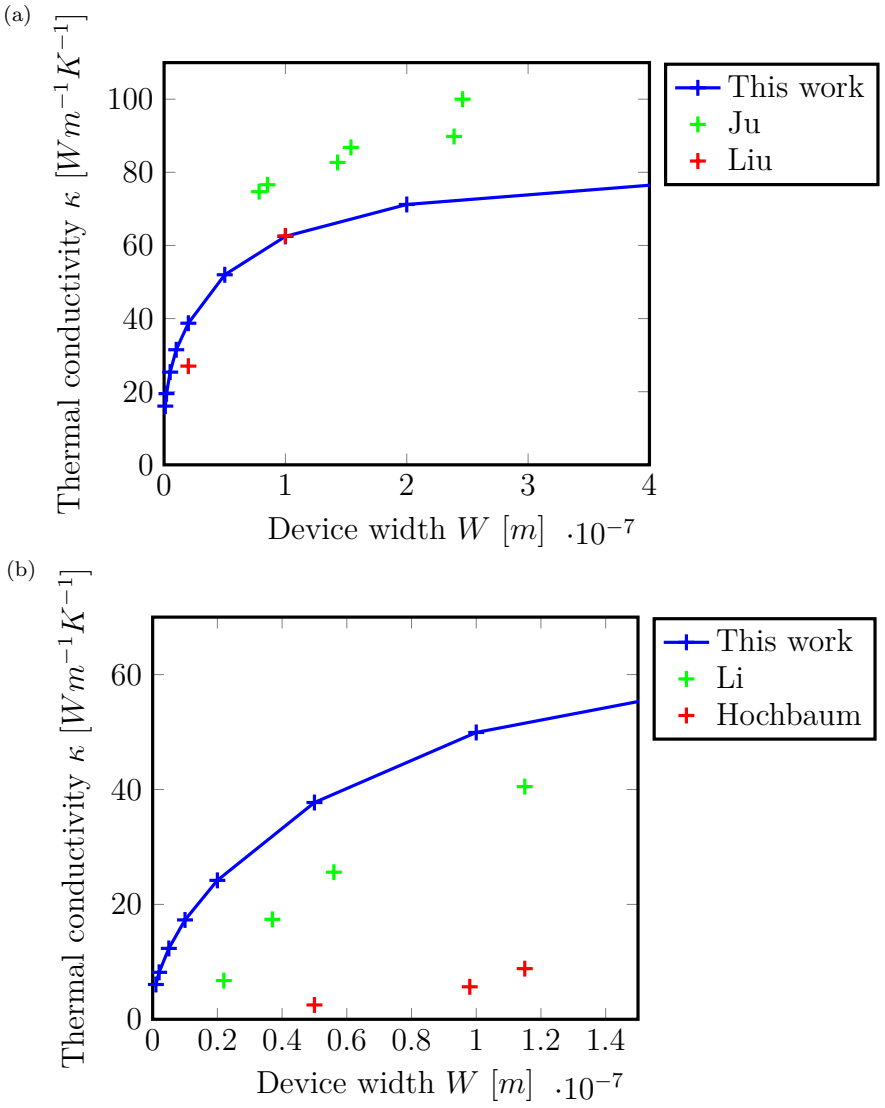

Figure 32: Thermal conductivity in Si3C in (a) IPNF and (b) NW, as function of device width with $L = 1\mu m$. Lines are MC simulations, crosses experimental results from (Liu and Asheghi 2006), (Ju and Goodson 1999), (Li et al. 2003) and (Hochbaum et al. 2008).

In the case of Li's measurements on NW (Li et al. 2003), we further compare the temperature dependence of the thermal conductivity in Figure 33. Only three widths W are considered: 37nm, 56nm and 115nm, as the 22nm device is too small to be correctly simulated using the bulk materials parameters. Our Monte Carlo simulation reproduces correctly the evolution of the conductivity with the temperature. The differences may be due to other sources of thermal resistance in the experimental setup, such as contact resistance.

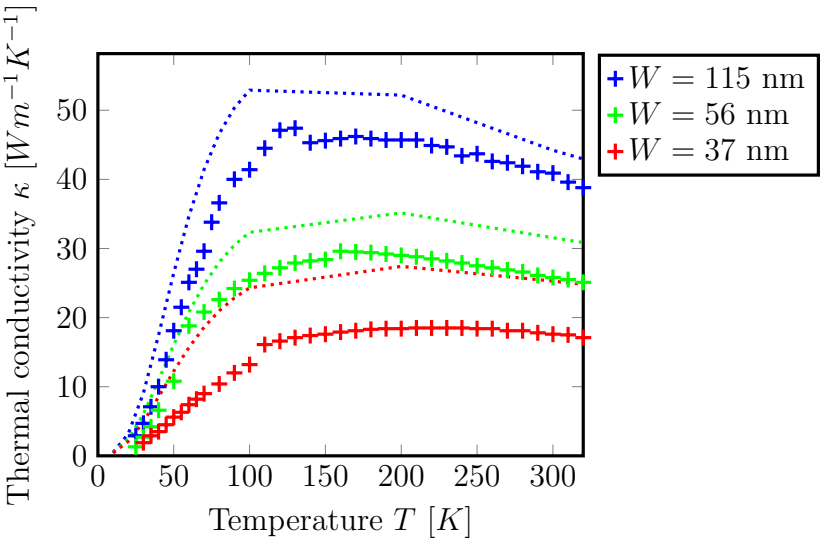

Figure 33: Thermal conductivity in NW as function of temperature, compared with exp. results from (Li et al. 2003).

6 Thermal transport modeling at solid-solid interfaces

This chapter studies the thermal transport at interfaces between semi-conducting materials. One of the goals of this thesis is to characterize the properties of polytype interfaces. Another one is to implement an advanced interface model in a Full-band Monte Carlo simulator (MC) based on data from Molecular Dynamics (MD) simulations, which accurately model the position of atoms at the interfaces.

After presenting the studied interfaces, we determine the simulation parameters in MD to estimate the interface thermal conductance (ITC) at a Si/Ge interface. The implementation of Diffusive Mismatch Model (DMM) to describe the phonon transmission at interfaces in the MC simulator is then tested, and the resulting ITC is compared to the semi-analytical (SA) DMM formula. Using both methods, we investigate the ITC of several interfaces, and their temperature dependence. Finally, we study some spectral properties of the heat flux at the interfaces.

6.1 Simulated interfaces

Several interfaces between Si and Ge in two different phases are considered. As previously, the cubic phases are refered as '3C' and the hexagonal phases '2H'. A lattice orientation of [100] is used when nothing else is specified, '2Hx' and '2Hz' correspond to [10-10] and [0001], respectively.

First the interfaces between cubic Si & Ge in the same lattice orientation are investigated:

- Si3C/Ge3C (stands for Si3C within a [100] orientation in contact with a Ge3C within the same orientation)
- Si3C/Ge3C [110]
- Si3C/Ge3C [111]

Then the polytype interfaces:

- Si3C/Si2Hx
- Si3C/Si2Hz
- Ge3C/Ge2Hx, refered as "aligned" polytype interfaces (see Figure 34 (a))
- Ge3C [00-1]/Ge2H [0-110], refered as "mismatched" polytype interfaces (see Figure 34 (b))

In the case of DMM, pseudo-interfaces between identical materials are also investigated:

- Si3C/Si3C
- Si3C/Si3C [110]
- Si3C/Si3C [111]

The mismatched polytype Ge interface is the kind of interfaces mainly observed in the Ge polytype nanowires fabricated by Vincent et al. (2014).

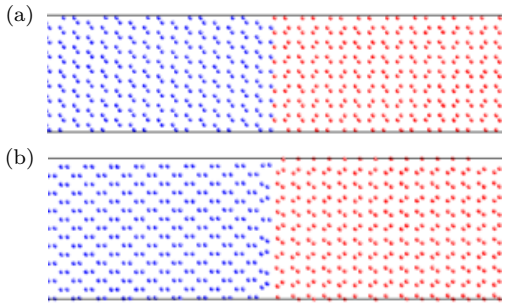

Figure 34: Diagram showing the position of atoms forming the (a) "aligned" and (b) "mismatched" Ge polytype interfaces. Blue and red dots are from the cubic and hexagonal phases respectively.

6.2 Selection of MD simulation parameters

The accuracy of ITC computation by using MD methods relies on a good selection of the relevant simulation parameters. The following MD simulations uses the Stillinger-Weber potential. Indeed, the Tersoff potential used for studying bulk materials (see §4), could not easily be implement by using the spectral analysis that we have choosen (cf. §6.3, the method distinguishes the contribution of atoms at the interface that is not directly consistent with the Tersoff approach). All simulations only consider the steady state.

6.2.1 EMD parameters

The EMD method is reminded in §3.2.3. The main simulation parameters for EMD and their default values are:

- 10 independent runs,
- a simulated time of 0.5 ns,
- a data collection time (1,000,000 timesteps of 0.5 fs) of 0.5 ns,
- a simulated box width W of 8 unit cells,
- a simulated box length L of 32 unit cells of material on each side of the interface,
- an equilibrium temperature T of 400 K.

In Figure 35, it is presented the ITC values for several deviations of the previous simulation parameters from their default value.

In Figure 35 (a), the ITC is calculated by averaging over an increasing number of independent runs. The values reach a plateau after 5 runs.

In Figure 35 (b), an increasing total simulation time is used for averaging each independent run. At least 400,000 timesteps are required in this case.

In Figure 35 (c), the influence of the width of the simulation box is investigated. A sudden drop of the ITC is observed in boxes smaller than 6 unit cells. In such devices smaller than the wavelength of some important phonons, the heat transfer cannot be simulated correctly.

In Figure 35 (d), the influence of the length L of the two materials on each side of the interface is investigated. From 2 to 8 unit cells, the ITC is inversely propotionnal to the length. This dependence is due to the periodicity of the superlattice, and is related to a significant ballistic transport between the interfaces. The ITC is almost constant for L higher than 10 cells.

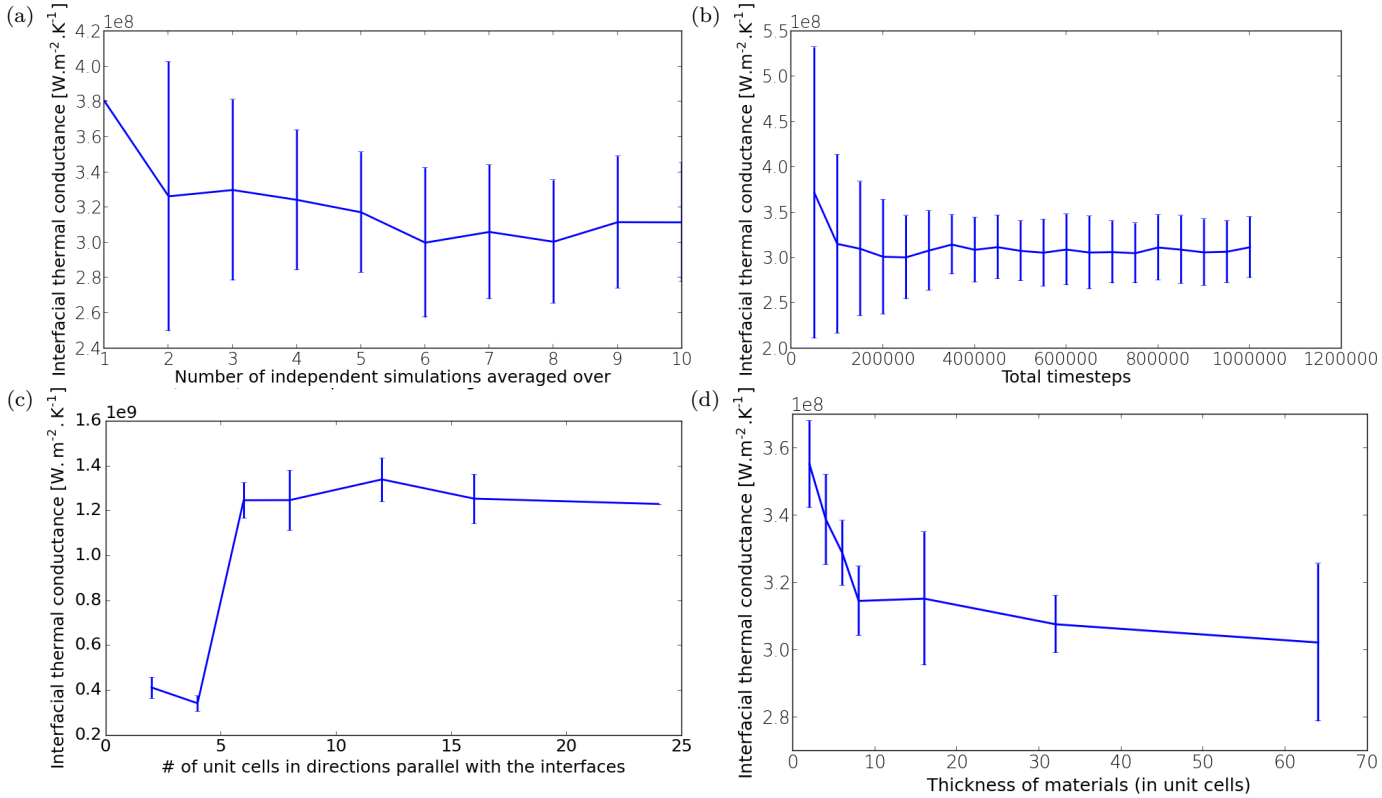

Figure 35: By using EMD, ITC at the Si3C/Ge3C interface vs. (a) number of independent runs, (b) simulated time, (c) width W, and (d) length L.

6.2.2 NEMD parameters

The NEMD method is described in §3.2.5. Our average temperature are higher in NEMD (T=1000K) than in the EMD (T=400K) in order to reduce the mean free path of phonons. This allows to sudy systems with smaller lengths between the thermostats and interfaces leading to lower computational times.

The default simulation parameters chosen for our NEMD simulations are:

- a relaxation time of 0.5 ns,
- a thermalization time with thermostats of 5 ns,
- a data collection (500,000 timesteps of 0.5fs) time of 1 ns,
- a simulated system width W of 4 unit cells,
- a simulated system length of 32 unit cells,
- an average temperature of 1000K,

- a temperature bias ΔT of 100K between thermostats.

The related temperature profile between thermostats is plotted for T=1000 K and ΔT = (a) 10K, (b) 50K and (c) 100K in Figure 36. For ΔT = 10K, we see that the temperature fluctuations are so strong with respect to the temperature gradient at the interface, that it leads to unphysical results. Temperature biases higher than 50 K are required in this structure. The ITC is extracted by using the temperature regression shown in red lines to compute the effective temperature bias at the interface.

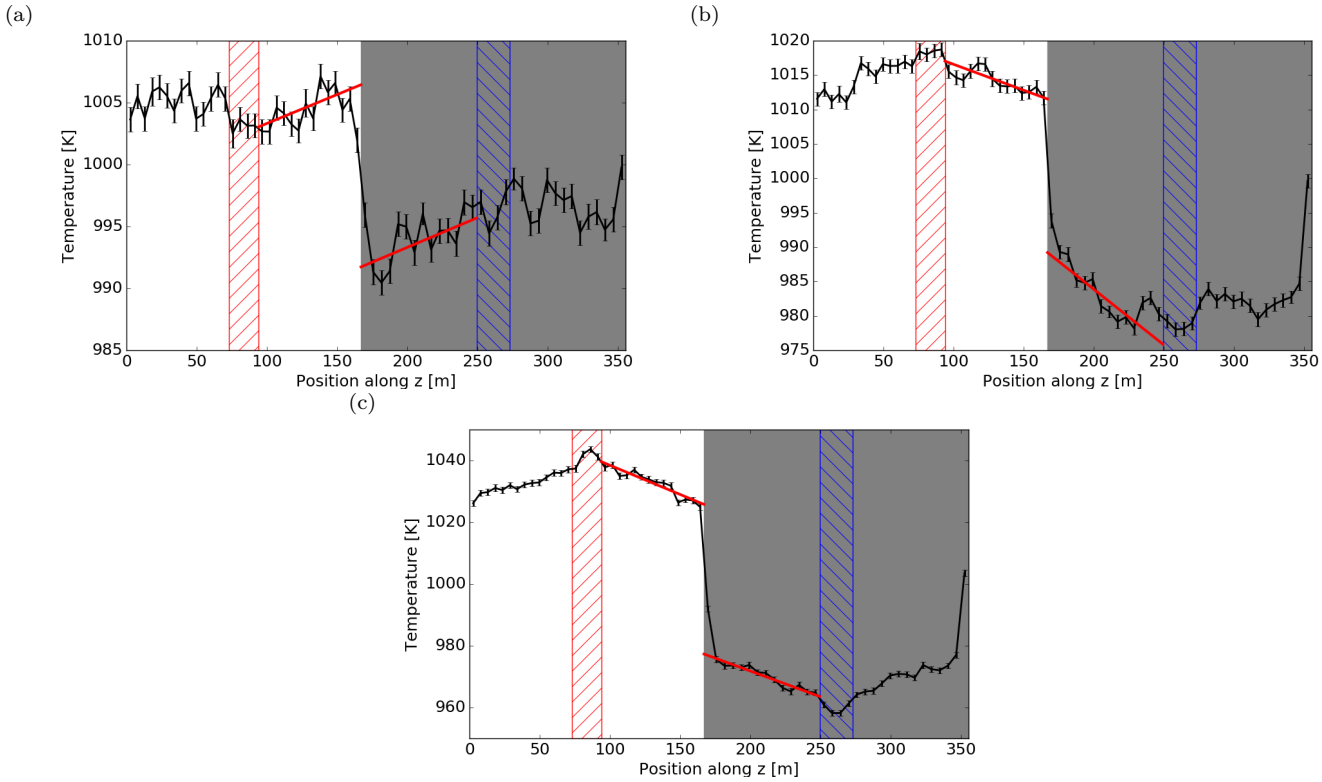

Figure 36: Temperature profiles in the Si3C/Ge3C superlattices along the direction normal to the interfaces, at three imposed temperature differences ΔT: (a) 10K, (b) 50K and (c) 100K. White and grey backgrounds represent Si and Ge, respectively. Hashed areas represent the thermostats. Red bold lines are linear interpolations used to extrapolate the temperature at the interfaces.

The ITC for several values of the simulation parameters in NEMD are presented in Figure 37.

In Figure 37 (a), we see the evolution of ITC with the temperature difference between the thermostats. The results reach a plateau above 100K.

In Figure 37 (b), we see that a simuation time longer than 0.4ns (800,000 timesteps) is required.

In Figure 37 (c), several box widths W are tested. Contrary to the case of EMD

(cf. Figure 35 (c)), the thermal conductance is higher for small W. For the following NEMD simulations, a width of 4 unit cells is selected (N.B. 8 unit cells for EMD).

In Figure 37 (d), the length L of materials on each side is changed. This is the most important point as it directly impacts the computation time. As the ballistic transport is important in these nanometer scale devices, a strong dependence of length L can be observed. At the diffusive limit a plateau appears. In Landry and McGaughey (2009), the diffusive limit is reached in a structure with 400 unit cells between thermostats at 500K. As their system is not periodic in the transport direction, it would correspond in our case to a structure having 800 unit cells for each material. Due to the limitation of our computational ressources, the longest simulated devices have 512 unit cells. With 512 unit cells at 1000K, the diffusive limit is not reached in our simulations. This is consistent with the previously shown MC results of nanofilms (cf. §4).

In bulk NEMD simulations, the thermal conductivy is extrapolated by using the Mathiessen theoretical model presented in §2. In our NEMD simulation the ITCs are L-dependent. However, as far as we know, no L-depend model have been developped for the ITC. This is an open issue as the NEMD method is used in the next section to estimate the spectral transmission of phonons at interfaces.

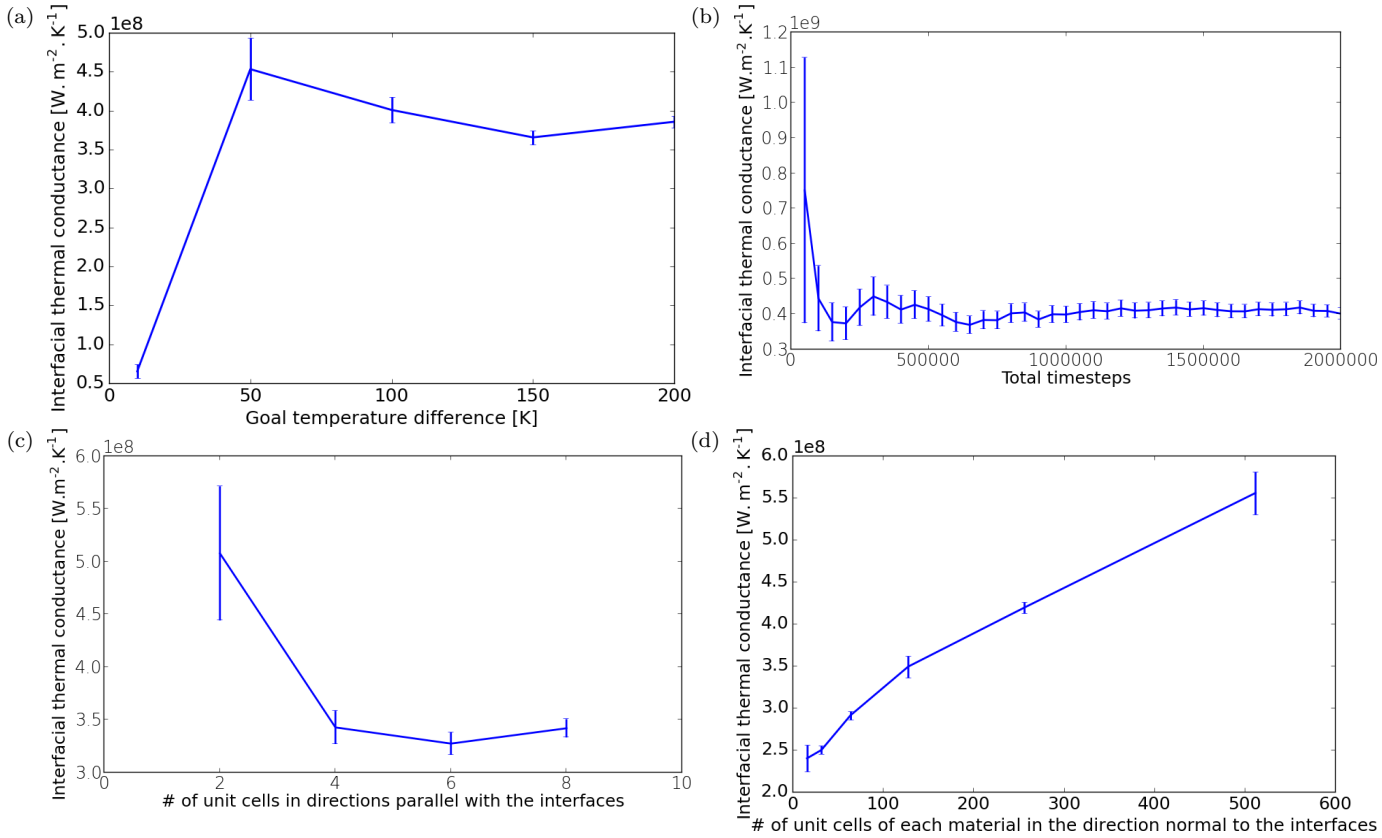

Figure 37: By using NEMD, Si3C/Ge3C ITC vs. (a) temperature bias ΔT, (b) simulated time, (c) width W, and (d) length L.

6.3 Spectral distribution of the interfacial heat flux

This section studies the spectral distribution of the interfacial heat flux computed by using NEMD simulations.

The spectral NEMD heat flux is calculated from the forces and velocities of atoms around the interface. This method is detailed in (Sääskilahti et al. 2014) in the case of an interface between simple materials (i.e. between Argon and an artificially heavy Argon). It is applied here to interfaces between Si and Ge.

The spectral interfacial heat flux $Q(\omega)$ is the sum of the heat fluxes between every pair of atoms i and j across the interface between the materials A and B. The cut-off distance of interatomic potentials limits the number of pairs of atoms included in the calculation.

First, an inter-atomic correlation function K_{ij} is defined as:

$$K_{ij}(t_1 - t_2) = \frac{1}{2} \left\langle \vec{F}_{ij}(t_1) \cdot (\vec{v}_i(t_2) + \vec{v}_j(t_2)) \right\rangle \tag{66}$$

where $\vec{F}_{ij}$ is the force applied from atom j on atom i, and $\vec{v}$ their velocities. The averaging is performed over the simulation time.

The spectral heat flux can then be calculated from its Fourier transform $\tilde{K}_{ij}(\omega)$ by using:

$$Q_{i\to j}(\omega) = \frac{2}{A}\mathrm{Re}[\tilde{K}_{ij}(\omega)] \tag{67}$$

Finally, the spectral conductance can be recovered:

$$G(\omega) = \frac{Q(\omega)}{\Delta T} = \frac{1}{\Delta T}\sum_{i\in A, j\in B} Q_{i\to j}(\omega) \tag{68}$$

Figure 38 shows the resulting normalized spectral heat flux at a Si3C/Ge3C and a mismatched Ge3C/Ge2H interfaces.

These spectral distributions are significantly different. The polytype Ge interfaces have two strong peaks due to the acoustic and optical modes. The heat flux is mainly transmitted via the acoustic modes of phonons. The transmission at the Si3C/Ge3C interface is more uniform. Nevertheless, the second peak is higher and the contribution of optical modes are more important that the acoustic ones.

They both have a similar cutoff in angular frequency around 70 rad.THz. The angular frequency range is limited by the available phonon states in Ge. However, in the case of Si3C/Ge3C, a small spectral heat flux is observed above the cutoff, around 85 rad.THz, which is attributed to anharmonic interactions at the interface.

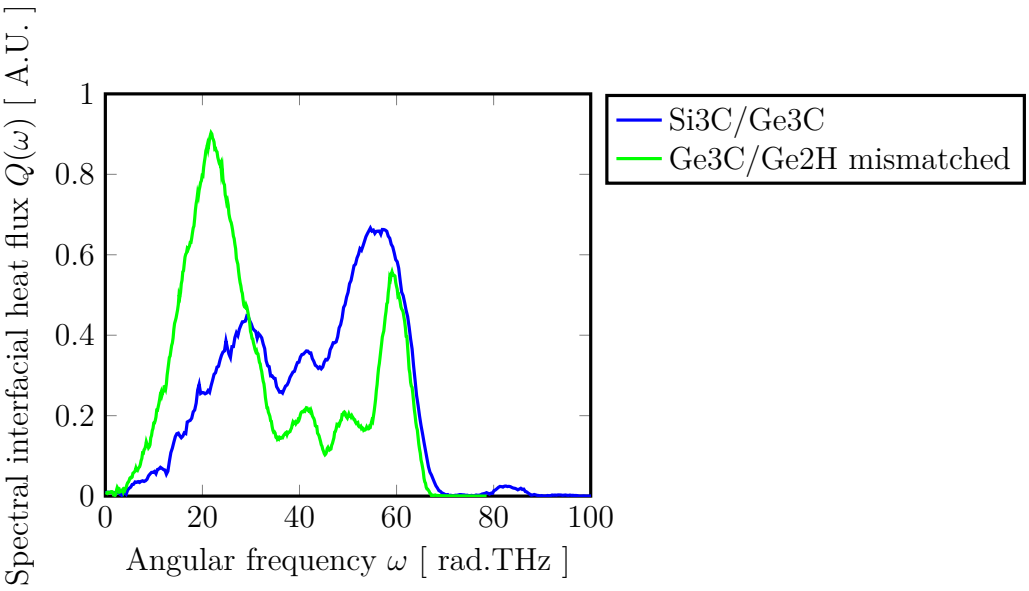

Figure 38: Spectral distributions of the interfacial heat flux at Si3C/Ge3C and Ge3C/Ge2H mismatched interfaces from NEMD simulations.

In MD simulations, a detailed atomic model of the interfaces is implemented. The Full Band DMM model (which is used in MC simulations) provides a simpler physical model of the interface. In Figure 39, we compare the interfacial heat flux of Si3C/Ge3C interfaces computed by using these two methods. The DMM result shows three peaks while only two peaks are present in MD. The DMM spectral flux is higher at lower frequencies. Besides, the DMM cutoff frequency slightly different than in MD as the phonon dispersion relation in MD is not exactly the same. As expected, there is no contribution above the cutoff within the DMM method.

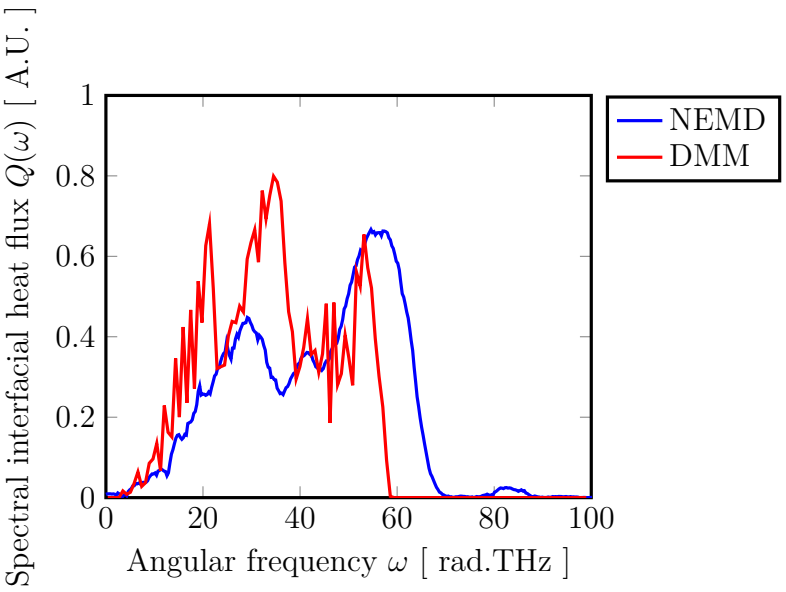

Figure 39: Spectral distributions of the interfacial heat flux at Si3C/Ge3C interfaces from NEMD simulations and DMM.

Figure 40 shows the the DMM spectral transmission coefficients in a Si3C/Ge3C interface, and a polytype Si3C/Si2Hx interface. As in the previous figure, the frequency cutoff is around 60 rad.THz for Si3C/Ge3C, while the polytype Si interface cutoff is around 95 rad.THz. Since the transmission coefficients are calculated by using the DMM impedance of materials, all the simulated polytype interfaces have their transmission coefficients oscillating around $t = \frac{1}{2}$. For Si3C/Ge3C, it is notable that the first and third peaks in the spectral heat flux correspond to high transmission values, while the middle peak is only related to a low transmission $t = 0.2$.

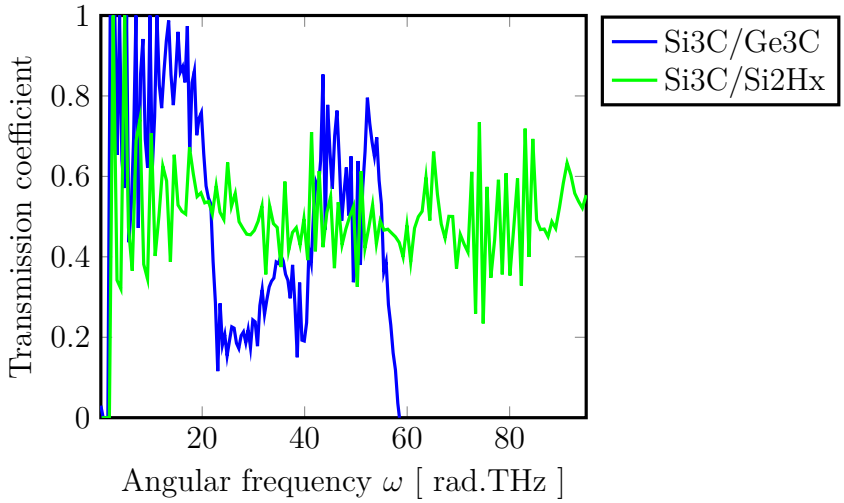

Figure 40: Spectral transmission coefficients at Si3C/Ge3C and polytype Si3C/Si2Hx interfaces from DMM.

6.4 ITC by using MC simulations

To study heterojunctions and superlattices by using Full Band Monte Carlo simulation of phonons, the interface transmission is derived from DMM as explained in §3.1.8.2. This DMM spectral transmission is used to validate our implementation of the heterostructure transmission.

The first test is performed with a Si3C/Si3C interface i.e. a constant transmission of $t_{A\to B} = t_{B\to A} = \frac{1}{2}$, and a Si3C/Si2Hx interface. An heterojunction without any thermostat (i.e. without any phonon injection) is simulated with different initial temperatures on each side of the interface. As expected, after a transient regime, the temperature profile relaxes to the same equilibrium value, and the net heat flux at the interface becomes null.

Then thermostats are added to recover the same configuration as those used in the two previous chapters, i.e. with a hot thermostat and a cold thermostat along the X axis. The temperature profile at steady-state for a Si3C/Si3C heterojunction (HJ) is shown in Figure 41. The red and blue diamonds show the temperature of the thermostats, and the grey vertical line represents the position of the interface.

For small devices, i.e. $L = 100$nm, the transport is in the intermediate transport regime between ballistic and diffusive ones. As expected, we observe a temperature drop at the contacts with the thermostats, and also at the inner interface.

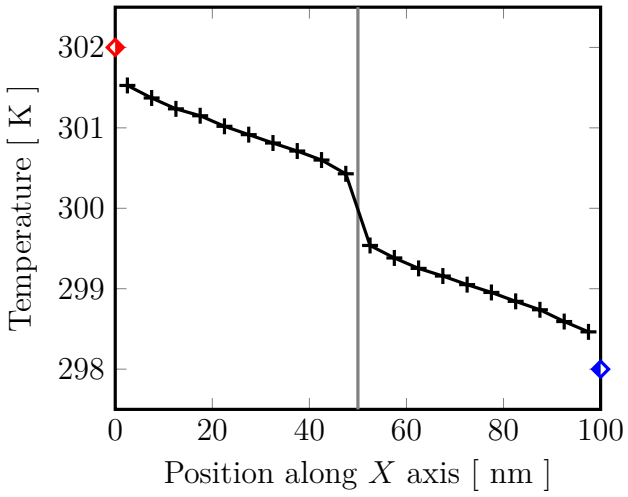

Figure 41: Temperature profile in a Si3C/Si3C HJ, with a DMM interface at $x = 50$nm.

The ITC is calculated as a first attempt by simply dividing the average heat flux in the device and the temperature difference between the two sides of the interface.

In Figure 42, the ITC is calculated in heterojunctions of different lengths L by the mentioned approach. The ITC is expected to be independent of L. This occurs in the ballistic regime but the ITC seems to be around twice the values by using the SA formula. Besides, when L increases, the ITC decreases below the expected value.

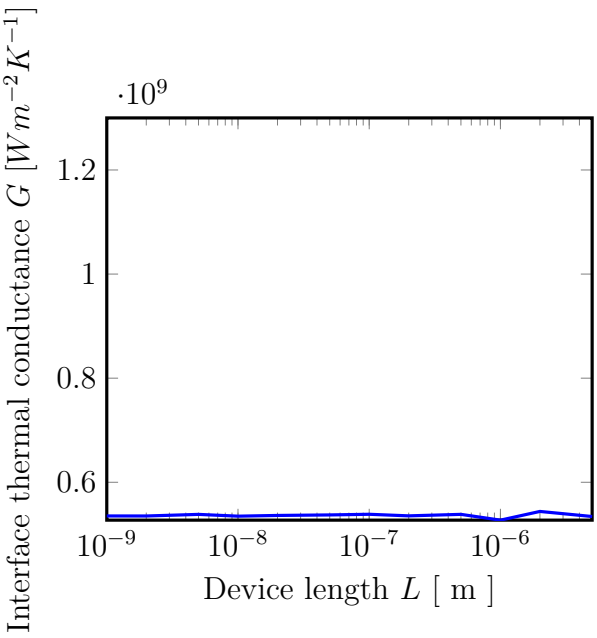

Figure 42: Evolution of the ITC calculated by using irrelevant temperature drops with the device length L.

To recover the expected result, the temperature difference to consider must be different. Only the population of incident phonons on the interface must be included in the computation of the temperature. Indeed, when a strong out-of-equilibirum transport regime occurs, this last approach gives a significantly different temperature drop.

In order to calculate a correct ITC, we simulate very small HJ ($L = 1$nm) without any phonon-phonon scattering mechanism. The incident heat flux on each face is directly the heat flux injected from thermostats in which temperatures are known. The thermostat temperature can thus be used to calculate the temperature drop at the interface ΔT.

The results are given in Table 7 for several interfaces at 300K, and compared to results from the SA formula. They are mostly equivalent for all studied interfaces and orientations except for Si3C/Ge3C interfaces where differences up to 10% are present.

For some interfaces (marked wiht '*'), the specular boundaries on the Y and Z axes are substituted by fully-diffusive boundaries due to technical limitations.

Materials	SA ITC $G\ Wm^{-2}K^{-1}$	MC ITC $G\ Wm^{-2}K^{-1}$
Si3C/Si3C	536	531
Si3C/Si3C [110]	527	528
Si3C/Si3C [111]	526	524∗
Si3C/Si2Hx	512	515
Si3C/Si2Hz	485	480
Si3C/Ge3C	245	266∗
Si3C/Ge3C [110]	239	241∗
Si3C/Ge3C [111]	249	272∗

Table 7: Comparison of ITC at 300K from DMM SA and ballistic MC for several interfaces.

Besides, increasing ΔT does not modify significantly the computed ITC. As permutting the hot and cold thermostats modifies the ITC by about 1%, no significant rectification of interface is observed.

In order to estimate the ITC in more complex devices, a specific method to directly calculate the temperature of the incident heat flux at the interfaces should be implemented in the future.

The thermal conductivity κ of HJ is computed as in CPNF. The evolution of κ with the device length L is plotted in Figure 43, with crosses. We find that it follows closely the results of SA formula for CPNF thermal conductance (continuous line, see §2.4) by using $\frac{L}{2}$ (which is the actual length of the materials in contact) instead of L.

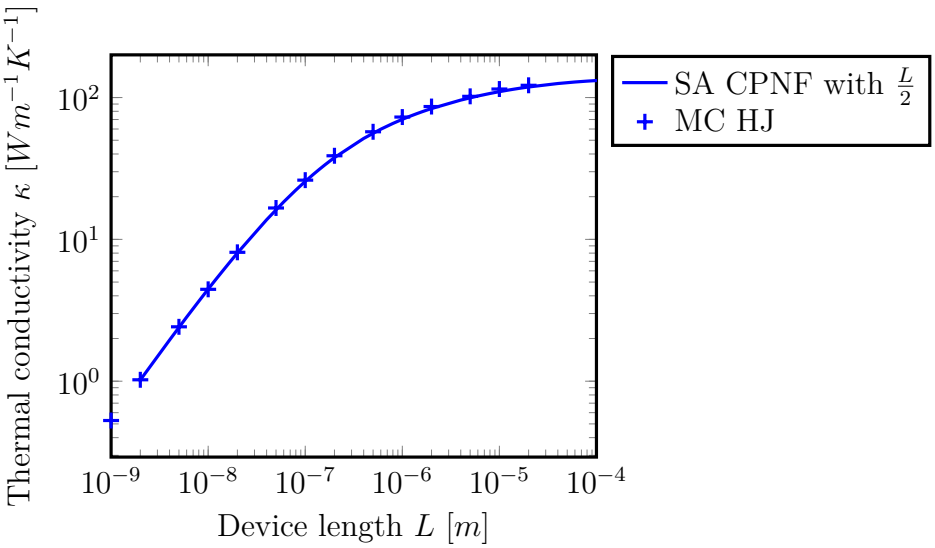

Figure 43: Thermal conductivity in Si3C/Si3C HJ as function of device length.

6.5 Temperature dependence of the interface thermal conductance

We compare in Figure 44 our EMD and NEMD ITC results for several temperatures. The EMD ITC are independant on temperatures. They are on average equal to $G = 650\ MWm^{-2}k^{-1}$, slightly above the results from Chalopin et al. (2012).

However, the NEMD ITC increases when the average temperature increases. This phenomenon was has been previously observed in (Landry and McGaughey 2009). As NEMD results are performed in short devices (in order to reduce simulation times), the computed conductances are low. But as seen in Figure 37 (d) the diffusive limit is higher than our EMD results.

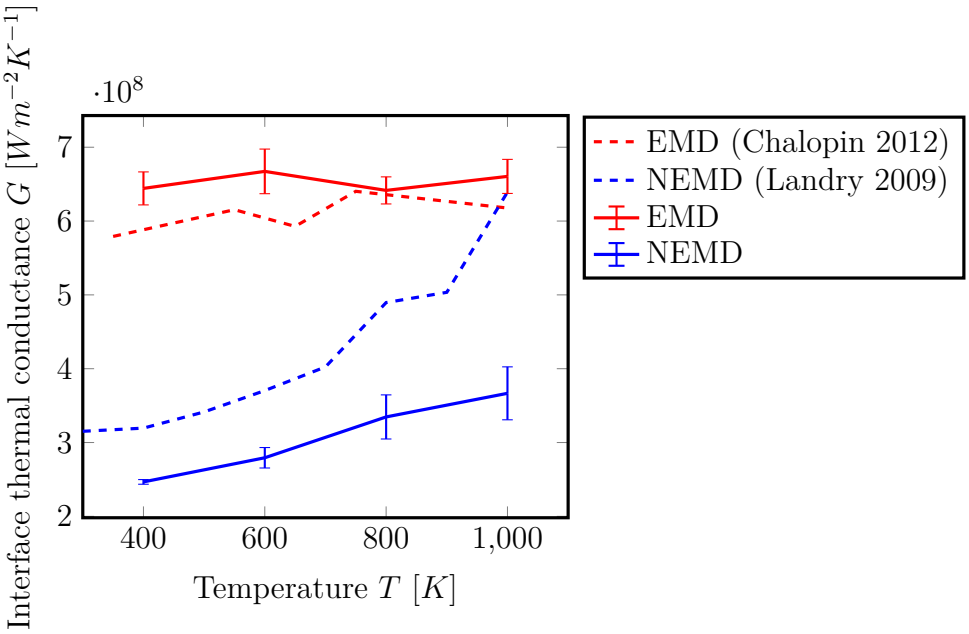

Figure 44: Thermal conductances of Si/Ge strained interfaces as a function of temperature.

After having studied Si/Ge in the [100] lattice orientation, we compare it to the [110] and [111] orientations. In Figure 45, the temperature dependence of these three orientations are calculated by using EMD. In these simulations, the sizes of the simulation box are $8 \times 8 \times (32 + 32)$, $8 \times 6 \times (22 + 22)$ and $6 \times 6 \times (18 + 18)$ unit cells.

There is almost a 50% increase of ITC between the [100] and [110] orientations. Only [111] ITC is temperature dependent.

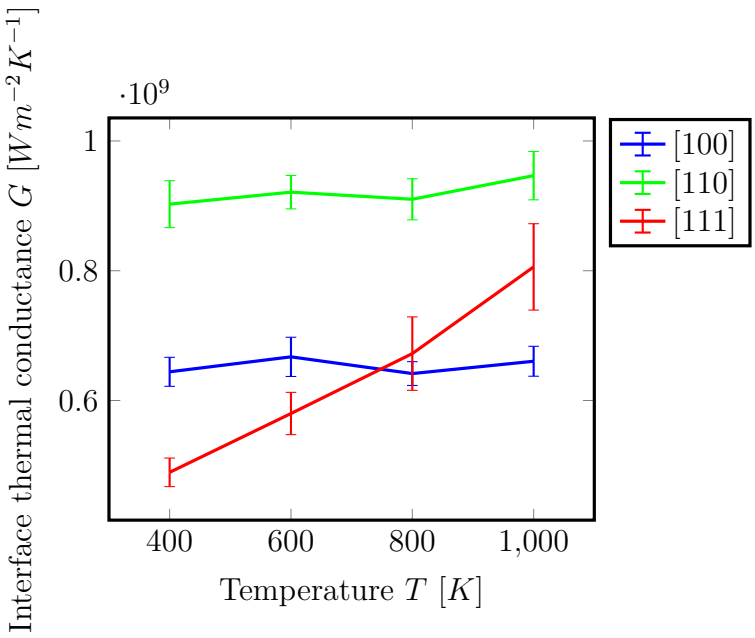

Figure 45: Interface thermal conductances of Si/Ge strained interfaces for several lattice orientations at different temperatures using EMD.

In Figure 46, we compare the conductances of the two Ge polytype interfaces to the Si/Ge [100] one, computed by using EMD. We find that the mismatched polytype ITC is on the same order of magnitude as Si/Ge interfaces, about 50% higher. When stacked in the polytype nanowires, this low ITC value should lead to low a thermal conductivity of the device that could be interesting for thermoelectric applications. The aligned polytype Ge interface is however about 10 times more conductive.

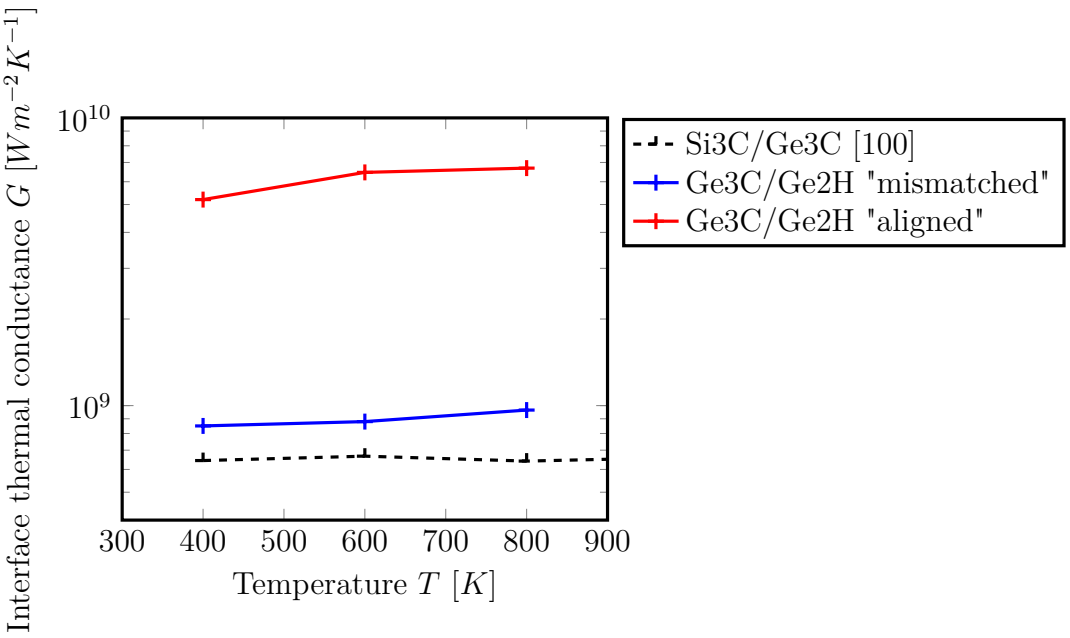

Figure 46: Interface thermal conductance of polytype Ge interfaces and Si/Ge [100] interface as a function of temperature using EMD.

The temperature dependence of the reference Si3C/Ge3C ITC calculated by using the SA DMM formula is shown in Figure 47 for three lattice orientations. These results have been presented in Larroque, Dollfus, and Saint-Martin (2018). As the DMM is a model based on the impedence of the materials, the results are quite different from those of the atomistic MD methods. While the [110] ITC is again higher than the [100] and [111] ones, they all have the same temperature dependence. The ITCs increase when the temperature increases but reach a plateau above 600K.

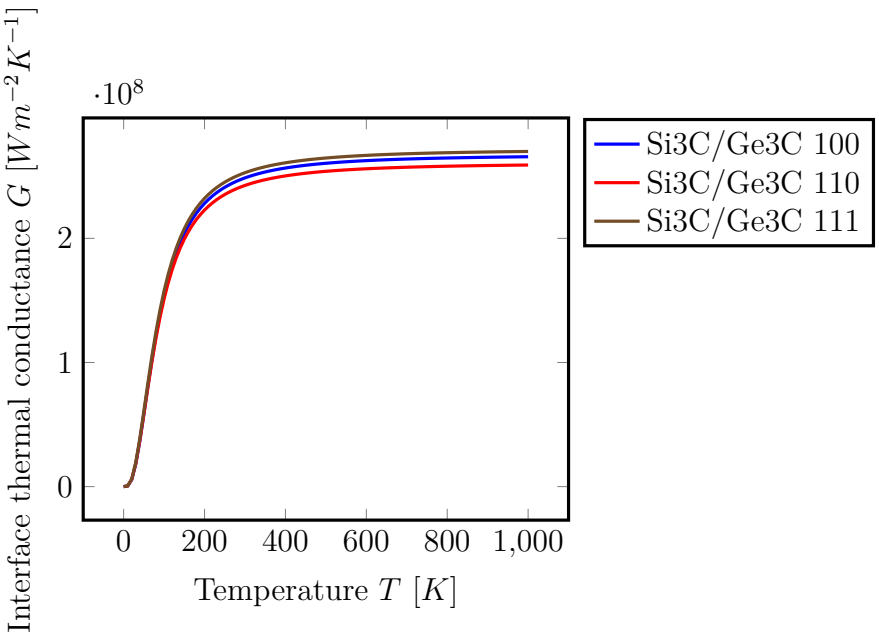

Figure 47: Si/Ge ITC from SA ABCM.

Since the DMM model for the transmission can be seen as a strong approximation, our future work will implement the transmission coefficients computed by using MD in our Full Band MC simulator.

Conclusion

Throughout this thesis, several thermal properties of nanostructures are studied. Two complementary simulation methods are used: Molecular Dynamics, which considers the position of atoms and interatomic potentials, and Monte Carlo simulation for phonons. Previous results on bulk thermal conductivity in Si and Ge are reproduced as well as the thermal conductance of Si/Ge interfaces. An original MC simulator with a full-band model of the material's dispersion relation and scattering rates computed by DFT have been developed during this thesis. As these parameters are based on *ab initio* calculations, this code can be used to study a large class of materials or crystalline phases. Models for rough boundaries and interface between materials are also implemented.

Both methods give insight on the thermal conductivity of the hexagonal phases of Si and Ge. The computed thermal properties of both materials are in agreement with previous theories and measurements. The thermal conductivity is lower for hexagonal phases as compared to the cubic ones.

It has been shown that even if spectral semi-analytical models can estimate satisfactorily the cross plane thermal conductivity in quasi-ballistic transport in nanofilms, they are disappointing when the rough interfaces are dominant as in the case of nanofilms with in-plane configuration or in nanowires. Besides, the contribution of each phonon branch to the heat flux is complex and highly anisotropic. This is also depicted by the polar and azimuthal descriptions of heat fluxes in nanofilms and nanowires. The introduction of rough boundaries impacts mostly acoustic modes (transverse acoustic for Si3C) and tends to focus the heat flux in the main transport direction.

Finally, polytype interfaces can exhibit low thermal conductivities, in the same order of magnitude as Si/Ge interfaces. The Molecular Dynamics methods provide a spectral decomposition of the interfacial heat flux, which is compared to results from the Diffusive Mismatch Model. In future works, more realistic models of interfaces computed by using MD will be implemented in our Monte Carlo simulator. This will allow the complete simulation of polytype nanowires and provide deep insight of the heat transport in these nanodevices.

Acknowledgements

This work is supported by a public grant overseen by the French National Research Agency (ANR) as part of the "Investissements d'Avenir" program (Labex NanoSaclay, reference: ANR-10-LABX-0035).

A Synthèse en français

A.1 Introduction

La conversion thermoélectrique est un sujet de recherche très actif. Ses principales applications sont liées à la récupération d'énergie pour les systèmes d'alimentation électrique autonomes ainsi qu'au refroidissement des microcontrôleurs. Actuellement, les systèmes thermoélectriques courants reposent sur des composés rares et toxiques comme le Tellurure de Bismuth, le Tellurure de Plomb, etc. Leur remplacement par le Silicium et le Germanium, plus abondants et largement utilisés par l'industrie microélectronique, serait intéressant. Cependant, leurs propriétés thermoélectriques intrinsèques sont médiocres, en particulier près de la température ambiante.

Afin d'améliorer la conversion thermoélectrique des appareils à base de Si et de Ge, les nanotechnologies offrent de nouvelles voies d'optimisation. En effet, la nanostructuration permet d'améliorer les propriétés intrinsèques des nanostructures de plusieurs ordres de grandeur.

Dans ce cadre, cette thèse étudie les propriétés thermiques des nanofils polyphasés en Si et Ge récemment fabriqués. Ils sont constitués d'un empilement quasi périodique de phases cubiques et hexagonales de Si ou Ge. La présence de nombreuses interfaces polyphasées devrait être bénéfique pour les propriétés thermoélectriques. Les caractérisations expérimentales de ces nanofils étant encore très difficiles, le développement en parallèle d'outils numériques spécifiques est d'une grande importance pour le développement de cette technologie.

Au cours de cette thèse, un simulateur de Monte Carlo original dédié au transport des phonons a été développé. Il s'agit d'un simulateur "full band" et 3D dans l'espace réel capable de fournir des informations détaillées sur le transport thermique dans des nanodispositifs complexes. Comme les paramètres "semi-empiriques" requis sont calculés à l'aide de données *ab initio*, il est possible de modéliser une grande classe de matériaux et de phases, même s'ils n'ont pas été caractérisés expérimentalement. Par ailleurs, des études réalisées à l'aide de la Dynamique Moléculaire sont présentées afin de paramétrer la modélisation d'interface semi-transparente dans le code MC.

Les différents modèles théoriques utilisés sont présentés dans le §A.2. Les méthodes de simulation Monte Carlo et de Dynamique Moléculaire sont dans le §A.3. Dans le §A.4, nos méthodes sont validées en étudiant les propriétés de matériaux massifs et de couches fines. Dans le §A.5, l'effet de surfaces rugueuses sur des nanostructures est présenté. Enfin, dans le §A.6, les propriétés d'interfaces entre différentes phases de Si et Ge sont étudiées.

A.2 Modèles théoriques

Dans ce chapitre, nous détaillons les bases théoriques utilisées dans cette thèse. Les deux premières sections présentent les dispositifs étudiés et les différents types de modélisation de matériaux. Les sections suivantes portent sur la modélisation du transfert thermique et présentent des approches semi-analytiques pertinentes.

A.2.1 Dispositifs simulés

Dans cette thèse, différents types de nanostructures sont étudiés : nanofilms, nanofils (NW) et hétérojonctions (HJ). Les nanofilms sont considérés dans des configurations où le flux thermique est perpendiculaire (CPNF) ou transverse (IPNF) aux interfaces. Des faces spéculaires sont introduites pour simuler les dimensions supposées infinies (respectivement 2, 1, 0 et 2 dimensions pour CPNF, IPNF, NW et HJ). Ces dispositifs sont paramétrés par leur longer L (distance entre les thermostats, alignés selon l'axe de transport thermique X) et leur largeur W.

A.2.2 Modèles de matériaux

Pour résoudre l'équation du transport thermique dans un système à l'état solide, il faut connaître au préalable la relation de dispersion et les taux de diffusion.

Le mouvement des phonons dans un matériau est perturbé par plusieurs mécanismes de diffusion, qui peuvent être caractérisés par leur fréquences d'interactions. Habituellement, la principale source de résistance thermique est due aux diffusions phonon-phonon.

Il est possible d'avoir une représentation analytique de la relation de dispersion et des taux de diffusion en utilisant plusieurs approximations. Cependant dans cette thèse, une description complète ("full band") de la zone de Brillouin (BZ) est utilisée, c'est-à-dire que les relations de dispersion et les taux de diffusion sont calculés numériquement pour un grand nombre de vecteurs d'ondes dans le volume complet de la BZ. Deux méthodes ont été utilisées pour calculer ces paramètres: l'ABCM (Larroque 2016) et la DFT (Togo, Chaput, and Tanaka 2015).

La DFT est une méthode *ab initio*, qui est donc pertinente pour étudier des matériaux pas encore (ou peu) caractérisés expérimentalement. Les paramètres que nous avons utilisés ont été calculés par Chaput et al. (2018).

Dans les deux cas, la BZ est discrétisée en N vecteurs d'ondes, avec respectivement $N = 31 \times 31 \times 31 = 29791$ et $N = 31 \times 31 \times 19 = 18259$ pour les phases cubiques et hexagonales. La pulsation, la vitesse de groupe et (avec la DFT) le taux de diffusion phonon-phonon sont calculés pour chaque vecteur d'onde $\vec{q}$ et mode m.

En raison de la nature discrète de notre description de la BZ, la définition des états d'iso-énergie doit être relâchée, entrainant des fluctuations sur la pulsation des phonons. La conservation de la pulsation est limitée par le pas de discrétisation sur la pulsation $\Delta\omega$.

A.2.3 Modèles de faces rugueuses

Dans les nanostructures, il faut tenir compte de la contribution des faces rugueuses sur la résistance thermique. En effet, cette contribution peut devenir plus forte que celle des mécanismes de diffusion phonon-phonon.

Pour cela, le modèle de Soffer considère qu'une particule peut subir lors d'une collision soit une réflexion spéculaire, soit une réflexion diffusive (Soffer 1967). Cela est déterminé par une probabilité de réflexion spéculaire dépendante de l'angle d'incidence du phonon, d'un paramètre de rugosité de surface Δ, et d'un paramètre de corrélation spatiale de la rugosité.

Dans le cas où la corrélation spatiale de la rugosité de surface est négligeable, la probabilité de réflexion spéculaire à une face rugueuse est :

$$p_{\text{specular}} = e^{-(2cos(\theta)\Delta|\vec{q}|)^2} \tag{A1}$$

où $\vec{q}$ est le vecteur d'onde incident, θ l'angle d'incidence, et Δ le paramètre de rugosité.

Ce modèle a permis à Kazan et al. (2010) de reproduire les mesures expérimentales de Hochbaum et al. (2008)

A.2.4 Modèles de transport thermique et conductivité thermique

La conductivité thermique d'un matériau peut être calculée par une formule semi-analytique (SA) à partir de la relation de dispersion et des taux de diffusion "full band" (cf. §A.2.2). Des modèles similaires ont été développés par Mingo et al. (2003) et Aksamija and Knezevic (2010), l'originalité de cette thèse est d'utiliser des taux de dispersion "full band" calculés en DFT.

Le modèle **SA balistique** évalue la conductivité thermique dans des nanofilms (CPNF) infiniment courts, utilisant le formalisme de Landauer.

$$\kappa^{\text{balistique}} = \frac{L\ V_s}{\Delta T}\left(\sum_{\substack{\text{état } j \\ |\vec{v}_j\cdot\vec{n}|>0}} \hbar\omega_j|\vec{v}_j\cdot\vec{n}|f_{\text{BE}}(\omega_j,T_{\text{chaud}}) + \sum_{\substack{\text{état } j \\ |\vec{v}_j\cdot\vec{n}|<0}} \hbar\omega_j|\vec{v}_j\cdot\vec{n}|f_{\text{BE}}(\omega_j,T_{\text{froid}})\right) \tag{A2}$$

Le modèle **SA diffusif** est dérivé de l'équation de transport de Boltzmann, et correspond à la conductivité d'un matériau massif.

$$k^{\text{diffusif}} = V_s \sum_{\text{état } j} \hbar\omega_j|\vec{v}_j\cdot\vec{n}|^2 \frac{1}{\lambda_j}\frac{\partial f_{\text{BE}}}{\partial T}(\omega_j,T_{eq}) \tag{A3}$$

où λ_j est le taux de diffusion phonon-phonon pour l'état j.

Un modèle **SA Matthiessen** est d'abord utilisé pour estimer la conductivité de dispositifs dans un régime transitif entre les limites balistique et diffusive.

$$\frac{1}{\kappa_{\text{Matthiessen}}} = \frac{1}{\kappa_{\text{balistique}}} + \frac{1}{\kappa_{\text{diffusif}}} \tag{A4}$$

Des modèles plus complexes basés sur une décomposition spectrale de la conductivité sont généralement plus fiables. Nous avons défini des modèles spectraux

pour trois dispositifs : **SA CPNF**, **SA IPNF** et **SA NW**, utilisant le modèle de Soffer pour les faces rugueuses (cf. §A.2.3).

Pour ces trois modèles, le taux de diffusion des phonons dans un état j est modifié tels que:

$$\lambda_{\mathrm{CPNF},j} = \lambda_j + \frac{|\vec{v}_j \cdot \vec{n}|}{\bar{L}} \tag{A5}$$

$$\lambda_{\mathrm{IPNF},j} = \lambda_j + \frac{|\vec{v}_j \cdot \vec{n}|}{\bar{L}} + \frac{|\vec{v}_j \cdot \vec{n}_{\perp,1}|}{\bar{W}} \tag{A6}$$

$$\lambda_{\mathrm{NW},j} = \lambda_j + \frac{|\vec{v}_j \cdot \vec{n}|}{\bar{L}} + \frac{|\vec{v}_j \cdot \vec{n}_{\perp,1}|}{\bar{W}} + \frac{|\vec{v}_j \cdot \vec{n}_{\perp,2}|}{\bar{W}} \tag{A7}$$

où $\bar{L} = \frac{L}{2}$ et $\bar{W} = W\left(\frac{1}{1-p_{\text{spéculaire}}} - \frac{1}{2}\right)$.

Leurs conductivités thermiques κ_{CPNF}, κ_{IPNF}, et κ_{NW} sont alors calculées avec la formule diffusive (Eq. A3) en adaptant les taux de diffusions.

A.2.5 Modèles de conductance thermique d'interface

La conductance thermique d'interface (ITC) est liée à la chute de température au bord de l'interface entre deux matériaux, quand un flux thermique est imposé.

Le modèle utilisé dans cette thèse pour définir une interface semi-transparente est une adaptation du Diffusive Mismatch Model (DMM) pour notre modèle de matériaux "full band" (Larroque, Dollfus, and Saint-Martin 2018). La DMM considère une interface de mauvaise qualité, de telle sorte que tous les phonons en collision avec l'interface subissent une diffusion. Les phonons peuvent ensuite être soit transmis, soit réfléchit, selon une probabilité de transmission t.

$$G^{\mathrm{DMM}}(\omega, T) = \frac{\partial f_{\mathrm{BE}}}{\partial T}(\omega, T) I_A(\omega) t_{A\to B}(\omega) \tag{A8}$$

où $G^{\mathrm{DMM}}(\omega, T)$ est la décomposition spectral de l'ITC à la température T, f_{BE} est la distribution d'équilibre de Bose Einstein et I_A est le flux de phonons à l'interface.

A.3 Simulation Monte Carlo et Dynamique Moléculaire

Ce chapitre présente les méthodes de simulations numérique utilisées dans cette thèse pour étudier le transport thermique dans des nanostructures.

D'abord, notre méthode Monte Carlo (MC) originale développée partiellement lors de cette thèse est détaillée, puis les méthodes de Dynamique Moléculaire (MD) sont rappelées.

A.3.1 Méthode Monte Carlo

A.3.1.1 Principes

La méthode de Monte Carlo est une approche stochastique pour résoudre l'équation de transport de Boltzmann (BTE). Dans cette thèse, nous présentons un nouveau simulateur pour le transport de phonons en MC, qui résout la BTE en 3D dans l'espace réel et l'espace réciproque (approche "full band"). La relation de dispersion des phonons et les taux de diffusion phonon-phonon, sont paramétrés dans toute la zone Brillouin en utilisant les calculs de DFT *ab initio* (cf. §A.2.2).

La BTE décrit l'évolution temporelle de la distribution de phonons $f_j(\vec{r}, \vec{q}, t)$ dans l'espace de phase, où j est l'état des phonons, $\vec{r}$ la position dans l'espace réel et $\vec{q}$ leur vecteur d'onde.

$$\frac{\partial f_j}{\partial t} + \vec{v} \cdot \vec{\nabla} f = \left.\frac{\partial f}{\partial t}\right|_{\text{interactions}}, \tag{A9}$$

où $\vec{v}_j$ est la vitesse de groupe ($\vec{v}_j = \vec{\nabla}_{\vec{q}}\, \omega_j$, ω_j est la pulsation) et $\left.\frac{\partial f}{\partial t}\right|_{\text{interactions}}$ est le terme d'interactions (diffusion, collisions, etc.).

Nous résolvons la BTE pour le transport de phonons avec une méthode particulaire Monte Carlo (Péraud and Hadjiconstantinou 2011).

Dans cette approche stochastique, les trajectoires d'un grand nombre de particules semi-classiques sont choisies au hasard. Les trajectoires de chaque particule sont décrites comme une séquence de vols libres (trajectoires linéaires dans l'espace réel sans changement dans l'espace réciproque) et d'événements de diffusion instantanés (pas de changement dans l'espace réel mais avec une modification de l'état dans l'espace réciproque). Le mécanisme de diffusion qui met fin à un vol libre peut être soit une diffusion phonon-phonon, soit une collision avec une face du dispositif. Pour chaque particule, l'état initial, la durée de chaque vol libre, ainsi que le type et l'effet de chaque événement de diffusion sont choisis au hasard en fonction des taux de diffusion appropriés.

A.3.1.2 Techniques d'optimisation

Pour réduire le nombre de particules simulées et donc la puissance de calcul requise, les particules simulées ne sont pas des phonons mais des paquets de phonons. Ces paquets ont un nombre de phonons variable, tels que leur énergie totale E_p est toujours constante. Cela permet de simplifier grandement le traitement des diffusions élastiques et garantit dans tous les cas la conservation d'énergie (Klitsner et al. 1988). Le paramètre E_p définit la précision de la simulation.

Puisque seule la déviation de la distribution de phonons par rapport à la distribution d'équilibre est pertinente pour étudier le transport thermique, seulement celle-ci est simulée. Une température de référence T^0 est définie, proche des températures dans les dispositifs simulés, et la distribution d'équilibre à cette température est soustraite. Cela permet de réduire de manière significative le

nombre de particules à simuler, et de réduire la variance des résultats (Péraud and Hadjiconstantinou 2011).

A.3.1.3 Température effective

La température de chaque section du dispositif simulé est mise à jour périodiquement, puisque les taux de diffusion phonon-phonon dépendent de la température locale. Pour cela, la relation énergie-température est pré-calculée pour chaque matériau. L'énergie totale des particules dans une section est sommée, puis la relation énergie-température est inversée numériquement pour obtenir la température locale.

A.3.1.4 Algorithme

En premier lieu, la distribution initiale de particule est générée dans l'ensemble du dispositif. La simulation entre ensuite dans deux boucles : l'une pour chaque pas de temps, et la deuxième pour chaque particule. À chaque pas de temps, la température locale est mise à jour dans chaque section du dispositif, et de nouvelles particules sont injectées par les thermostats. Ensuite, chaque particule est déplacée pendant son temps de vol libre, qui peut être est interrompu par une interaction phonon-phonon ou une collision avec les bords du dispositif.

En considérant que les interactions sont des processus poissoniens (cf. Jacoboni and Lugli (1989)), au début d'un vol libre, le temps avant la prochaine interraction $t_{\text{interaction}}$ est déterminé aléatoirement :

$$t_{\text{interaction}} = -\frac{\ln(n_{\text{random}})}{\lambda_j(T_c)} \tag{A10}$$

où n_{random} est un nombre aléatoire uniforme dans l'intervalle]0;1] et $\lambda_j(T_c)$ est le taux d'interaction, dans notre cas le taux de diffusion phonon-phonon d'une particule dans l'état j à la température T_c.

Bien que la **diffusion phonon-phonon** soit un processus à trois phonons (les ordres supérieurs étant ignorés), nous la traitons comme un processus à deux phonons (Lacroix, Joulain, and Lemonnier 2005). Ceci simplifie grandement l'algorithme, et comme chaque particule a une énergie fixe, la conservation de l'énergie est exacte. Cette approximation peut être considérée dans le cas où un grand nombre de phonons ont un grand nombre de collisions, où le comportement moyen est alors correct. Quand une particule subit une diffusion phonon-phonon à la fin de son vol libre, son état précédent est perdu (Mazumder and Majumdar 2001) et remplacé par un nouvel état. Cet état est sélectionné aléatoirement selon la distribution d'équilibre, pondérée par le taux de diffusion de chaque état (cf. Lacroix, Joulain, and Lemonnier (2005)).

$$p_j \propto \lambda_j(T_c) n_j^{eq}(T_c) \tag{A11}$$

Les **thermostats** injectent un flux de particule constant, dépendant de leur température.

Aux **faces lisses**, les particules subissent une réflexion spéculaire : la composante normale à la face du vecteur d'onde est inversée.

Lors d'une collision avec une **face rugueuse**, la particule a une probabilité de subir soit une réflexion spéculaire, soit une réflexion diffusive (Soffer 1967). Dans le cas d'une réflexion diffusive, un nouvel état est sélectionné aléatoirement dans l'isoénergie concernée, ayant une vitesse positive selon la normale à la face. La probabilité de sélection de ces états est pondérée par la probabilité de réflexion spéculaire et la composante normale de la vitesse (conformément à la Loi de Lambert) :

$$p_{\text{diffusive},j'} \propto (1 - p_{\text{specular},j'})|\vec{v}_{j'}|cos(\theta_{j'}) \tag{A12}$$

Lors d'une collision avec une **face semi-transparente**, la particule a une probabilité de subir soit une transmission diffusive, soit une réflexion diffusive, selon une probabilité de transmission $t_{A\to B}$ calculée par DMM. L'implémentation est similaire aux faces rugueuses, le nouvel état après diffusion étant sélectionné dans l'isoénergie concernée, et ayant une orientation de vitesse cohérente. De la même manière, la probabilité de sélection de ces états est pondérée par la probabilité de réflexion et la composante normale de la vitesse :

$$p_{\text{DMM},j'} \propto (1 - t_{A\to B}(\omega_{j'}))\,|\vec{v}_{j'}|cos(\theta_{j'}) \tag{A13}$$

A.3.2 Dynamique Moléculaire

Les méthodes de Dynamique Moléculaire (MD) sont des simulations classiques des trajectoires d'atomes. Comme chaque position atomique est déterminée lors de l'initialisation, il est possible de modéliser avec précision les interfaces entre matériaux par ces techniques.

Dans une simulation MD, chaque atome a une masse, une position et une vitesse définies. La deuxième équation de Newton dépendante du temps est résolue numériquement pour obtenir les trajectoires atomiques. Les forces instantanées des interactions entre atomes sont calculées à partir de potentiels semi-empiriques. Enfin, toutes les propriétés thermodynamiques pertinentes peuvent être obtenues à partir d'une analyse statistique du système.

Ces techniques sont assez polyvalentes mais ont leurs limites. Tout d'abord, ces méthodes exigent beaucoup de puissance de calcul, donc seuls de petits systèmes de quelques milliers d'atomes sont gérables. Afin d'éviter de diffuser les phonons aux limites, des conditions périodiques sont généralement appliquées, mais la taille du système par rapport au libre parcours des phonons doit être prise en compte. Enfin, nous devons garder à l'esprit qu'il s'agit d'une simulation classique qui ne peut rendre compte d'effets quantiques. Les simulations MD sont donc limitées à des régimes de températures élevées supérieures à la température de Debye du matériau, qui peut être relativement élevée dans le cas des semi-conducteurs standards.

Des méthodes à l'équilibre (EMD) et hors équilibre (NEMD) ont été utilisées dans les travaux suivants, pour étudier des matériaux massifs et des interfaces.

Les méthodes EMD utilisent un formalisme de Green-Kubo pour déterminer les propriétés thermiques, alors que les méthodes NEMD sont similaires à des mesures expérimentales de dispositifs.

Ces méthodes ont été décrites dans des travaux précédents :

- EMD massif (Sellan et al. 2010; Schelling, Phillpot, and Keblinski 2002; Volz and Chen 2000)
- EMD aux interfaces (Chalopin et al. 2012)
- NEMD massif (Schelling, Phillpot, and Keblinski 2002)
- NEMD aux interfaces (Landry and McGaughey 2009)

A.4 Matériaux massifs et nanofilms

A.4.1 Transition entre régimes balistique et diffusif

Les différents modèles SA ont été comparé dans des dispositifs de différentes longueurs L. Pour les dispositifs très longs, tous les modèles (sauf le modèle balistique) convergent vers la valeur diffusive de conductivité thermique qui correspond à la conductivité du matériau massif. De même, à l'exception du modèle diffusif, ils convergent asymptotiquement vers la conductance du modèle balistique dans les dispositifs courts. Cela confirme que les modèles sont équivalents à ces limites.

En comparant aux résultats de simulation MC, on trouve que la transition entre ces limites n'est pas correctement exprimée par le modèle Matthiessen (jusqu'à 60% de différences observées). Cependant, le modèle SA CPNF est très proche des résultats MC sur toute la gamme de longueurs. Cela indique qu'un traitement spectral de la conductivité est nécessaire pour représenter de manière précise la transition entre ces régimes.

A.4.2 Phases hexagonales de Si et Ge

Dans la Table A1, la conductivité thermique des phases cubiques et hexagonales de Si et Ge à $T = 1000$K sont calculées par EMD. Dans les deux cas, les phases hexagonales ont des conductivités inférieures aux phases cubiques correspondantes.

	Si	Ge
Cubique	77.2 ± 21.3	32.4 ± 7.2
Hexagonale	72.0 ± 16.8	31.6 ± 11.2

Table A1: Conductivité thermique à 1000K par EMD, pour des phases cubiques et hexagonales de Si et Ge.

Ces matériaux sont ensuite étudiés avec des simulations MC et le modèle SA CPNF. La Figure A1 montre l'évolution de la conductivité avec la longueur du dispositif dans des CPNF en Si cubique (Si3C) et Si hexagonal dans les orientations cristallines [10-10] (Si2Hx) et [0001] (Si2Hz). Les courbes ont les

mêmes caractéristiques, et confirment que la conductivité des phases hexagonales est inférieure à celle de la phase cubique pour toutes les longueurs. À la limite diffusive, $\kappa_{\text{diffusif}} = 138$, 100 et $74 W m^{-1} K^{-1}$ respectivement pour Si3C, Si2Hx et Si2Hz. De plus, on observe une anisotropie entre les deux phases hexagonales, puisque la conductivité diffusive est supérieure de 26% en Si2Hx comparé à Si2Hz.

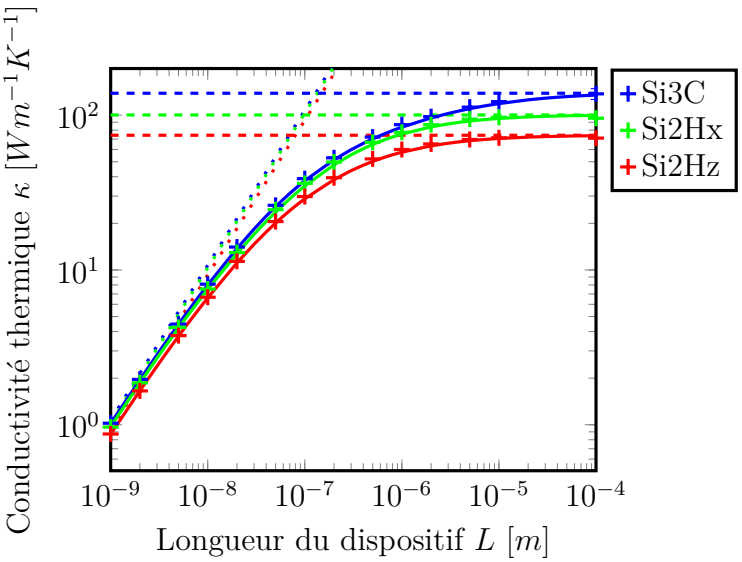

Figure A1: Conductivité thermique de CPNF en fonction de leur longueur L, en Si3C (bleu), Si2Hx (vert) et Si2Hz (rouge).

A.4.3 Distribution spectrale du flux thermique

Dans la Figure A2, l'intégrale sur la pulsation de la distribution spectrale du flux thermique est tracée pour des CPNF de 1µm en Si3C, depuis des simulations MC et le modère SA CPNF. Les contributions de chaque mode sont séparées par couleur. Les résultats des deux modèles sont similaires, mais les contributions totales dans chaque mode diffèrent. De plus, pour certains modes à haute fréquence angulaire, une contribution négative au flux thermique peut être observée dans des résultats MC qui ne sont pas présents dans le modèle SA. Nous expliquons ce phénomène par le fait que l'approximation diffusive utilisée dans le modèle SA CNPF ne tient compte que des vitesses positives, puisque seules leurs valeurs absolues sont utilisées. Ainsi, les flux thermiques totaux calculés par le modèle SA sont plus élevés que ceux calculés en utilisant MC.

(a)

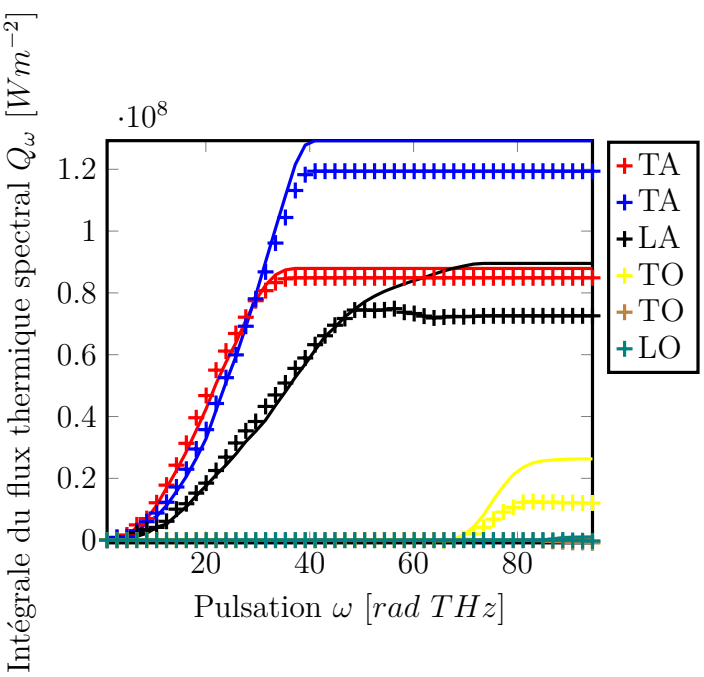

Figure A2: Intégrale de la distribution spectrale du flux thermique pour chaque mode dans un CPNF de 1µm de long, en Si3C, avec le modèle SA CPNF (ligne continue) et des simulations MC (croix).

A.4.4 Distribution angulaire du flux thermique

Notre modèle de matériaux “full band” permet de rendre compte de l’anisotropie du transport thermique. Pour l’estimer, la distribution angulaire de la densité d’état (aDOS) et du flux thermique sont représentée dans la Figure A3, pour un CPNF de 1µm en Si3C, extrait depuis une simulation MC. Nous observons une aDOS élevée dans les principales directions cristallines. Comme prévu, la contribution principale du flux est orientée directement vers la direction du transport. Cependant, le flux thermique le long des directions <111> est plus élevé que le long des directions <110> même si leur aDOS est inférieure. Des phénomènes similaires sont présents en Si2Hx et Si2Hz.

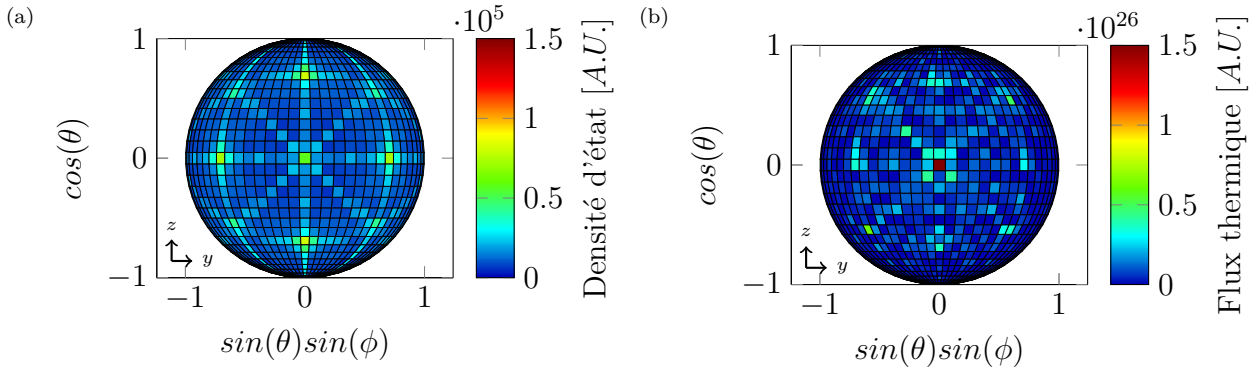

Figure A3: Distributions angulaires (a) de la densité d'état, (b) du flux thermique, dans un NW de 1µm de long en Si3C.

A.5 Nanostructures rugueuses

Ce chapitre considère l'effet des faces rugueuses, introduites dans les nanofilms IPNF, et les nanofils NW.

A.5.1 Effets dus à la géométrie des dispositifs

La dégradation de la conductivité thermique dans des dispositifs longs (donc diffusifs) est liée au nombre de faces rugueuses présentes. Cependant, dans les appareils ultra-courts dans lesquels le transport thermique est balistique, l'évolution des conductivités thermiques sont les mêmes. Dans le cas de IPNF et NW de très grandes largeurs ($W > 1$µm), ou de paramètres de rugosité très faibles ($\Delta < 0.1$nm), la conductivité tend vers la valeur limite des CPNF. Il est notable que contrairement aux CPNF, les modèles semi-analytiques (SA), correspondent pas précisément aux simulations MC pour les IPNF et les NW, bien que les tendances soient les mêmes.

A.5.2 Impact sur les distributions spectrales et angulaires du flux thermique

La Figure A4 (a) compare la distribution spectrale du flux dans un CPNF (ligne continue) et un NW (pointillés) de même dimension ($L = 1$µm et $W = 100$nm), en Si3C, avec un paramètre de rugosité $\Delta = 0.5$nm. On observe que la réduction du flux par les faces rugueuses degrade plus fortement le transport des modes acoustiques. La proportion de flux transporté par les modes optiques est donc plus grande dans les NW que dans les CPNF, bien que toujours très faible.

La Figure A4 (b) compare la distribution angulaire du flux selon l'angle azimutal ϕ dans un CPNF (ligne continue) et un NW (pointillés), en Si2Hx, avec les mêmes paramètres que précédemment. Comme vu dans le chapitre précédent, le flux en CPNF est transporté par les orientations cristallines ayant une grande densité d'état. Cependant, l'introduction de faces rugueuses réduit principalement le

flux dans les orientations hors de la direction du transport (par exemple [21-30]). Il y a donc une concentration du flux thermique.

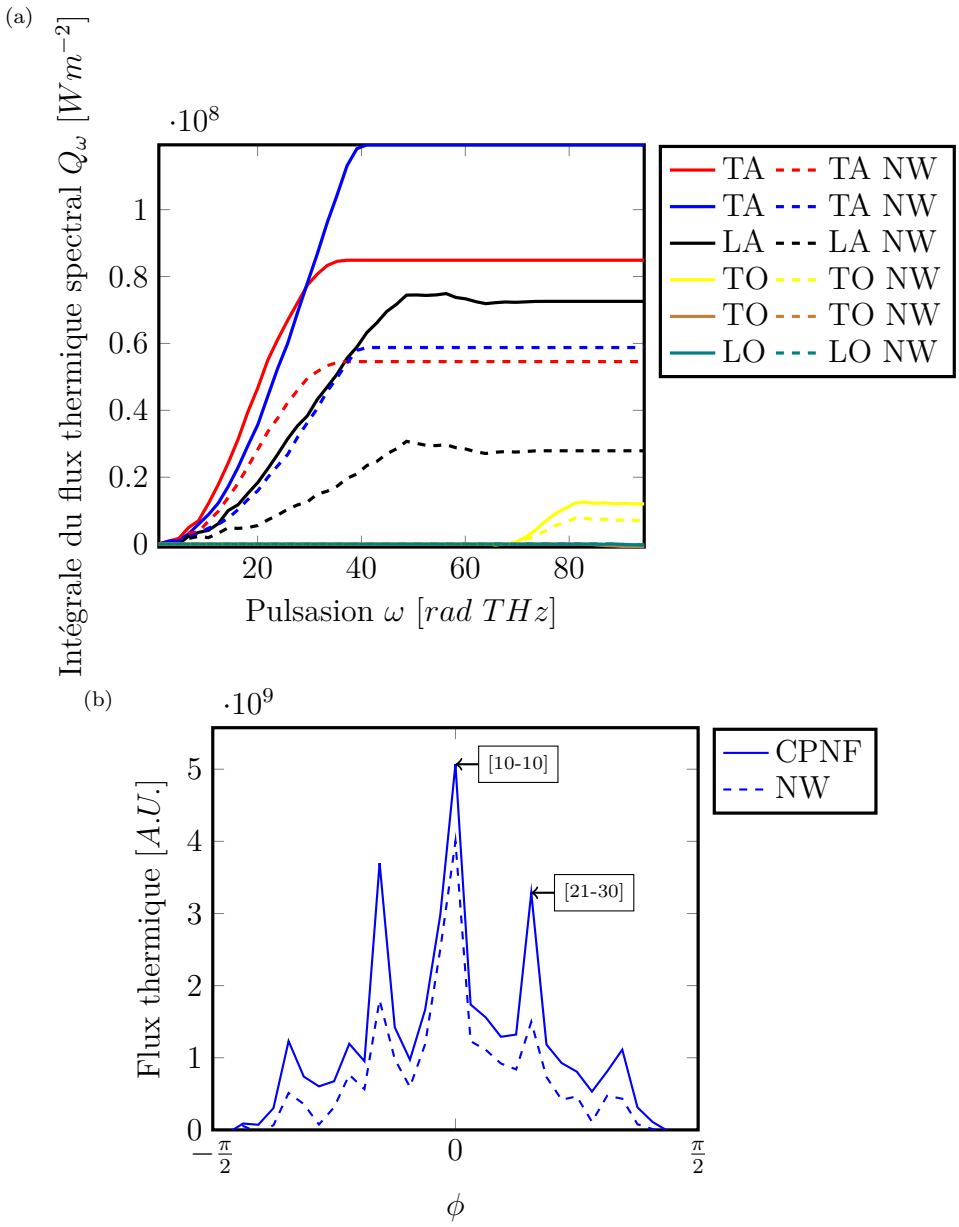

Figure A4: (a) Intégrale de la distribution spectrale du flux thermique pour chaque mode, dans un CPNF (ligne continue) et un NW (pointillés) de 1µm de long, en Si3C, depuis des simulations MC. (b) Distribution angulaire du flux selon l'angle azymuthal ϕ dans un CPNF (ligne continue) et un NW (pointillés), en Si2Hx, depuis des simulations MC

A.5.3 Comparaison avec des mesures expérimentales

Dans le cas des mesures de Li sur NW (Li et al. 2003), nous comparons la dépendance en température de la conductivité thermique sur la figure A5. Seulement trois largeurs W sont considérées : 37nm, 56nm et 115nm, car les dispositifs de 22nm sont trop fins pour être simulés correctement en utilisant les paramètres des matériaux massifs. Notre simulation Monte Carlo reproduit correctement l'évolution de la conductivité avec la température. Les différences peuvent être dues à d'autres sources de résistance thermique dans les mesures expérimentales, comme des résistances de contact.

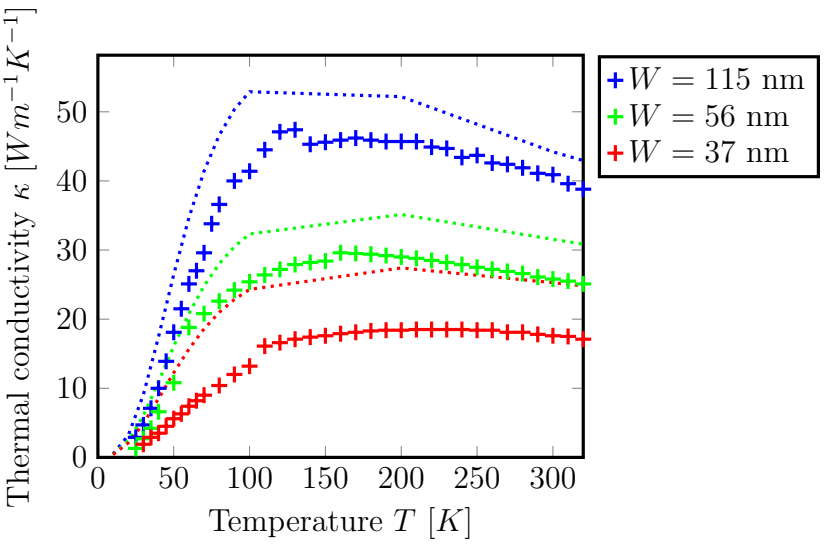

Figure A5: Conductivité thermique de NW en Si3C en fonction de la température, comparés aux mesures expérimentales (Li et al. 2003).

A.6 Transport thermique aux interfaces solide-solide

Ce chapitre étudie le transport thermique aux interfaces entre des matériaux semi-conducteurs.

L'un des objectifs de cette thèse est de caractériser les propriétés des interfaces polyphasées. Un autre consiste à mettre en œuvre un modèle d'interface avancé dans un simulateur de Monte Carlo "full band" basé sur des données issues de simulations de dynamique moléculaire (MD), qui modélisent avec précision la position des atomes aux interfaces.

A.6.1 Distribution spectrale du flux thermique aux interfaces

Le flux thermique spectral est calculé en NEMD à partir des forces et des vitesses des atomes autour de l'interface (Sääskilahti et al. 2014). Dans le cas d'interface

Si3C/Ge3C, il est comparé dans la Figure A6 avec le flux thermique à une interface DMM.

Le flux spectral DMM montre trois pics alors que seulement deux pics sont présents en MD. Il est plus élevé aux basses fréquences en DMM. De plus, la fréquence de coupure en DMM est légèrement différente de celle en MD, car la relation de dispersion des phonons en MD n'est pas exactement la même. En MD, certaines contributions sont observées au-dessus de la fréquence de coupure, dues à des effets anharmoniques.

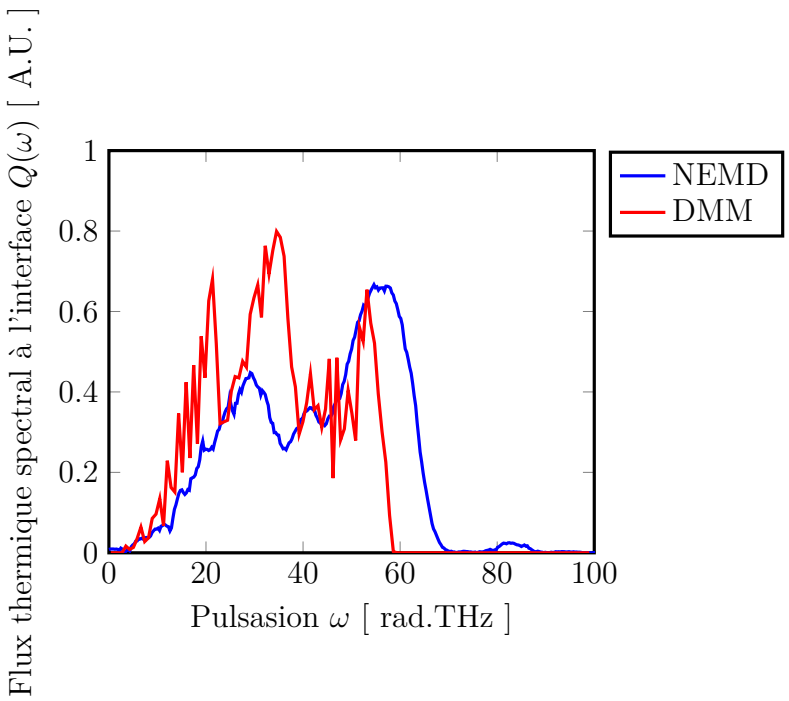

Figure A6: Distribution spectrale du flux thermique à une interface Si3C/Ge3C, par une simulation NEMD et le modèle DMM.

A.6.2 Dépendance à la température de la conductance d'interface

Dans la Figure A7, nous comparons les conductances thermiques d'interface (ITC) de deux interfaces en Ge polyphasées à celle d'une interface Si3C/Ge3C, calculées en EMD. Ces deux interfaces polyphasées correspondent aux orientations cristallines suivantes :

- interface "alignée" Ge3C [100] // Ge2H [10-10],
- interface "non alignée" Ge3C [00-1] // [0-110], correspondant aux interfaces observées dans les nanofils polyphasée de Vincent et al. (2014).

Nous constatons que l'ITC de l'interface polyphasée "non alignée" est du même ordre de grandeur que l'ITC d'interfaces Si/Ge (supérieure d'environ 50%). Dans une nanostructure possédant un grand nombre de cette interface, la faible ITC

devrait réduire significativement la conductivité du dispositif, ce qui le rendrait intéressant pour des applications thermoélectriques. Par contre, l'interface polyphasée "alignée" a une ITC environ 10 fois plus grande.

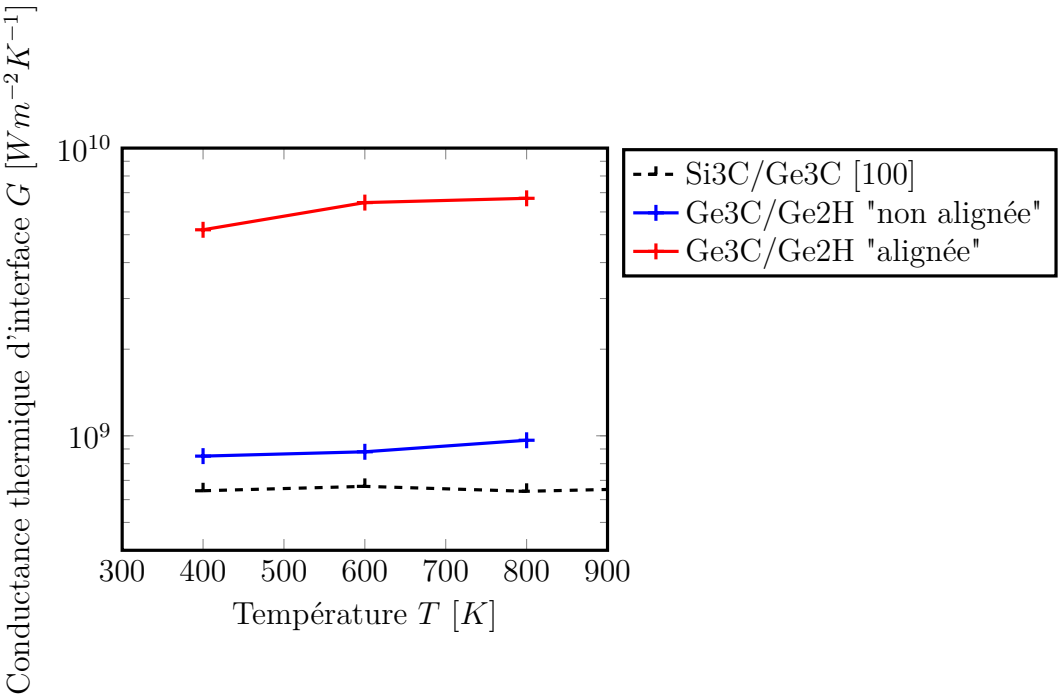

Figure A7: Conductance thermique d'interface Si3C/Ge3C et d'interfaces Ge polyphasées "alignée" et "non alignée", en fonction de la température, en EMD.

A.7 Conclusion

Dans cette thèse, plusieurs propriétés thermiques de nanostructures sont étudiées. Deux méthodes de simulation complémentaires sont utilisées : la Dynamique Moléculaire, qui prend en compte la position des atomes et des potentiels interatomiques, et des simulation Monte Carlo de phonons. Les résultats précédents sur la conductivité thermique en Si et Ge massifs sont reproduits ainsi que la conductivité thermique d'interfaces Si/Ge. Un simulateur Monte Carlo original, utilisant un modèle "full band" de la relation de dispersion et des temps de relaxation calculés par DFT, a été développé au cours de cette thèse. Comme ces paramètres sont basés sur des calculs *ab initio*, ce code peut être utilisé pour étudier une grande classe de matériaux ou de phases cristallines. Des modèles de faces rugueuses et d'interfaces entre matériaux sont également étudiés.

Les deux méthodes de simulation donnent un aperçu de la conductivité thermique des phases hexagonales de Si et Ge. Les propriétés thermiques calculées des deux matériaux sont en accord avec les théories et mesures précédentes. La conductivité thermique est plus faible pour les phases hexagonales que pour les phases cubiques correspondantes.

Nous avons démontré que même si les modèles semi-analytiques spectraux peuvent estimer de manière satisfaisante la conductivité thermique dans le cas de transport quasi-balistique dans des nanofilms, elles sont décevantes lorsque l'effet des faces rugueuses est dominant comme dans le cas des nanofils. De plus, la contribution de chaque mode de phonon au flux thermique est complexe et hautement anisotrope. Les distributions angulaires du flux thermique dans les nanofilms et les nanofils le montrent également. L'introduction de faces rugueuses a un impact principalement sur les modes acoustiques et tend à concentrer le flux thermique dans la direction principale du transport.

Pour finir, les interfaces polyphasées en Ge peuvent présenter de faibles conductivités thermiques, du même ordre de grandeur que les interfaces Si/Ge. Des méthodes de Dynamique Moléculaire fournissent une décomposition spectrale du flux thermique aux interfaces, qui est comparée aux résultats du Diffusive Mismatch Model. Dans des travaux futurs, des modèles plus réalistes d'interfaces paramétrés à l'aide de simulations de Dynamique Moléculaire seront implémentés dans notre simulateur Monte Carlo. Ceci permettra la simulation complète des nanofils polyphasés et fournira une connaissance approfondie du transport thermique dans ces nanodispositifs.

Bibliography

Akiyama, Toru, Takato Komoda, Kohji Nakamura, and Tomonori Ito. 2017. "Effects of Polytypism on the Thermoelectric Properties of Group-IV Semiconductor Nanowires: A Combination of Density Functional Theory and Boltzmann Transport Calculations." *Physical Review Applied* 8 (2): 024014. https://doi.org/10.1103/PhysRevApplied.8.024014.

Aksamija, Z., and I. Knezevic. 2010. "Anisotropy and Boundary Scattering in the Lattice Thermal Conductivity of Silicon Nanomembranes." *Physical Review B* 82 (4). https://doi.org/10.1103/PhysRevB.82.045319.

Alkurdi, A., S. Pailhès, and S. Merabia. 2017. "Critical Angle for Interfacial Phonon Scattering: Results from Ab Initio Lattice Dynamics Calculations." *Applied Physics Letters* 111 (9): 093101. https://doi.org/10.1063/1.4997912.

Berman, R., F. E. Simon, and J. M. Ziman. 1953. "The Thermal Conductivity of Diamond at Low Temperatures." *Proceedings of the Royal Society A: Mathematical, Physical and Engineering Sciences* 220 (1141): 171–83. https://doi.org/10.1098/rspa.1953.0180.

Boukai, Akram I., Yuri Bunimovich, Jamil Tahir-Kheli, Jen-Kan Yu, William A. Goddard Iii, and James R. Heath. 2008. "Silicon Nanowires as Efficient Thermoelectric Materials." *Nature* 451 (7175): 168–71. https://doi.org/10.1038/nature06458.

Callaway, Joseph. 1959. "Model for Lattice Thermal Conductivity at Low Temperatures." *Physical Review* 113 (4): 1046–51. https://doi.org/10.1103/PhysRev.113.1046.

Capinski, W. S., H. J. Maris, E. Bauser, I. Silier, M. Asen-Palmer, T. Ruf, M. Cardona, and E. Gmelin. 1997. "Thermal Conductivity of Isotopically Enriched Si." *Applied Physics Letters* 71 (15): 2109. https://doi.org/10.1063/1.119384.

Casimir, H. B. G. 1938. "Note on the Conduction of Heat in Crystals." *Physica* 5 (6): 495–500. https://doi.org/10.1016/S0031-8914(38)80162-2.

Chalopin, Y., K. Esfarjani, A. Henry, S. Volz, and G. Chen. 2012. "Thermal Interface Conductance in Si/Ge Superlattices by Equilibrium Molecular Dynamics." *Physical Review B* 85 (19). https://doi.org/10.1103/PhysRevB.85.195302.

Chaput, Laurent, Jérôme Larroque, Philippe Dollfus, Jérôme Saint-Martin, and David Lacroix. 2018. "Ab Initio Based Calculations of the Thermal Conductivity at the Micron Scale." *Applied Physics Letters* 112 (3): 033104. https://doi.org/10.1063/1.5010959.

Chen, G. 2005. *Nanoscale Energy Transport and Conversion: A Parallel Treatment of Electrons, Molecules, Phonons, and Photons.* MIT-Pappalardo Series in Mechanical Engineering. Oxford University Press. https://books.google.nl/books?id=M3n3lUJpYDYC.

Chen, G., M. S. Dresselhaus, G. Dresselhaus, J.-P. Fleurial, and T. Caillat. 2003. "Recent Developments in Thermoelectric Materials." *International Materials Reviews* 48 (1): 45–66. https://doi.org/10.1179/095066003225010182.

Chen, Jie, Gang Zhang, and Baowen Li. 2010. "How to Improve the Accuracy of Equilibrium Molecular Dynamics for Computation of Thermal Conductivity?" *Physics Letters A* 374 (23): 2392–6. http://www.sciencedirect.com/science/article/pii/S0375960110004081.

Chen, Renkun, Allon I. Hochbaum, Padraig Murphy, Joel Moore, Peidong Yang, and Arun Majumdar. 2008. "Thermal Conductance of Thin Silicon Nanowires." *Physical Review Letters* 101 (10). https://doi.org/10.1103/PhysRevLett.101.105501.

Chen, Yunfei, Deyu Li, Jennifer R. Lukes, and Arun Majumdar. 2005. "Monte Carlo Simulation of Silicon Nanowire Thermal Conductivity." *Journal of Heat Transfer* 127 (10): 1129. https://doi.org/10.1115/1.2035114.

Donadio, Davide, and Giulia Galli. 2009. "Atomistic Simulations of Heat Transport in Silicon Nanowires." *Physical Review Letters* 102 (19): 195901. https://doi.org/10.1103/PhysRevLett.102.195901.

Fourier, Joseph. 1822. *Theorie Analytique de La Chaleur, Par M. Fourier.* chez Firmin Didot, pere et fils.

Garg, Jivtesh, Nicola Bonini, Boris Kozinsky, and Nicola Marzari. 2011. "Role of Disorder and Anharmonicity in the Thermal Conductivity of Silicon-Germanium Alloys: A First-Principles Study." *Physical Review Letters* 106 (4). https://doi.org/10.1103/PhysRevLett.106.045901.

Hamzeh, Hani, and Frédéric Aniel. 2011. "Monte Carlo Study of Phonon Dynamics in III-V Compounds." *Journal of Applied Physics* 109 (6): 063511. https://doi.org/10.1063/1.3553409.

Hao, Qing, Gang Chen, and Ming-Shan Jeng. 2009. "Frequency-Dependent Monte Carlo Simulations of Phonon Transport in Two-Dimensional Porous Silicon with Aligned Pores." *Journal of Applied Physics* 106 (11): 114321. https://doi.org/10.1063/1.3266169.

He, Yuping, Ivana Savić, Davide Donadio, and Giulia Galli. 2012. "Lattice Thermal Conductivity of Semiconducting Bulk Materials: Atomistic Simulations." *Physical Chemistry Chemical Physics* 14 (47): 16209. https://doi.org/10.1039/c2cp42394d.

Heremans, Joseph P., Mildred S. Dresselhaus, Lon E. Bell, and Donald T. Morelli. 2013. "When Thermoelectrics Reached the Nanoscale." *Nature Nanotechnology* 8 (7): 471–73. https://doi.org/10.1038/nnano.2013.129.

Hicks, L. D., and M. S. Dresselhaus. 1993. "Effect of Quantum-Well Structures on the Thermoelectric Figure of Merit." *Physical Review B* 47 (19): 12727–31. https://doi.org/10.1103/PhysRevB.47.12727.

Hochbaum, Allon I., Renkun Chen, Raul Diaz Delgado, Wenjie Liang, Erik C. Garnett, Mark Najarian, Arun Majumdar, and Peidong Yang. 2008. "Enhanced Thermoelectric Performance of Rough Silicon Nanowires." *Nature* 451 (7175): 163–67. https://doi.org/10.1038/nature06381.

Holland, M. G. 1963. "Analysis of Lattice Thermal Conductivity." *Physical Review* 132 (6): 2461. http://journals.aps.org/pr/abstract/10.1103/PhysRev.132.2461.

Hu, Ming, Konstantinos P. Giapis, Javier V. Goicochea, Xiaoliang Zhang, and Dimos Poulikakos. 2011. "Significant Reduction of Thermal Conductivity in Si/Ge Core-Shell Nanowires." *Nano Letters* 11 (2): 618–23. https://doi.org/10.1021/nl103718a.

Hu, Ming, and Dimos Poulikakos. 2012. "Si/Ge Superlattice Nanowires with Ultralow Thermal Conductivity." *Nano Letters* 12 (11): 5487–94. https://doi.org/10.1021/nl301971k.

Jacoboni, Carlo, and Paolo Lugli. 1989. *The Monte Carlo Method for Semiconductor Device Simulation*. Edited by S. Selberherr. Computational Microelectronics. Vienna: Springer Vienna. http://link.springer.com/10.1007/978-3-7091-6963-6.

Jacoboni, C., and P. Lugli. 2012. *The Monte Carlo Method for Semiconductor Device Simulation*. Computational Microelectronics. Springer Vienna. https://books.google.fr/books?id=_l39CAAAQBAJ.

Ju, Y. S., and K. E. Goodson. 1999. "Phonon Scattering in Silicon Films with Thickness of Order 100 Nm." *Applied Physics Letters* 74 (20): 3005–7. https://doi.org/10.1063/1.123994.

Kazan, M., G. Guisbiers, S. Pereira, M. R. Correia, P. Masri, A. Bruyant, S. Volz, and P. Royer. 2010. "Thermal Conductivity of Silicon Bulk and Nanowires: Effects of Isotopic Composition, Phonon Confinement, and Surface Roughness." *Journal of Applied Physics* 107 (8): 083503. https://doi.org/10.1063/1.3340973.

Klitsner, Tom, J. E. VanCleve, Henry E. Fischer, and R. O. Pohl. 1988. "Phonon Radiative Heat Transfer and Surface Scattering." *Physical Review B* 38 (11): 7576–94. https://doi.org/10.1103/PhysRevB.38.7576.

Kukita, Kentaro, Indra Nur Adisusilo, and Yoshinari Kamakura. 2014. "Monte Carlo Simulation of Thermal Conduction in Silicon Nanowires Including Realistic Phonon Dispersion Relation." *Japanese Journal of Applied Physics* 53 (1): 015001. https://doi.org/10.7567/JJAP.53.015001.

Lacroix, David, Karl Joulain, and Denis Lemonnier. 2005. "Monte Carlo Transient Phonon Transport in Silicon and Germanium at Nanoscales." *Physical Review B* 72 (6): 064305. https://doi.org/10.1103/PhysRevB.72.064305.

Lacroix, David, Karl Joulain, Damian Terris, and Denis Lemonnier. 2006. "Monte Carlo Simulation of Phonon Confinement in Silicon Nanostructures: Application to the Determination of the Thermal Conductivity of Silicon Nanowires." *Applied Physics Letters* 89 (10): 103104. https://doi.org/10.1063/1.2345598.

Landry, E. S., and A. J. H. McGaughey. 2009. "Thermal Boundary Resistance Predictions from Molecular Dynamics Simulations and Theoretical Calculations." *Physical Review B* 80 (16). https://doi.org/10.1103/PhysRevB.80.165304.

Larroque, J. 2016. "Étude Théorique de L'anisotropie Du Transport Thermique Dans Les Nanostructures à Base de Silicium et de Germanium." PhD thesis. https://tel.archives-ouvertes.fr/tel-01298072/document.

Larroque, J., P. Dollfus, and J. Saint-Martin. 2017. "Full-Band Modelling of Phonons in Polytype Ge and Si." *Journal of Physics: Conference Series* 906 (October): 012007. https://doi.org/10.1088/1742-6596/906/1/012007.

Larroque, Jérôme, Philippe Dollfus, and Jérôme Saint-Martin. 2018. "Phonon Transmission at Si/Ge and Polytypic Ge Interfaces Using Full-Band Mismatch Based Models." *Journal of Applied Physics* 123 (2): 025702. https://doi.org/10.1063/1.5007034.

Li, Deyu, Yiying Wu, Philip Kim, Li Shi, Peidong Yang, and Arun Majumdar. 2003. "Thermal Conductivity of Individual Silicon Nanowires." *Applied Physics Letters* 83 (14): 2934–6. https://doi.org/10.1063/1.1616981.

Li, Ju, Lisa Porter, and Sidney Yip. 1998. "Atomistic Modeling of Finite-Temperature Properties of Crystalline β-SiC." *Journal of Nuclear Materials* 255 (2-3): 139–52. https://doi.org/10.1016/S0022-3115(98)00034-8.

Li, Wu, Natalio Mingo, L. Lindsay, D. A. Broido, D. A. Stewart, and N. A. Katcho. 2012. "Thermal Conductivity of Diamond Nanowires from First Principles." *Physical Review B* 85 (19): 195436. https://doi.org/10.1103/PhysRevB.85.195436.

Little, W. A. 1959. "The Transport of Heat Between Dissimilar Solides at Low Temperatures." *Canadian Journal of Physics* 37 (3): 334–49. https://doi.org/10.1139/p59-037.

Liu, Ling, and Xi Chen. 2010. "Effect of Surface Roughness on Thermal Conductivity of Silicon Nanowires." *Journal of Applied Physics* 107 (3): 033501. https://doi.org/10.1063/1.3298457.

Liu, Wenjun, and Mehdi Asheghi. 2006. "Thermal Conductivity Measurements of Ultra-Thin Single Crystal Silicon Layers." *Journal of Heat Transfer* 128 (1): 75. https://doi.org/10.1115/1.2130403.

Luisier, Mathieu, and Gerhard Klimeck. 2009. "Atomistic Full-Band Simulations of Silicon Nanowire Transistors: Effects of Electron-Phonon Scattering." *Physical Review B* 80 (15): 155430. https://doi.org/10.1103/PhysRevB.80.155430.

Madelung, O, U Rössler, and M Schulz. 2002. "Landolt-Börnstein-Group III Condensed Matter." *Non-Tetrahedrally Bonded Elements and Binary Compounds I.*

Maire, Jeremie, Roman Anufriev, Ryoto Yanagisawa, Aymeric Ramiere, Sebastian Volz, and Masahiro Nomura. 2017. "Heat Conduction Tuning by Wave Nature of Phonons." *Science Advances* 3 (8): e1700027. https://doi.org/10.1126/sciadv.1700027.

Markussen, Troels, Antti-Pekka Jauho, and Mads Brandbyge. 2008. "Heat Conductance Is Strongly Anisotropic for Pristine Silicon Nanowires." *Nano Letters* 8 (11): 3771–5. https://doi.org/10.1021/nl8020889.

Maurer, L. N., Z. Aksamija, E. B. Ramayya, A. H. Davoody, and I. Knezevic. 2015. "Universal Features of Phonon Transport in Nanowires with Correlated Surface Roughness." *Applied Physics Letters* 106 (13): 133108. https://doi.org/10.1063/1.4916962.

Mazumder, Sandip, and Arunava Majumdar. 2001. "Monte Carlo Study of Phonon Transport in Solid Thin Films Including Dispersion and Polarization." *Journal of Heat Transfer* 123 (4): 749. https://doi.org/10.1115/1.1377018.

Mei, S., L. N. Maurer, Z. Aksamija, and I. Knezevic. 2014. "Full-Dispersion Monte Carlo Simulation of Phonon Transport in Micron-Sized Graphene Nanoribbons." *Journal of Applied Physics* 116 (16): 164307. https://doi.org/10.1063/1.4899235.

Merabia, Samy, and Konstantinos Termentzidis. 2012. "Thermal Conductance at the Interface Between Crystals Using Equilibrium and Nonequilibrium Molecular Dynamics." *Physical Review B* 86 (9). https://doi.org/10.1103/PhysRevB.86.094303.

Mingo, Natalio, Liu Yang, Deyu Li, and Arun Majumdar. 2003. "Predicting the Thermal Conductivity of Si and Ge Nanowires." *Nano Letters* 3 (12): 1713–6. https://doi.org/10.1021/nl034721i.

Mingo, N., and Liu Yang. 2003. "Phonon Transport in Nanowires Coated with an Amorphous Material: An Atomistic Green's Function Approach." *Physical Review B* 68 (24). https://doi.org/10.1103/PhysRevB.68.245406.

Moore, Arden L., Sanjoy K. Saha, Ravi S. Prasher, and Li Shi. 2008. "Phonon Backscattering and Thermal Conductivity Suppression in Sawtooth Nanowires." *Applied Physics Letters* 93 (8): 083112. https://doi.org/10.1063/1.2970044.

Moore, Arden L., and Li Shi. 2014. "Emerging Challenges and Materials for Thermal Management of Electronics." *Materials Today* 17 (4): 163–74. https://doi.org/10.1016/j.mattod.2014.04.003.

Mu, Xin, Lili Wang, Xueming Yang, Pu Zhang, Albert C. To, and Tengfei Luo. 2015. "Ultra-Low Thermal Conductivity in Si/Ge Hierarchical Superlattice Nanowire." *Scientific Reports* 5 (November): 16697. https://doi.org/10.1038/srep16697.

Narumanchi, Sreekant V. J., Jayathi Y. Murthy, and Cristina H. Amon. 2005. "Comparison of Different Phonon Transport Models for Predicting Heat Conduction in Silicon-on-Insulator Transistors." *Journal of Heat Transfer* 127 (7): 713. https://doi.org/10.1115/1.1924571.

Nghiêm, T. T. Trang, J. Saint-Martin, and P. Dollfus. 2016. "Electro-Thermal Simulation Based on Coupled Boltzmann Transport Equations for Electrons and Phonons." *Journal of Computational Electronics* 15 (1): 3–15. https://doi.org/10.1007/s10825-015-0773-2.

Ozhogin, V. I., A. V. Inyushkin, A. N. Taldenkov, A. V. Tikhomirov, G. E. Popov, E. Haller, and K. Itoh. 1996. "Isotope Effect in the Thermal Conductivity of Germanium Single Crystals." *Journal of Experimental and Theoretical Physics Letters* 63 (6): 490–94. http://link.springer.com/article/10.1134/1.567053.

Peierls. 1929. "Zur Kinetischen Theorie Der Wärmeleitung in Kristallen." https://onlinelibrary.wiley.com/doi/abs/10.1002/andp.19293950803.

Peterson, R. B. 1994. "Direct Simulation of Phonon-Mediated Heat Transfer in a Debye Crystal." *Journal of Heat Transfer* 116 (4): 815–22. https://doi.org/10.1115/1.2911452.

Péraud, Jean-Philippe M., and Nicolas G. Hadjiconstantinou. 2011. "Efficient Simulation of Multidimensional Phonon Transport Using Energy-Based Variance-

Reduced Monte Carlo Formulations." *Physical Review B* 84 (20): 205331. https://doi.org/10.1103/PhysRevB.84.205331.

Plimpton, Steve. 1995. "Fast Parallel Algorithms for Short-Range Molecular Dynamics." *Journal of Computational Physics* 117 (1): 1–19. http://www.sciencedirect.com/science/article/pii/S002199918571039X.

Pop, Eric. 2010. "Energy Dissipation and Transport in Nanoscale Devices." *Nano Research* 3 (3): 147–69. https://doi.org/10.1007/s12274-010-1019-z.

Qiu, Bo, Lin Sun, and Xiulin Ruan. 2011. "Lattice Thermal Conductivity Reduction in Bi 2 Te 3 Quantum Wires with Smooth and Rough Surfaces: A Molecular Dynamics Study." *Physical Review B* 83 (3): 035312. https://doi.org/10.1103/PhysRevB.83.035312.

Qiu, Bo, Zhiting Tian, Ajit Vallabhaneni, Bolin Liao, Jonathan M. Mendoza, Oscar D. Restrepo, Xiulin Ruan, and Gang Chen. 2015. "First-Principles Simulation of Electron Mean-Free-Path Spectra and Thermoelectric Properties in Silicon." *EPL (Europhysics Letters)* 109 (5): 57006. https://doi.org/10.1209/0295-5075/109/57006.

Ramayya, E. B., L. N. Maurer, A. H. Davoody, and I. Knezevic. 2012. "Thermoelectric Properties of Ultrathin Silicon Nanowires." *Physical Review B* 86 (11): 115328. https://doi.org/10.1103/PhysRevB.86.115328.

Ruf, T., R.W. Henn, M. Asen-Palmer, E. Gmelin, M. Cardona, H.-J. Pohl, G.G. Devyatych, and P.G. Sennikov. 2000. "Thermal Conductivity of Isotopically Enriched Silicon." *Solid State Communications* 115 (5): 243–47. https://doi.org/10.1016/S0038-1098(00)00172-1.

Santamore, D. H., and M. C. Cross. 2001. "Effect of Surface Roughness on the Universal Thermal Conductance." *Physical Review B* 63 (18). https://doi.org/10.1103/PhysRevB.63.184306.

Sääskilahti, K., J. Oksanen, J. Tulkki, and S. Volz. 2014. "Role of Anharmonic Phonon Scattering in the Spectrally Decomposed Thermal Conductance at Planar Interfaces." *Physical Review B* 90 (13). https://doi.org/10.1103/PhysRevB.90.134312.

Schelling, Patrick K., Simon R. Phillpot, and Pawel Keblinski. 2002. "Comparison of Atomic-Level Simulation Methods for Computing Thermal Conductivity." *Physical Review B* 65 (14). https://doi.org/10.1103/PhysRevB.65.144306.

Seko, Atsuto, Atsushi Togo, Hiroyuki Hayashi, Koji Tsuda, Laurent Chaput, and Isao Tanaka. 2015. "Prediction of Low-Thermal-Conductivity Compounds with First-Principles Anharmonic Lattice-Dynamics Calculations and Bayesian Optimization." *Physical Review Letters* 115 (20): 205901. https://doi.org/10.1103/PhysRevLett.115.205901.

Sellan, D. P., E. S. Landry, J. E. Turney, A. J. H. McGaughey, and C. H. Amon. 2010. "Size Effects in Molecular Dynamics Thermal Conductivity Predictions." *Physical Review B* 81 (21). https://doi.org/10.1103/PhysRevB.81.214305.

Setyawan, Wahyu, and Stefano Curtarolo. 2010. "High-Throughput Electronic Band Structure Calculations: Challenges and Tools." *Computational Materials Science* 49 (2): 299–312. https://doi.org/10.1016/j.commatsci.2010.05.010.

Smith, C A, R D Belles, and A J Simon. 2011. "2007 Estimated International Energy Flows." LLNL-TR-473098, 1021561. https://doi.org/10.2172/1021561.

Soffer, Stephen B. 1967. "Statistical Model for the Size Effect in Electrical Conduction." *Journal of Applied Physics* 38 (4): 1710–5. https://doi.org/10.1063/1.1709746.

Stillinger, Frank H., and Thomas A. Weber. 1985. "Computer Simulation of Local Order in Condensed Phases of Silicon." *Physical Review B* 31 (8): 5262. http://journals.aps.org/prb/abstract/10.1103/PhysRevB.31.5262.

Swartz, E. T., and R. O. Pohl. 1989. "Thermal Boundary Resistance." *Reviews of Modern Physics* 61 (3): 605–68. https://doi.org/10.1103/RevModPhys.61.605.

Termentzidis, Konstantinos, Thibaut Barreteau, Yuxiang Ni, Samy Merabia, Xanthippi Zianni, Yann Chalopin, Patrice Chantrenne, and Sebastian Volz. 2013. "Modulated SiC Nanowires: Molecular Dynamics Study of Their Thermal Properties." *Physical Review B* 87 (12): 125410. https://doi.org/10.1103/PhysRevB.87.125410.

Termentzidis, Konstantinos, and Samy Merabia. 2012. *Molecular Dynamics Simulations and Thermal Transport at the Nano-Scale*. INTECH Open Access Publisher. http://cdn.intechopen.com/pdfs/34979/InTech-Molecular_dynamics_simulations_and_thermal_transport_at_the_nano_scale.pdf.

Tersoff, J. 1989. "Modeling Solid-State Chemistry: Interatomic Potentials for Multicomponent Systems." *Physical Review B* 39 (8): 5566. http://journals.aps.org/prb/abstract/10.1103/PhysRevB.39.5566.

Thompson, Aidan P., Steven J. Plimpton, and William Mattson. 2009. "General Formulation of Pressure and Stress Tensor for Arbitrary Many-Body Interaction Potentials Under Periodic Boundary Conditions." *The Journal of Chemical Physics* 131 (15): 154107. https://doi.org/10.1063/1.3245303.

Tian, Zhiting, Keivan Esfarjani, and Gang Chen. 2012. "Enhancing Phonon Transmission Across a Si/Ge Interface by Atomic Roughness: First-Principles Study with the Green's Function Method." *Physical Review B* 86 (23). https://doi.org/10.1103/PhysRevB.86.235304.

Togo, Atsushi, Laurent Chaput, and Isao Tanaka. 2015. "Distributions of Phonon Lifetimes in Brillouin Zones." *Physical Review B* 91 (9): 094306. https://doi.org/10.1103/PhysRevB.91.094306.

Verdier, Maxime, David Lacroix, and Konstantinos Termentzidis. 2018. "Thermal Transport in 2D and 3D Nanowire Networks." *arXiv:1802.05654 [Cond-Mat]*, February. http://arxiv.org/abs/1802.05654.

Vincent, Laetitia, Gilles Patriarche, Géraldine Hallais, Charles Renard, Cyrille Gardès, David Troadec, and Daniel Bouchier. 2014. "Novel Heterostructured Ge Nanowires Based on Polytype Transformation." *Nano Letters* 14 (8): 4828–36. https://doi.org/10.1021/nl502049a.

Vining, Cronin B. 2009. "An Inconvenient Truth About Thermoelectrics." *Nature Materials* 8 (2): 83–85. https://doi.org/10.1038/nmat2361.

Volz, Sebastian G., and Gang Chen. 1999. "Molecular Dynamics Simulation of Thermal Conductivity of Silicon Nanowires." *Applied Physics Letters* 75 (14): 2056. https://doi.org/10.1063/1.124914.

———. 2000. "Molecular-Dynamics Simulation of Thermal Conductivity of Silicon Crystals." *Physical Review B* 61 (4): 2651–6. https://doi.org/10.1103/PhysRevB.61.2651.

Weber, Werner. 1977. "Adiabatic Bond Charge Model for the Phonons in Diamond, Si, Ge, and α-Sn." *Physical Review B* 15 (10): 4789–4803. https://doi.org/10.1103/PhysRevB.15.4789.

Wolf, Stefanie, Neophytos Neophytou, and Hans Kosina. 2014. "Thermal Conductivity of Silicon Nanomeshes: Effects of Porosity and Roughness." *Journal of Applied Physics* 115 (20): 204306. https://doi.org/10.1063/1.4879242.

Yang, Lina, and Austin J. Minnich. 2017. "Thermal Transport in Nanocrystalline Si and SiGe by Ab Initio Based Monte Carlo Simulation." *Scientific Reports* 7 (1). https://doi.org/10.1038/srep44254.

Yang, Ronggui, and Gang Chen. 2004. "Thermal Conductivity Modeling of Periodic Two-Dimensional Nanocomposites." *Physical Review B* 69 (19). https://doi.org/10.1103/PhysRevB.69.195316.

Yu, Jen-Kan, Slobodan Mitrovic, Douglas Tham, Joseph Varghese, and James R. Heath. 2010. "Reduction of Thermal Conductivity in Phononic Nanomesh Structures." *Nature Nanotechnology* 5 (10): 718–21. https://doi.org/10.1038/nnano.2010.149.

Ziman, J. M. 2001. *Electrons and Phonons: The Theory of Transport Phenomena in Solids*. Oxford Classic Texts in the Physical Sciences. Oxford, New York: Oxford University Press.

Titre : Étude théorique des propriétés thermoéletriques de nanostructures

Mots clés : thermoelectricité, simulation, Monte Carlo, Dynamique Moleculaire, transport thermique

Résumé : Les générateurs thermoélectriques convertissent directement l'énergie thermique en énergie électrique. Ils pourraient devenir de plus en plus utiles à des fins de récupération d'énergie et font l'objet de recherches actives. Cependant, les meilleurs matériaux thermoélectriques sont rares et polluants.
Le Silicium et le Germanium seraient des matériaux intéressants si leur efficacité thermoélectrique était améliorée. Pour ce faire, la nanostructuration est une voie possible, par exemple en introduisant des faces rugueuses ou de nouvelles interfaces semi-transparentes.
Récemment, des nanofils polyphasés (composés d'une alternance de phases cubiques et hexagonales de Si et Ge) ont été fabriqués, mais la caractérisation expérimentale de nanostructures aussi complexes comprenant des matériaux exotiques peut être difficile.
Dans cette thèse, nous étudions en détail le transport thermique dans des nanostructures avec des simulations numériques. Une méthode Monte Carlo originale a été développée, avec une description "full band" des matériaux. Elle inclut des modèles pour les faces rugueuses et les interfaces entre matériaux. Des simulations de Dynamique Moléculaire sont également effectuées pour caractériser les propriétés des interfaces.
Nous confirmons que les phases hexagonales de Si et Ge ont une conductivité thermique inférieure à celle des phases cubiques correspondantes. Le modèle "full band" montre que le flux thermique est fortement anisotrope. Des modèles semi-analytiques habituels n'ont pas pu reproduire la conductivité thermique des nanostructures simulées avec des faces rugueuses. De plus, ces faces ont tendance à concentrer le flux de chaleur dans la direction principale de la nanostructure. Enfin, certaines interfaces polyphasées peuvent avoir une conductance thermique presque aussi faible que les interfaces Si/Ge, et pourrait ainsi améliorer significativement l'efficacité thermoélectrique des nanofils polyphasés.
La méthode Monte Carlo présentée peut facilement être utilisée pour étudier une large gamme de matériaux, et elle est capable de modéliser des nanostructures arbitrairement complexes. A l'avenir, les simulations en Dynamique Moléculaire seront utilisées pour paramétrer un modèle plus réaliste d'interfaces.

Title : Theoretical study of thermoelectric properties in nanostructures

Keywords : thermoelectricity, simulation, Monte Carlo, Molecular Dynamics, thermal transport

Abstract : Thermoelectric generators are able to directly convert heat into electrical energy. They could have a great potential in terms of energy harvesting, but unfortunately, the best thermoelectric materials are rare and pollutant.
Silicon and Germanium would be attractive materials if their thermoelectric efficiency were improved. For this purpose, nanostructuring is a possible route, for instance via the introduction of rough boundaries or interfaces between materials.
Recently, polytype nanowires (composed of a sequence of cubic and hexagonal phases of Si and Ge) have been fabricated, but the experimental characterization of such complex nanostructures with exotic materials is challenging.
In this thesis, we study the details of thermal transport in nanostructures with numerical simulations. An original Monte Carlo method is developed, with a full band *ab initio* description of materials. It includes models for the rough boundaries and the solid-solid interfaces. Molecular Dynamics simulations are also performed to characterize the properties of interfaces.
We confirm that the hexagonal phases of Si and Ge have lower thermal conductivity than their cubic counterparts. The full band model shows a strong anisotropy in the heat flux. Usual semi-analytical models failed to reproduce the thermal conductivity of simulated nanostructures with rough boundaries. Besides, those boundaries tend to focus the heat flux in the main direction of the nanostructure. Finally, some polytype interfaces can have an interfacial conductance almost as low as Si/Ge interfaces, and thus could improve significantly the thermoelectric efficiency of polytype nanowires.
The presented Monte Carlo method could easily be used with a wide range of materials, and it can model arbitrarily complex nanostructures. In the future, the results from Molecular Dynamics simulation will be used to parametrize a more realistic model of solid-solid interfaces.

Université Paris-Saclay
Espace Technologique / Immeuble Discovery
Route de l'Orme aux Merisiers RD 128 / 91190 Saint-Aubin, France